A 3D Time Domain CSEM Forward Modeling Code using custEM and FEniCS

Marc Seidel

A 3D Time Domain CSEM Forward Modeling Code using custEM and FEniCS

Inaugural-Dissertation

zur Erlangung des Doktorgrades

(Dr. rer. nat.)

der Mathematischen-Naturwissenschaftlichen Fakultät

der Universität zu Köln

vorgelegt von

Marc Seidel

aus Leverkusen

Köln, 2019

Erstgutachter	Prof. Dr. Bülent Tezkan
Zweitgutachter	Prof. Dr. Andreas Hördt

Tag der mündlichen Prüfung: 25. November 2019

Für Juri, den ersten Menschen in unserem Weltall.

Abstract

A new 3D time domain CSEM forward modeling code *TDcustEM* built upon the recently published open-source frequency domain code custEM and the open-source finite element toolbox FEniCS is presented. The transformation of the frequency domain data provided by custEM is performed by a Fast Hankel Transform using 80 digital filter coefficients. 3D edge-based tetrahedral meshes generated by TetGen facilitate the calculation of synthetic data using topography, arbitrary loop and dipole source geometries and complex subsurface structures. To ensure precision and reliability of the new algorithm, calculated results of different CSEM setups and electromagnetic field components are cross-validated against analytic solutions and well-established 1D (EMUPLUS) and 3D (SLDMEM) time domain modeling codes.

Certain modeling studies are conducted regarding possible interpolation and extrapolation techniques to reduce the number of necessary frequencies and therefore the computational runtime, which is still an issue of convolutional time domain CSEM approaches. Additional modeling studies showed the importance of precise receiver positioning for measuring the horizontal components of the time derivative of the magnetic field. The performance of the implemented 80 filter coefficients for the Fast Hankel Transform was successfully compared with two recently published sets of 101 and 201 filter coefficients for loop and dipole source transmitters.

As the present thesis is embedded in the Collaborative Research Centre 806 – *Our Way to Europe*, three sedimentary deposits in the East African Rift Valley were subject to multidimensional TEM surveys in the framework of this project. Geophysical measurements assist with the identification and definition of possible paleoenvironmental archives which serve as potential coring locations for paleoclimatic reconstructions.

Common 1D (EMUPLUS) as well as laterally and spatially constrained (AarhusInv) inversion techniques were applied to the TEM field data. Sediment thicknesses as well as stratigraphic sequences of the investigated sedimentary basins were derived. An extensive 3D modeling study of one of the target areas representing a volcanically-formed basin including topography was performed using the newly developed TDcustEM code.

Zusammenfassung

Im Rahmen der vorliegenden Arbeit wurde das Programm *TDcustEM* zur 3D CSEM Modellierung im Zeitbereich unter Verwendung des kürzlich veröffentlichten open-source Frequenzbereichcodes custEM und der finiten Elemente Bibliothek FEniCS entwickelt. Die Transformation der custEM Frequenzbereichsdaten in den Zeitbereich erfolgt mittels einer Schnellen Hankel Transformation mit 80 digitalen Filterkoeffizienten. Die simulierten dreidimensionalen Domänen bestehenen aus kantenbasierten Tetraederelementen und werden von TetGen erzeugt. Dies ermöglicht die Berechnung synthetischer elektrischer und magnetischer Daten mit Topographie, beliebig geformten Stromquellen und komplexen Untergrundstrukturen. Um die Funktionalität des neuen Algorithmus unter Beweis zu stellen, wurden dessen Ergebnisse mit analytischen Lösungen sowie bewährten 1D (EMUPLUS) und 3D (SLDMEM) Vorwärtsalgorithmen im Zeitbereich erfolgreich verglichen.

Um die große Anzahl Frequenzen und die damit verbundenen Laufzeiten, die für eine Vorwärtsrechnung im Zeitbereich benötigt werden, zu reduzieren, wurden diverse Extrapolations- und Interpolationsstudien durchgeführt. Darüber hinaus wurde in Modellstudien gezeigt, dass präzise Positionierungen der Empfänger wichtig sind wenn die zeitliche Ableitung der horizontalen Magnetfelder gemessen wird. Die Leistungsfähigkeit der implementierten 80 Filterkoeffizienten für die Transformation in den Zeitbereich wurde erfolgreich mit zwei kürzlich veröffentlichten 101 und 201 Koeffizienten umfassende Filtersets für galvanisch und induktiv angekoppelte Sendergeometrien verglichen.

Die vorliegende Arbeit ist Teil des Sonderforschungsbereiches 806 – *Our Way to Europe*. Im Rahmen dieser Arbeit wurden drei multidimensionale TEM Messkampagnen auf Sedimentationsbecken im ostafrikanischen Graben durchgeführt. Die geophysikalischen Messungen ermöglichen die Untersuchung und Charakterisierung der Sedimentbecken im Sinne paläoklimatologischer Archive als potentielle Bohrlokationen und einer anschließenden Rekonstruktion des lokal vorherrschenden Paläoklimas.

Die TEM Felddaten wurden mit herkömmlichen 1D (EMUPLUS) und sogenannten "laterally und spatially constrained" (AarhusInv) Inversionstechniken interpretiert. Darauf beruhend wurden Sedimentmächtigkeiten bzw. stratigrafische Schichtungen der untersuchten Sedimentbecken abgeleitet. Mit dem neu entwickelten Code wurde abschließend eine umfangreiche 3D Modellstudie inklusive Topografie durchgeführt, die eines der untersuchten Gebiete - einen vulkanischer Krater mit einem See in der Mitte - abbildet.

Contents

List of Figures

List of Tables

CHAPTER 1

Introduction

Within the broad field of exploration techniques in geophysics, electromagnetic (EM) methods have become a well established tool over the last decades. Possible fields of EM research cover hydrocarbon and mineral exploration, groundwater and geothermal investigations, CO_2 storage characterization, environmental studies, geological and sedimentary formations and many others. Aside from potential methods and ground-penetrating radar, EM methods usually focus on investigating the physical parameter of the electrical resistivity (respectively its reciprocal, the electrical conductivity) and deriving reasonable resistivity models of the subsurface. Controlled-source electromagnetic (CSEM) surveys are set to detect subsurface structures from depths of a few meters up to several kilometers and are nowadays commonly conducted air-borne, marine and land-based.

In order to predict the electromagnetic signature of complex geological subsurface structures, advanced 3D modeling algorithms are essential. To create accurate synthetical data and, in a second step, to produce inversion results of real field data, the speed, quality and reliability of these algorithms are vital. In applied geophysics, electromagnetic forward modeling techniques are usually incorporated in the frequency domain and afterwards transformed to the time domain if desired. The minority of 3D algorithms published to this day solve the governing physical equations directly in the time domain.

The Finite Difference (FD) and the Finite Element (FE) method have been widely accepted as numerical methods for the spatial discretization of the modeled domain, the latter becoming more and more prevalent as the performance of modern computers permanently increases. Although the implementation of the FD method is straightforward, its major drawback is the limitation to regular meshes with staggered grids. Modeling complex geological anomalies and realistic topographies in 3D requires the incorporation of irregular and unstructured meshes built from non-rectangular elements like tetrahedra for example.

Rochlitz et al. (2019) developed and published an open-source toolbox custEM (customizable Electromagnetic Modeling) for the simulation of 3D CSEM data in the frequency domain. The toolbox is based on the open-source finite element library FEniCS, a computing framework for solving partial differential equations (*Logg et al.*, 2012). FEniCS

supports tetrahedral meshes, high-order finite element polynomials, parallel computing and provides Python and C++ interfaces.

In the framework of the present thesis, a 3D time domain CSEM forward modeling algorithm *TDcustEM* (Time Domain custEM) was developed in collaboration with R. Rochlitz from the Leibniz Institute for Applied Geophysics in Hanover, Germany. The TDcustEM algorithm utilizes the custEM toolbox and transforms the calculated frequency domain data into the time domain by performing a Fast Hankel Transform (FHT).

Within custEM and TDcustEM, different approaches of solving Maxwell's equations are implemented including the commonly applied E-field approach in form of the total and secondary field approach. Both algorithms are written in Python and the particular PDEs are solved in parallel (MPI) with the direct solver MUMPS. For the generation of high-quality tetrahedral meshes, TetGen (*Si*, 2015) and the pyGIMLi library (*Rücker et al.*, 2017) are used. Nodal (Lagrange), edge-based (Nédélec) and mixed tetrahedral elements are implemented.

To ensure reliability and accuracy of the TDcustEM algorithm, the calculated results are cross-validated against analytic solutions and well-established 1D and 3D algorithms.

After the successful cross-validation of the code, the TDcustEM software is utilized to assist in the interpretation of real time domain field data. The present PhD project was embedded in the Collaborative Research Centre 806 (CRC 806) – *Our Way to Europe*. Combining geoscientific and archeological methods, the CRC 806 is designed to reconstruct the passageway of homo sapiens from eastern Africa to central Europe over the last 200,000 years. Geophysical measurements assist with the identification and definition of possible paleoenvironmental archives such as sedimental deposits. These deposits serve as coring locations for a subsequent reconstruction of the paleoclimate.

In 2014 and 2015, two multidimensional transient CSEM field surveys have been conducted on three sedimental basins in the East-African rift valley. On each location, the vertical and one horizontal component of the time derivate of the magnetic field have been recorded. These time domain CSEM field data are subject to a modeling study with TDcustEM within this thesis.

The present thesis is composed of the following chapters:

- In **Chapter 1**, the state of research regarding 3D CSEM modeling is summarized with the main focus lying on recent advances of the different numerical approaches. Following this, the motivation of this thesis is presented.

- **Chapter 2** contains the basic theoretical background for 3D electromagnetic modeling. An introduction of the finite element method and of the Fast Hankel Transform is given and different time domain modeling approaches are discussed.

- The developed algorithm TDcustEM is described in **Chapter 3**. Here, the time domain results of the algorithm are cross-validated against analytic solutions for uniform half-spaces, for 1D layered subsurfaces against the software *EMUPLUS* and for 3D models against the finite differences code *SLDMEM*. The chapter closes with a brief study about the runtimes of the TDcustEM.

- In **Chapter 4**, various modeling studies are presented. First, the implemented FHT filter coefficient set is assessed and a possible reduction of the necessary number of frequencies by extrapolation and interpolation techniques is discussed. Following this, modeling studies regarding precise receiver positioning, reasonable domain sizes and resistivity contrasts are presented.

- An application of the TDcustEM algorithm to real field data from a TEM survey in the East-African rift valley is presented in **Chapter 5**. Additionally, this chapter contains conventional and laterally or spatially constrained 1D inversion results of data from the three TEM surveys conducted in Ethiopia within the framework of the CRC 806.

- **Chapter 6** concludes the thesis with a summary and an outlook.

1.1. State of Research

With permanent advances in computer technology and processing speed over the last decades, 3D controlled-source electromagnetic forward modeling further increases its importance in all fields of ground-based, airborne and marine exploration geophysics. *Avdeev* (2005) and *Börner* (2010) reviewed the development of CSEM forward modeling until 10 years ago. Since then, significant progresses have been made especially in time domain simulations. Apart from numerous publications regarding 1D and 2D CSEM modelings, this chapter concentrates only on 3D CSEM simulations. For a brief overview of recent publications regarding 1D forward modelings, see for example *Werthmüller* (2017).

Integral equations

One of the first attempts of 3D CSEM forward modeling was the *integral equation* (IE) method which dates back to the 1970s when *Raiche* (1974), *Hohmann* (1975) and *Weidelt* (1975) almost simultaneously presented their results for the solution of Maxwell's equations in the frequency domain. *Weidelt* (1975) converts Maxwells's equations to a linear inhomogeneous vector integral equation and applies it to a 3D anomalous body in which the electrical conductivity deviates from a horizontally layered 1D background structure. The resulting total field is then calculated by superposition of the anomalous 3D field and the background 1D field. All integral equations are basically of the form

$$\mathbf{E}(\mathbf{r}) = \mathbf{E}_0(\mathbf{r}) + \int_{V^s} \underline{\underline{G}}(\mathbf{r}, \mathbf{r}')\mathbf{E}(\mathbf{r}')\Delta\sigma(\mathbf{r}')d^3\mathbf{r}' \tag{1.1}$$

which is also known as the scattering equation (*Avdeev*, 2005). Here, the electric field at position $\mathbf{r}$ is composed of the known background field $\mathbf{E}_0$ and an anomalous field caused by a volume V^s with a different conductivity $\Delta\sigma(\mathbf{r}')$ with respect to the background. To solve the volume integral over the anomalous scattering volume V^s, Green's function $\underline{\underline{G}}(\mathbf{r}, \mathbf{r}')$ needs to be computed. The main advantage of the integral equation method is that only the scattering volume V^s needs to be discretized which reduces the system matrix considerably for simple model geometries. The major drawback of the integral equation method is, however, the complex formulation of the problem and the tedious computation of the system matrix (*Avdeev*, 2005).

The first application of the IE method for 3D time domain modeling was presented by *Newman et al.* (1986) who transform the calculated frequency domain data into the time domain by applying a Fourier transform with sine and cosine digital filters.

Finite Differences

One of the standard tools and most commonly implemented approaches of 3D CSEM forward modeling is the *Finite Difference* (FD) method (*Wang and Hohmann*, 1993; *Mackie et al.*, 1993; *Commer and Newman*, 2004). One advantage of the FD method and therefore one reason for its extensive use is the comparably low implementational effort. On the other hand, FD approaches can become computationally expensive for regular meshes on complex geometries.

Druskin and Knizhnerman (1988, 1994, 1999) presented a 3D finite difference algorithm based on the spectral Lanczos decomposition method (SLDM) using Krylov subspaces. In Chapter 3, their algorithm will be used to cross-validate the results of the algorithm developed in the framework of this thesis. Most FD algorithms are implemented on

staggered grids, which have been introduced by *Yee* (1966). Within a Yee cell, the electric field components are edge-averaged while the associated $\partial_t \mathbf{B}$ components are face-averaged and calculated by taking the curl of $\mathbf{E}$ (*Börner*, 2010). *Rätz* (2000) points out that generating an adequate FD grid for a complex 3D model can become quite challenging which is a drawback of the FD approach.

Another issue for Finite Differences in the time domain (FDTD) is that explicit time stepping approaches require very small time step sizes to satisfy stability conditions especially when large conductivity contrasts are modeled (*Um et al.*, 2012).

However, the major disadvantage of the FD method is its inability to work on unstructured grids. Complex model geometries can only be satisfyingly represented with the FD method when the subsurface consists of rectangular shaped structures. Otherwise, staircasing on curved boundaries may lead to imprecise results and misinterpretations.

Finite Elements

The aforementioned issue concerning rectangular grids can be overcome by the *Finite Element Method* (FEM), which turned out to have the greatest flexibility regarding model geometries using tetrahedral meshes (*Schwarzbach et al.*, 2011). Additionally, it offers a good trade-off between accuracy, number of degrees of freedom (dofs) and spatial distribution of physical parameters.

Although the history of FEM in electromagnetic modeling goes back a long way (*Coggon*, 1971; *Pridmore et al.*, 1981; *Livelybrooks*, 1993; *Sugeng*, 1998; *Badea et al.*, 2001) only in recent years, with a permanent increase of computational power, the FE method has become the standard discretization technique in 3D CSEM modeling. An introduction into the FE technique and a condensed theory of the FEM is given in Chapter 2.2.

One early challenge of CSEM modeling using the FEM was the possible jump of normal components across material interfaces (*Börner*, 2010). Standard *nodal* (Langrange) elements which force all field components to be continuous across element boundaries can not reproduce the physical behavior of field discontinuities and may lead to spurious solutions (*Börner*, 2010). This issue was resolved by the introduction of curl-conforming Nédélec elements (*Nédélec*, 1980, 1986), also known as *edge* elements. This family of elements uses vector basis functions which assign the degrees of freedom to the element edges and can therefore perfectly treat the discontinuities of electric and magnetic fields across interfaces. Adaptive mesh refinement (h-refinement) and the refinement of polynomial degrees (p-refinements, i.e. increasing the dofs per element) can drastically improve the solution accuracy.

Considering FEM CSEM frequency domain modeling, there have been numerous publications over the last decade. *Schwarzbach et al.* (2011) presented a 3D vector FE simulation for marine CSEM scenarios applying a primary/secondary field approach and higher-order finite elements with an adaptive mesh refinement. *Puzyrev et al.* (2013) published results of a nodal finite element parallel algorithm for anisotropic media implementing a secondary field formulation on unstructured tetrahedral meshes. Further publications of electromagnetic frequency domain algorithms using the FEM have been presented by *Ansari and Farquharson* (2014); *Grayver and Kolev* (2015); *Li et al.* (2017).

Castillo-Reyes et al. (2018) published their Parallel Edge-based Tool for Geophysical Electromagnetic Modeling (PETGEM), an open-source parallel algorithm for modeling 3D

CSEM problems. PETGEM solves the frequency domain Maxwell's equations applying the secondary electric field approach on Nédélec edge finite elements. Furthermore, an automatic mesh adaptation strategy for a specific source position is presented.

Most recently, *Rochlitz et al.* (2019) developed and published the open-source toolbox custEM (customizable electromagnetic modeling) which is based on the open-source finite element library FEniCS (Finite Elements in Computer Sciences). FEniCS supports tetrahedral meshes, multiprocessing, higher order polynomials and anisotropy. In custEM, multiple finite element approaches to solve the time-harmonic Maxwell equations using total or secondary electric field and gauged potential formulations, are implemented. In addition, *Rochlitz et al.* (2019) developed a secondary magnetic field formulation which showed superior performance if only magnetic fields are required. Using vector basis functions, the current density is incorporated on the edges of the elements for the total field formulations which facilitates modeling of CSEM problems with topography.

Frequency domain calculations with a subsequent transform into the time domain have been presented by e.g. *Gupta et al.* (1989); *Sugeng* (1998) and *Börner et al.* (2015). The number of publications presenting pure time domain FEM 3D CSEM modeling algorithms using time-stepping methods is rather short. *Um et al.* (2010) were the first to present a CSEM finite element approach in the time domain by applying time-stepping with the E-field approach (see Chapter 2.1.3). The algorithm simulates transient electric fields and the time derivate of the magnetic field using direct time-stepping with an implicit backward Euler scheme. *Um et al.* (2012) extended this approach by an adaptive time step doubling (ATSD), an algorithm which reduces CPU runtime by allowing large time steps at late times when high-frequency field components are increasingly attenuated. The ATSD was also implemented by *Cai et al.* (2017) who as well presented an edge-based finite element time domain modeling algorithm using a backward Euler scheme.

Another FEM time domain forward solver was presented by *Li et al.* (2018) who implemented a total-field algorithm on unstructured tetrahedral meshes applying the backward Euler method. Unstructured tetrahedral grids combined with a local refinement technique was used to model complex-shaped loop sources.

Finite Volumes

Haber et al. (2007) solved the time domain forward problem using the Finite Volume (FV) method, which is related to the FD method, using an implicit backward Euler time discretization scheme. According to *Rochlitz et al.* (2019), the FV method combines the advantages of a straightforward implementation, similar to the FD method, with unstructured meshes like the FE method. But *Jahandari et al.* (2017) showed that the accuracy of FV simulations is inferior to the FEM when they compared two FE and three FV schemes which use unstructured tetrahedral grids. Moreover, *Rylander et al.* (2013) state two more drawbacks of the FV method in the time domain using time-stepping. First, weak numerical instabilities may appear at late times and second, the FV method needs very small time steps when the cells are not uniform in size.

1.2. Thesis Motivation

As highlighted in the previous section, the most reasonable numerical method for the forward calculation of 3D CSEM data is the finite element method because of its flexibility regarding unstructured meshes while offering satisfying accuracy with an adequate number of degrees of freedom per cell. There are different ways of modeling time domain data (direct time-stepping, Fourier-like transforms, see Chapter 2.4). Within the course of the present thesis, it was decided to calculate the desired data in the frequency domain and afterwards transform it into the time domain via a Fast Hankel Transform. This procedure is fast, precise and well-proven.

The open-source toolbox *custEM* (*Rochlitz et al.*, 2019) is used as the fundamental frequency domain code. Till this day, *custEM* is the only known and established 3D CSEM forward modeling open-source code that unites the usage of unstructured tetrahedral meshes with Nédélec basis functions, arbitrary source and subsurface geometries, parallel processing, higher-order polynomials, topography, anisotropy and multiple approaches to solve the time-harmonic Maxwell equations.

The ambition and purpose of the present thesis consist of three major goals:

- Develop an algorithm that provides all the aforementioned benefits from custEM and transfers them to a 3D time domain CSEM forward modeling software *TDcustEM*.
- Investigate TDcustEM's capabilities regarding precision, reliability, computational speed and hardware requirements.
- Create a 3D model with topography and apply the developed time domain forward code to a two-dimensional field data set from a TEM survey on a sedimentary basin.

As the present thesis is part of the CRC 806 and three geophysical surveys have been conducted in Ethiopia in the framework of this project, an additional separate goal is:

- Determine the sediment thicknesses and subsurface structures of the investigated sedimentary basins in Eastern Africa with common 1D inversion techniques of the recorded TEM data to assist in finding possible future drilling locations.

1.3. Preliminary Notes

Throughout this thesis, vectors are presented in lower bold letters and matrices in capital bold letters. Exceptions are the electromagnetic fields $\mathbf{B}$, $\mathbf{H}$, $\mathbf{E}$ and $\mathbf{D}$ which are as well displayed in capital bold letters.

When comparing magnetic field results to analytic solutions, they are given as the time derivative of the magnetic field strength $\partial_t \mathbf{H}$, in all other cases the time derivative of the magnetic flux density $\partial_t \mathbf{B}$ is given.

In many figures of this thesis, TEM transients showing $\partial_t \mathbf{B}$ results are labelled *transient response* and are source current and receiver area normalized to 1 Am^2. The transmitter loop areas or dipole lengths are not included in this normalization.

The simplified expressions *resistivity* and *conductivity* denote the specific electrical resistivity ρ and the specific electrical conductivity σ, respectively.

CHAPTER 2

Computational Electromagnetics

Faraday's law of induction
The law of all sea and all land
No lies, no deceit, no corruption
In this law so complete and so grand!

A Physics Utopia (Folk Song)
Dr. Walter Fox Smith, 2001

The following chapter portrays the fundamentals of computational electromagnetic forward modeling and the underlying electromagnetic theory. Computational electromagnetics is an interdisciplinary subject, a combination of physics, computer sciences and mathematics. Generally spoken, electromagnetic problems are described mathematically by defining an equivalent boundary value problem consisting of the governing PDEs (i.e. Maxwell's equations or some derivative), boundary conditions and, for time-dependent problems, initial conditions. Once the problem is described, an effective numerical method to solve the problem needs to be set up and implemented into efficient computer code.

Computational methods for EM simulations can be divided into two groups: time domain and frequency domain methods. They are related to each other by Fourier-like transforms and their inverse transforms, respectively. Time-dependent problems are mathematically represented in four dimensions: three spatial dimensions plus the time dimension. In the frequency domain only three dimensions are required. Fourier transform techniques detach the time dimension from the problem formulation and therefore reduce the problem complexity – the higher the number of dimensions the greater the problem complexity. Calculating the data in the frequency domain allows for a subsequent transform to the time domain. However, many frequencies need to be calculated to reach a solution precision of an acceptable degree.

2.1. Electromagnetic Fundamentals

In applied geophysics, electromagnetic methods are based on the principle of electromagnetic induction. Its general idea is sketched in Figure 2.1.

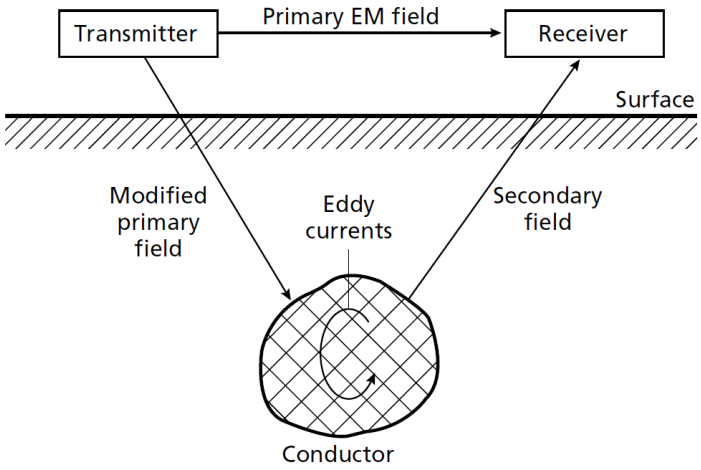

Figure 2.1.: *The principle of electromagnetic induction in applied geophysics (Figure from Kearey et al., 2002).*

In controlled-source electromagnetics (CSEM), an actively controlled transmitter generates a time-dependent primary electromagnetic signal which induces electric eddy currents in the conductive subsurface. These currents in turn generate a secondary electromagnetic field whose electric and magnetic components can be measured at a given receiver position. The objective then is to derive the conductivity distribution of the subsurface from the characteristics of the measured signals. The behavior of electric and magnetic fields, varying in time and space, is described by Maxwell's equations which will be introduced in the following subsection.

2.1.1. Maxwell's Equations

The electromagnetic field theory has been an essential component in many areas of science and engineering since James Clark Maxwell presented his electromagnetic theory in 1873 (*Maxwell*, 1873). His theory describes the interaction between moving electric charges by *Maxwell's equations* (Eq. 2.1 - 2.4 in the differential form), a system of coupled partial differential equations (PDE) that relate sources (electric charges and electric currents) to time varying electromagnetic fields and fluxes. All field quantities are functions of space and time.

$$\nabla \cdot \mathbf{D} = \rho \tag{2.1}$$
$$\nabla \cdot \mathbf{B} = 0 \tag{2.2}$$
$$\nabla \times \mathbf{E} = -\partial_t \mathbf{B} \quad \text{(Faraday's law)} \tag{2.3}$$
$$\nabla \times \mathbf{H} = \partial_t \mathbf{D} + \mathbf{j} \quad \text{(Ampère's law)} \tag{2.4}$$

In this set, the number of equations is less than the number of unknowns. The *constitutive equations* (Eq. 2.5 - 2.7) specify the relation between the field quantities causing

Maxwell's equations to become definite. The constitutive relations describe the macroscopic properties of the medium being considered. For an isotropic, homogeneous medium they read:

$$\mathbf{B} = \mu \mathbf{H} \tag{2.5}$$
$$\mathbf{D} = \epsilon \mathbf{E} \tag{2.6}$$
$$\mathbf{j} = \sigma \mathbf{E} \tag{2.7}$$

with the constitutive parameters μ (the magnetic permeability), ϵ (the electric permittivity) and σ (the electric conductivity). These parameters are scalars for isotropic media and tensors for anisotropic media. Equation (2.7) is called *Ohm's law* which states that in conducting media the electric field induces a conduction current with the density $\mathbf{j}$. Together with the *equation of continuity*

$$\nabla \cdot \mathbf{j} + \partial_t \rho = 0 \tag{2.8}$$

which describes the conservation of charges, all aforementioned equations together form the fundamental base of the classical theory of electromagnetism.

When considering harmonically oscillating electromagnetic fields with a single frequency, the fields are called *time-harmonic* and (2.3, 2.4) can be transformed into the frequency domain. This transform yields complex-valued fields but has the advantage that the time derivate ∂_t can be substituted by a multiplication operator $i\omega$ for a given function $f(\mathbf{r}, t)$

$$\frac{\partial}{\partial t} f(\mathbf{r}, t) \rightarrow i\omega f(\mathbf{r}, \omega) \tag{2.9}$$

where i is the imaginary unit and ω the angular frequency. Equations (2.3) and (2.4) can now be written as:

$$\nabla \times \mathbf{E} = -i\omega \mathbf{B} \tag{2.10}$$
$$\nabla \times \mathbf{H} = i\omega \mathbf{D} + \mathbf{j} \tag{2.11}$$

The transformation from time domain to frequency domain and back can be done by a *Fourier transform* (2.12) and the inverse Fourier transform (2.13), respectively:

$$\mathbf{E}(\omega) = \frac{1}{2\pi} \int_{-\infty}^{\infty} \mathbf{E}(t) e^{-i\omega t} dt \tag{2.12}$$
$$\mathbf{E}(t) = \int_{-\infty}^{\infty} \mathbf{E}(\omega) e^{i\omega t} d\omega \tag{2.13}$$

The use of time-harmonic fields is not as restrictive as it seems. By using Fourier analysis, any time-varying field can be expressed in terms of time-harmonic components via Eq. 2.12. Therefore, if the time-harmonic expression of a field is known for any ω, its counterpart in the time domain can be calculated by Eq. (2.13) (*Jin*, 2014).

Table 2.1 shows all electromagnetic symbols, their quantities name and their SI unit to be in use throughout this thesis.

Symbol	Quantity	SI Unit
$\mathbf{E}$	Electric field strength	$^{\mathrm{V}}/_{\mathrm{m}}$
$\mathbf{D}$	Displacement field strength	$^{\mathrm{C}}/_{\mathrm{m}^2}$
$\mathbf{H}$	Magnetic field strength	$^{\mathrm{A}}/_{\mathrm{m}}$
$\mathbf{B}$	Magnetic flux	$\mathrm{T} = {}^{\mathrm{Vs}}/_{\mathrm{m}^2}$
$\mathbf{j}$	Electric current density	$^{\mathrm{A}}/_{\mathrm{m}^2}$
ρ	Electric charge density	$^{\mathrm{C}}/_{\mathrm{m}^3}$
ϵ	Electric permittivity	$^{\mathrm{As}}/_{\mathrm{Vm}}$
μ	Magnetic permeability	$^{\mathrm{Vs}}/_{\mathrm{Am}}$
σ	Electric conductivity	$^{\mathrm{S}}/_{\mathrm{m}}$
ρ	Electric resitivity	$\Omega\mathrm{m}$
t	Time	s
ω	Angular frequency	$^{\mathrm{rad}}/_{\mathrm{s}}$

Table 2.1.: *List of symbols in electromagnetics.*

2.1.2. Interface Conditions

Interface conditions describe the behavior of the tangential and the normal components of the electromagnetic fields across an interface of two materials with different values for the electrical permittivity ϵ and the magnetic permeability μ. The conditions can be derived from the integral form of Maxwell's equations (*Jin*, 2010). With $\mathbf{n}_{12}$ denoting the normal vector from medium 1 to medium 2, they read:

$$\mathbf{n}_{12} \times (\mathbf{E}_2 - \mathbf{E}_1) = 0 \tag{2.14}$$

$$\mathbf{n}_{12} \cdot (\mathbf{D}_2 - \mathbf{D}_1) = \rho_s \tag{2.15}$$

$$\mathbf{n}_{12} \cdot (\mathbf{B}_2 - \mathbf{B}_1) = 0 \tag{2.16}$$

$$\mathbf{n}_{12} \times (\mathbf{H}_2 - \mathbf{H}_1) = \mathbf{j}_s \tag{2.17}$$

where ρ_s is the surface charge density on the interface and $\mathbf{j}_s$ is the surface current on the interface between the two media. Therefore, the tangential component of the electric field $\mathbf{E}$ is continuous across the interface while the normal component of the electric displacement field $\mathbf{D}$ is discontinuous. The normal component of $\mathbf{B}$ is continuous and the tangential component of $\mathbf{H}$ is discontinuous across the interface.

2.1.3. The E-Field Equation

The curl-curl E-field equation (or vector-wave E-field equation) can be obtained by eliminating the magnetic flux $\mathbf{B}$ from Faraday's law of induction (Eq. 2.3) by using Ampère's law (Eq. 2.4) and the constitutive equations. The electric current density $\mathbf{j}$ in Faraday's law can be split up into a source and induction part as

$$\mathbf{j} = \mathbf{j}_{ind} + \mathbf{j}_s \tag{2.18}$$

with the electric source current density $\mathbf{j}_s$ and the induced current density $\mathbf{j}_{ind} = \sigma\mathbf{E}$. This yields for the time domain:

$$\nabla \times \mu^{-1}\nabla \times \mathbf{E} + \partial_t^2 \epsilon \mathbf{E} + \partial_t \sigma \mathbf{E} = -\partial_t \mathbf{j}_s \tag{2.19}$$
$$\tag{2.20}$$

After a Fourier transform (2.12), the same equation reads in the frequency domain:

$$\nabla \times \mu^{-1}\nabla \times \mathbf{E} - \omega^2 \epsilon \mathbf{E} + i\omega\sigma\mathbf{E} = -i\omega\mathbf{j}_s \tag{2.21}$$

For most electromagnetic methods in applied geophysics, the displacement current $-\omega^2\epsilon\mathbf{E}$ is much smaller then the induction current $i\omega\sigma\mathbf{E}$ and can therefore be neglected. This approximation is called the *quasi-static approximation*

$$\omega^2\epsilon << i\omega\sigma \tag{2.22}$$

and it yields the quasi-static *total* E-field formulation in the frequency domain:

$$\nabla \times \mu^{-1}\nabla \times \mathbf{E} + i\omega\sigma\mathbf{E} = -i\omega\mathbf{j}_s. \tag{2.23}$$

Note that this approximation is not suitable for highly resistive regions where $\sigma \approx 0$ because in that case the term $\partial_t\sigma\mathbf{E}$ approaches zero. To complete the boundary value problem, a Dirichlet boundary condition can be applied on the boundary Γ:

$$\mathbf{n} \times \mathbf{E} = E_D \tag{2.24}$$

with $E_D = 0$ (Zero–Dirichlet) in case of a perfect conductor boundary condition.

By applying the *secondary* (or scattered) E-field approach $\mathbf{E} = \mathbf{E}^0 + \mathbf{E}^s$ (*Newman and Alumbaugh*, 1995), Equation (2.23) can be written as

$$\nabla \times \mu^{-1}\nabla \times \mathbf{E}^s + i\omega\sigma\mathbf{E}^s = -i\omega\Delta\sigma\mathbf{E}^0 \tag{2.25}$$

with the primary background field $\mathbf{E}^0$ and the secondary (anomalous) field $\mathbf{E}^s$. The conductivity σ can be split up accordingly into $\sigma = \sigma_0 + \Delta\sigma$. Here, σ_0 is a background model conductivity represented by a horizontally layered medium (*Grayver and Kolev*, 2015).

In the course of this thesis, the focus will be on the total E-field approach because the secondary E-field approach was not fully implemented for dipole sources in custEM by the time of writing these lines. The calculation of the magnetic field $\mathbf{H}$ is commonly of great interest as well, it can in a second step be obtained by

$$\mathbf{H} = -\frac{1}{i\omega\mu}\nabla \times \mathbf{E} \tag{2.26}$$

in the frequency domain.

2.2. The Finite Element Method

The Finite Element Method (FEM) is a standard numerical method for solving Partial Differential Equations (PDEs) in various disciplines of science and engineering. To be more precise, it is a numerical procedure to convert PDEs into a set of linear algebraic equations and then to obtain an approximate solution to a boundary value problem by solving this set of equations subject to given boundary conditions.

The extent of the FEM including all forms and variations is far-reaching and too complex to be presented here. A detailed introduction into the FEM and specifically its application to electromagnetics can be found in *Jin* (2014) or *Monk* (2003). A comprehensive description of a general implementation of the FEM is provided by *Gockenbach* (2006). The following section will give a brief summary of the basic principles of the FEM and the discretization of the E-field equation (2.23 and 2.25).

The FEM can be formulated using either the *Method of Weighted Residuals* (MWR) or the *variational* method. In the variational or 'Ritz' method, a given boundary-value problem is formulated in terms of a functional and an approximate solution is then obtained by minimizing this functional. Variational principles are best suited for mechanics of solids and structures due to their connection to energy principles. The MWR is a more general mathematical construct for solving all kinds of PDEs. Within this introduction into the FEM, the MWR is chosen because of its simplicity and popularity.

2.2.1. The Method of Weighted Residuals

The general form of a (partial) differential equation in a domain Ω enclosed by the boundary Γ and given boundary conditions can be written in abstract form as

$$L[u] = s \tag{2.27}$$

with an arbitrary differential operator L, a source excitation function s and the unknown function u to be found. The basic idea of the FEM now is to convert this differential equation into a system of linear equations of the form $\mathbf{Ax} = \mathbf{b}$ and solve for $\mathbf{x}$ by inverting the matrix $\mathbf{A}$ and multiplying it with the known vector $\mathbf{b}$.

The unknown function $u = u(x, y, z)$ in (2.27) can be approximated as

$$\hat{u}(x, y, z) \approx \sum_{i=1}^{N} u_i \, \phi_i(x, y, z) \tag{2.28}$$

with ϕ_i being a set of linear or polynomial *basis functions* and u_i being the elements of the vector of the degrees of freedom to be computed. Or in other words, the u_i's are the values of the unknown function u on the nodes i ($i = 1, \ldots, N$) of the discretization grid of the domain Ω. The differential equation can now be written as

$$L\left[\sum_{i=1}^{N} u_i \, \phi_i(x, y, z)\right] = s \, . \tag{2.29}$$

The expanded approximation of u (2.28) does usually not exactly solve the PDE, instead, a value called the *residual* R is "left over":

$$R = L\left[\sum_{i=1}^{N} u_i\,\phi_i(x,y,z)\right] - s \neq 0 \tag{2.30}$$

Assuming the given functions ϕ_i to be known, all values u_i need to be chosen in the way to minimize R. In the next step, N independent *weighting* or *test* functions w_j are multiplied to (2.30) and a subsequent integration over the complete domain Ω of both sides yields:

$$\int_\Omega R\,w_j\,d\Omega = \int_\Omega L\left[\sum_{i=1}^{N} u_i\,\phi_i - s\right] w_j\,d\Omega \stackrel{!}{=} 0 \tag{2.31}$$

with $\phi_i = \phi_i(x,y,z)$.

Of all MWR used in the scientific and engineering community, one particular method, the *Galerkin method of weighted residuals* is by far the most widely used, and has shown to provide the most accurate solutions on a wide variety of problems (*Zohdi*, 2015). In Galerkin's MWR, the weighting functions w_j are selected to be the same as the basis functions ϕ_i used for the approximation solution $\hat{u}$ in (2.28)

$$w_j = \phi_j \tag{2.32}$$

in the sense that the unknown functions u_i make the approximate solution $\hat{u}$ become zero in the space spanned by the basis functions ϕ_i, i.e. $u_i \perp \phi_i$:

$$\int_\Omega \phi_j\,L\left[\sum_{i=1}^{N} u_i\phi_i - s\right] d\Omega = 0 \tag{2.33}$$

This is the so-called *weak formulation* of the original PDE (the original form is called the *strong* formulation). Weak formulations are often an integral form and require a weaker continuity of the corresponding field variables. A strong form, in contrast to a weak form, requires strong continuity on the dependent field variables which means that the functions defining these field variables have to be differentiable up to the order of the original PDE. Weak forms usually require equality in an average or inner product sense only. The inner product of two complex-valued vector fields $\mathbf{u}$ and $\mathbf{v}$ is

$$\langle \mathbf{u}, \mathbf{v} \rangle = \int_\Omega \mathbf{u} \cdot \overline{\mathbf{v}}\,d\Omega \tag{2.34}$$

where $\overline{\mathbf{v}}$ is the complex conjugate of $\mathbf{v}$.

All steps so far lead to N equations for N unknowns. Assuming L to be linear, the initial differential equation can now be expressed as:

$$\underbrace{\sum_{i=1}^{N} u_i}_{\mathbf{x}}\ \underbrace{\int_\Omega L[\phi_i]\phi_j\,d\Omega}_{\mathbf{A}}\ =\ \underbrace{\int_\Omega s\,\phi_j\,d\Omega}_{\mathbf{b}}\,. \tag{2.35}$$

The term marked as $\mathbf{A}$ has the form of a matrix. $\mathbf{A}$ can be calculated because the functions ϕ_i, ϕ_j and the differential operator L are known. The right hand side vector $\mathbf{b}$ can also

be calculated and therefore this system of linear equations of the form $\mathbf{Ax} = \mathbf{b}$ can be computationally solved with $\mathbf{x}$ containing the unknown values u_i of interest. Obtaining the sought solution can be achieved using either direct or iterative solvers. If the differential operator L is self-adjoint, Galerkin's MWR results in the same system of equations as those obtained by the variational method (*Jin*, 2014).

The major challenge in the process described above is to find test functions that approximate the true solution the best way and at the same time satisfy the boundary conditions. For simple 1D problems, it is sometimes possible to find such functions for the entire solution domain. But for 2D and 3D problems this is almost impossible (*Jin*, 2014). This problem is solved by dividing the entire domain Ω into smaller subdomains and define test functions that are continuous over each element. Such subdomain test functions are usually much simpler than domain-wide test functions because they only have to approximate the solution on much smaller subdomains. In the FEM, the test functions are a combination of basis functions defined over small subdomains, so-called *finite elements*, which constitute the entire domain. These elements have a finite size in which the physical parameters (e.g. the electrical conductivity σ) are constant. The behavior of the fields inside each cell is described by so-called *shape functions* (also called basis or interpolation functions) which guarantee continuous field forms across element boundaries.

The general recipe of applying the FEM to a boundary-value problem consists of the following steps:

1. Discretization of Ω into smaller subdomains
2. Selection of local shape functions
3. Assembling of the global system of equations
4. Solution of the global system of equations
5. Computation of derived variables

Depending on the problem to be solved, a large variety of different finite elements in 1D, 2D and 3D is available for the discretization of the computational domain Ω, cf. *Logg et al.* (2012). Here, only two basic kinds of tetrahedral finite elements are presented because for the simulation of arbitrary and complex subsurface geometries, tetrahedral elements are best suited. Other 3D finite elements are for example hexahedra, prisms, pyramids or any kind of cuboids.

The nodal-based or *Lagrange* element (Figure 2.2a for polynomial degree 1 and Figure 2.2b for polynomial degree 2) is probably the most widely used finite element. The degrees of freedom are located on the nodes of the tetrahedron for $p = 1$. For higher-order polynomials, additional dofs are distributed on the element edges. The calculated values of the investigated function are scalars on Lagrange elements. This may lead to spurious solutions when dealing with vector field problems (*Börner*, 2010) and nodal elements are therefore not well suited for three-dimensional electromagnetics.

The problem of spurious solutions can be solved by using curl-conforming edge-based or *Nédélec* vector elements (Figure 2.2c and 2.2d) on which the degrees of freedom are assigned to the edges of the elements. Nédélec elements perfectly capture the discontinuities

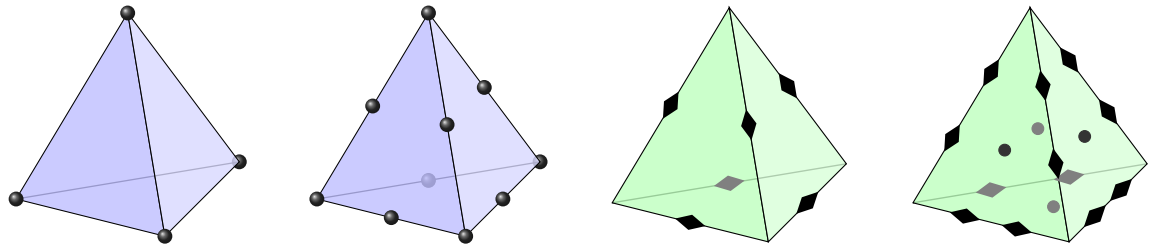

(a) *Lagrange, p=1* **(b)** *Lagrange, p=2* **(c)** *Nédélec, p=1* **(d)** *Nédélec, p=2*

Figure 2.2.: *Two basic kinds of finite elements. a) and b) show nodal (Lagrange) elements, c) and d) show edge-based (Nédélec) elements, each for polynomial degrees 1 and 2. Edge-based elements (or vector-valued elements) model the behavior of electromagnetic fields more accurately than nodal elements.*

of the electric and magnetic fields along material interfaces (*Börner*, 2010). Within this thesis, edge-based finite elements are used for the calculation of the electromagnetic fields up to a polynomial order of $p = 2$. Using polynomials of the order $p = 3$ or higher would in fact increase the solution accuracy but the computation time for solving the system matrix would disproportionally increase as well (*Rochlitz et al.*, 2019).

In addition to element nodes and edges, 3D scalar and vectorial degrees of freedom can also be calculated on element facets or inside the element volume.

2.2.2. Discretization of the E-Field Equation

The spatial discretization of the E-field equation in this section and the derivation of the linear system of equations to be solved follow generally the steps of *Börner* (2010). The boundary value problem (2.23) imposed by a perfect conductor boundary condition ($\mathbf{n} \times \mathbf{E} = 0$) can be expressed in the weak form by taking the inner product of (2.23) together with a test function ϕ. After an integration by parts, the E-field equation reads:

$$\begin{aligned} \int_\Omega \left[(\mu^{-1}\nabla \times \mathbf{E}) \cdot (\nabla \times \phi) + i\omega\sigma\mathbf{E} \cdot \phi\right] d\Omega \\ - \int_\Gamma (\mathbf{n} \times \phi) \cdot (\mu^{-1}\nabla \times \mathbf{E})\, d\Gamma = -i\omega \int_\Omega \mathbf{j}_s \cdot \phi\, d\Omega \end{aligned} \tag{2.36}$$

Regarding the integral over the boundary Γ, the perfect conductor boundary condition provides no information about the term $(\mu^{-1}\nabla \times \mathbf{E})$. This integral can be eliminated by choosing ϕ such that $\mathbf{n} \times \phi = 0$ on Γ.

Next, the Nédélec function space

$$\xi := \{v \in \mathbf{H}(curl; \Omega) : \mathbf{n} \times \mathbf{v} = 0 \text{ on } \Gamma\} \tag{2.37}$$

with the Sobolov function space whose curl is in L^2

$$\mathbf{H}(curl; \Omega) = \{\mathbf{v} \in L^2(\Omega)^3 : \nabla \times \mathbf{v} \in L^2(\Omega)^3\} \tag{2.38}$$

is introduced. $L^2(\Omega)^3$ is a space of square-integrable 3D vector fields defined on Ω. $\mathbf{H}(curl;\Omega)$ is also a Hilbertian space with respect to the inner product defined as

$$\langle \mathbf{u}, \mathbf{v} \rangle_{\mathbf{H}(curl;\Omega)} = \int_\Omega (\mathbf{u} \cdot \overline{\mathbf{v}} + (\nabla \times \mathbf{u}) \cdot (\nabla \times \overline{\mathbf{v}}))\, d\Omega. \tag{2.39}$$

The weak form of the boundary value problem can now be expressed as follows. Find $\mathbf{E} \in \xi$ such that:

$$\int_\Omega \left[(\mu^{-1} \nabla \times \mathbf{E}) \cdot (\nabla \times \mathbf{v}) + i\omega\sigma \mathbf{E} \cdot \mathbf{v} \right]\, d\Omega = -i\omega \int_\Omega \mathbf{j}_s \cdot \mathbf{v}\, d\Omega \tag{2.40}$$

for all $\mathbf{v} \in \xi$. Discretizing the simulation domain Ω into n subdomains (e.g. tetrahedra in 3D) and replacing the electric field $\mathbf{E}$ by an approximate solution $\hat{\mathbf{E}}$ as a linear combination of n basis functions ϕ_i $(i = 1, \ldots, n)$

$$\hat{\mathbf{E}}(\mathbf{r}) = \sum_{i=1}^{n} E_i \phi_i(\mathbf{r}), \tag{2.41}$$

the matrix form of (2.40) with the unknown complex-valued coefficients $E_i = u_i$ $(i = 1, \ldots, N)$ can be written as:

$$(\mathbf{K} + i\omega\mathbf{M})\mathbf{u} = -i\omega\mathbf{f} \tag{2.42}$$

with

$$[\mathbf{K}]_{j,i} = \int_\Omega (\mu^{-1} \nabla \times \phi_i) \cdot (\nabla \times \phi_j)\, d\Omega \tag{2.43}$$

$$[\mathbf{M}]_{j,i} = \int_\Omega \sigma \phi_i \cdot \phi_j\, d\Omega \tag{2.44}$$

$$[\mathbf{f}]_j = \int_\Omega \mathbf{j}_s \cdot \phi_j\, d\Omega \tag{2.45}$$

Following Galerkin's MWR, in (2.40) the j-th basis functions has been chosen as the test functions $\mathbf{v} = \phi_j$. The symmetric matrices $\mathbf{K}$ and $\mathbf{M}$ contain the basis and test functions, defined on the function space ξ. In the FEM, they are commonly known as *stiffness matrix* ($\mathbf{K}$) and *mass matrix* ($\mathbf{M}$), respectively, and both are large and sparse. The vector $\mathbf{f}$ on the right-hand side of (2.42) contains the source excitation term of the PDE, in this case the source current density $\mathbf{j_s}$. With $\mathbf{K}$, $\mathbf{M}$, and $\mathbf{f}$ being computable, the unknown vector $\mathbf{u}$, which contains the approximated values $\hat{E}_i$ for all degrees of freedom, can now be calculated. The system matrix $(\mathbf{K} + i\omega\mathbf{M})$ is identical for the total (2.23) and secondary (2.25) field approach. In case of the secondary E-field approach, the source term on right-hand side of (2.42) reads

$$[\mathbf{f}]_j = \int_\Omega \Delta\sigma \mathbf{E}^0 \cdot \phi_j\, d\Omega. \tag{2.46}$$

After the calculation of the electric field $\mathbf{E}$, the magnetic field $\mathbf{H}$ can be derived according to (2.26) on the same Nédélec function space ξ by solving the FE problem (*Rochlitz et al.*, 2019)

$$\int_\Omega \phi_i \cdot \phi_j\, d\Omega \cdot \mathbf{H} = -\frac{1}{i\omega} \int_\Omega (\mu^{-1} \nabla \times \mathbf{E}) \cdot \phi_j\, d\Omega. \tag{2.47}$$

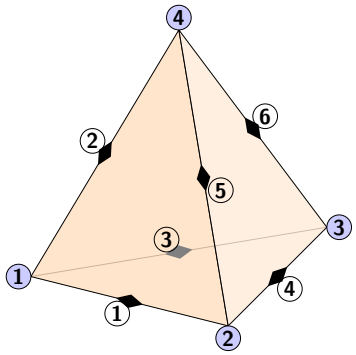

Figure 2.3.: *Tetrahedral edge element with 4 nodes (blue) and 6 edges (transparent).*

When using edge-based elements, the tangential components of the electric field $\mathbf{E}$ are assigned to the edges of each element. Any desired value inside an element can therefore be interpolated using a set of *vector* basis functions. The electric field $\mathbf{E}$ in an arbitrary tetrahedral element e ($e = 1, \ldots, n$) can be interpolated at position $\mathbf{r}$ as (*Jin*, 2010):

$$\begin{aligned}\mathbf{E}^e(\mathbf{r}) = \sum_{j=1}^{6} \mathbf{N}_j(\mathbf{r}) E_j = \mathbf{N}^e_{12}(\mathbf{r})E^e_{12} + \mathbf{N}^e_{13}(\mathbf{r})E^e_{13} + \mathbf{N}^e_{14}(\mathbf{r})E^e_{14} \\ + \mathbf{N}^e_{23}(\mathbf{r})E^e_{23} + \mathbf{N}^e_{24}(\mathbf{r})E^e_{24} + \mathbf{N}^e_{34}(\mathbf{r})E^e_{34}\end{aligned} \tag{2.48}$$

where E^e_{lk} is the tangential electric field component at the $j-th$ edge between the nodes l and k of element e (Figure 2.3). $\mathbf{N}^e_{lk}$ is the corresponding interpolation or basis function. Let N^e_l and N^e_k be the linear *scalar* interpolation function of nodes l and k as:

$$N^e_l(x, y, z) = \frac{1}{6V^e}(a^e_l + b^e_l x + c^e_l y + d^e_l z) \tag{2.49}$$

$$N^e_k(x, y, z) = \frac{1}{6V^e}(a^e_k + b^e_k x + c^e_k y + d^e_k z) \tag{2.50}$$

where V^e denotes the volume of the e-th element and $\mathbf{r} = (x, y, z)^T$. The derivation of the coefficients a_i, b_i, c_i and d_i ($i \in \{l, k\}$) can be found for example in *Jin* (2014). Considering a specific edge j between the element nodes l and k with length ℓ_{jk}, the interpolation functions $\mathbf{N}^e_j$ in (2.48) can then be written as:

$$\mathbf{N}^e_j(\mathbf{r}) = \ell_j(N^e_l \nabla N^e_k - N^e_k \nabla N^e_l) \qquad l < k \tag{2.51}$$

with ℓ_j being the length of the element edge between nodes l and k.

The vector plot of the vector basis function $\mathbf{N}^e_{lk}$ is illustrated in Figure 2.4, for simplification reasons only for a two-dimensional triangular element. Such vector basis functions have a tangential component only on the respective element edge and therefore maintain tangential continuity of the interpolated field across element boundaries. The normal component, on the other hand, is allowed to be discontinuous. These vector basis functions are called *curl-conforming* because they have zero divergence but a nonzero curl.

2.3. The Fast Hankel Transform

The transformation of the calculated frequency domain data into the time domain throughout all simulations within this thesis is performed by a Fast Hankel Transform (FHT) using

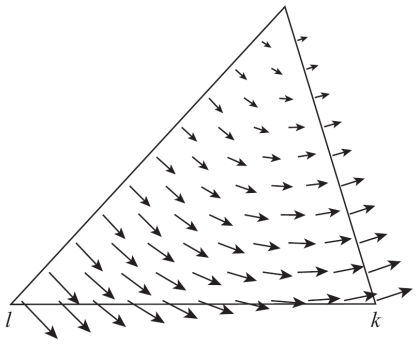

Figure 2.4.: *The vector basis function $\mathbf{N}^e_{lk}$ for the edge between nodes l and k for a linear triangular element (Jin, 2010).*

digital filter coefficients which is a common procedure in CSEM time domain modeling, as described in Chapter 2.4. The FHT comes into operation when integrals of the form

$$g(r) = \int_0^\infty f(k)\, J_\nu(kr)\, dk, \quad \nu > -1 \tag{2.52}$$

have to be evaluated. Equation (2.52) is generally denoted as a *Hankel Transform* with the function $f(k)$ to be transformed and $J_\nu(kr)$ being the *Bessel function* of the first kind and order $\nu > -1$. The evaluation of this kind of integral is numerically expensive for huge arguments kr. Because of the oscillatory behavior of the Bessel function, very small sampling rates for the numerical integration would be necessary (*Weidelt*, 1986). These numerical costs can be significantly reduced by the FHT, which uses digital linear filters for a fast computation of the Hankel integral by simplifying it to the form of a convolutional integral. The numerical evaluation of Hankel transforms using digital linear filters was firstly presented by *Ghosh* (1971) who originally computed type curves for Schlumberger and Wenner resistivity soundings. In the following years, the method was further developed by various authors (*Johansen and Sørensen*, 1979; *Andersen*, 1989; *Christensen*, 1990; *Mohsen and Hashish*, 1994).

In a first step, k and r are transformed into logarithmic space according to:

$$x = log\left(\frac{r}{r_0}\right) \tag{2.53}$$

$$y = -log\,(k\, r_0) \tag{2.54}$$

with an arbitrary scaling length $r_0 > 0$. Then, with

$$G(x) := r\, g(r) \tag{2.55}$$

$$F(y) := f(k) \tag{2.56}$$

$$H(x) := e^x\, J_\nu(e^x) \tag{2.57}$$

the Hankel transform (2.52) integral can be expressed in terms of a convolution integral:

$$G(x) = \int_{-\infty}^{\infty} F(y)\, H(x-y)\, dy. \tag{2.58}$$

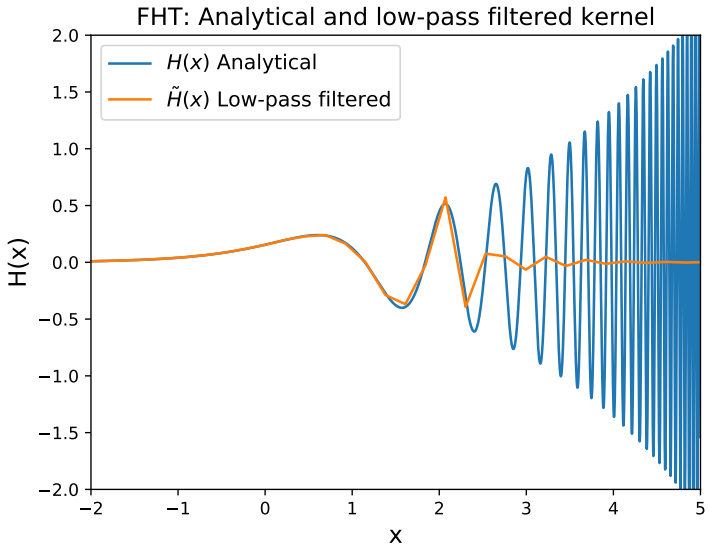

Figure 2.5.: *Convolution kernel $H(x)$ for $J_{1/2}$ (blue) and a low-pass filtered version (orange) with filter coefficients by Weidelt (1986) using 10 samples per decade.*

Yet, no advantage can be taken from (2.58) because the kernel function $H(x-y)$ is still highly oscillating for huge arguments x, see the blue curve in Figure 2.5. An integration of such a function is still demanding. The idea behind the Fast Hankel Transform now is to replace the fastly oscillating kernel function $H(x)$ with a low-pass filtered version $\tilde{H}(x)$ (orange curve in Figure 2.5). To create a low-pass filtered version $\tilde{H}(x)$, first the function $F(y)$ is replaced by an interpolated version $\tilde{F}(y)$ as:

$$\tilde{F}(y) = \sum_{n=-\infty}^{\infty} F_n \, P(y - n\Delta) \tag{2.59}$$

with an interpolation function $P(y)$ and $F_n = F(y_n)$ denoting known function values of equidistant samples $y_n = n\Delta$. The sampling length Δ has to comply with the Nyquist–Shannon sampling theorem with a maximum angular frequency ω_{max}:

$$\Delta \; > 2\, f_{max} = \frac{\omega_{max}}{\pi} \tag{2.60}$$

For higher frequencies $\omega > \omega_{max}$, $F(y) \equiv 0$. According to *Weidelt* (1986), an obvious choice for the interpolation function $P(y)$ is the *cardinal sine* function in its normalized version

$$P(y) = sinc(\pi y/\Delta) = \frac{sin(\pi y/\Delta)}{\pi y/\Delta}, \quad y \neq 0 \tag{2.61}$$

because in this case the values of $\tilde{F}(y)$ are exactly reproduced by the values of F_n. Each sample in the sequence is replaced by a sinc function. The sinc function (Figure 2.6) serves as a mathematically ideal low-pass filter that removes all frequency components above a particular cutoff frequency. Using the interpolated function $\tilde{F}(y)$, the convolutional

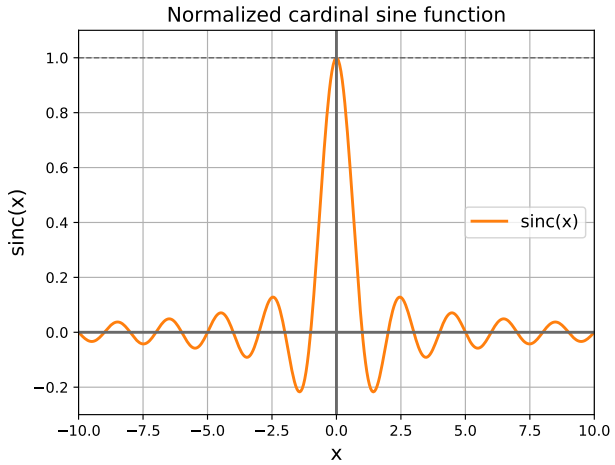

Figure 2.6.: *Normalized cardinal sine function sinc.*

integral $G(x)$ in (2.58) can now be approximated by $\hat{G}(x)$ as:

$$\hat{G}(x) = \sum_{n=-\infty}^{+\infty} F_n \int_{-\infty}^{+\infty} P(y - n\Delta)\, H(x - y)\, dy \tag{2.62}$$

$$= \sum_{n=-\infty}^{+\infty} F_n \hat{H}(x - n\Delta) \tag{2.63}$$

which was achieved by using

$$\hat{H}(x) := \int_{-\infty}^{+\infty} P(y)\, H(x - y)\, dy. \tag{2.64}$$

The discrete version of the convolutional integral (2.58) can be expressed as (*Weidelt*, 1986):

$$\hat{G}_m = \sum_{n=-\infty}^{+\infty} F_n\, \hat{H}_{m-n} \tag{2.65}$$

with

$$\hat{G}_m := G(m\Delta) \quad \text{and} \quad \hat{H}_m := \hat{H}(m\Delta) \tag{2.66}$$

on all sampling points $m\Delta$. The coefficients $\hat{H}$ in (2.65) are independent of the initial function $f(k)$ which is subject to the transformation. The coefficients need to be calculated only once for numerically fast transformations. In case of transforming frequency domain data to the time domain, the transformed variables in (2.53) and (2.54) are the time t instead of r and the frequency ω instead of k. The eventual form of the Fast Hankel Transform finally reads:

$$g(r) = \int_0^{\infty} f(k)\, J_\nu(kr)\, dk \qquad \rightarrow \qquad g(r_m) = \frac{1}{r_m} \sum_{n=n_1}^{n_2} f(k_n)\, \hat{H}_\nu(m - n)\,, \quad \nu \in (0, 1) \tag{2.67}$$

Here, the infinite negative and positive limits of the sum have been replaced by finite values n_1 and n_2, which depend on the chosen digital filter coefficients.

2.4. Time Domain CSEM Modeling

The following section discusses different approaches for CSEM modeling in the time domain and presents the procedure of transforming frequency domain data into the time domain by using the Fast Hankel Transform.

2.4.1. General Remarks

3D ground-based and marine EM measurements can technically record all six components of the EM field: three magnetic and three electric components. Air-borne receivers are limited to magnetic measurements due to an almost impossible electric coupling for E-field receivers surrounded by air. For ground-based field surveys, commonly the time derivate of the magnetic fields are derived which are proportional to an induced voltage V_{ind} of a receiving induction coil which is set up perpendicular to the direction of interest. This proportionality is depending on the area of the coil loop A, the number of windings N and μ as

$$V_{ind} = -N\,A\,\mu\,\partial_t H_i\,, \quad i \in (x, y, z). \tag{2.68}$$

In time domain methods, the magnetic flux density $\mathbf{B}$ can be recorded as well. *Rochlitz et al.* (2018) investigated the capabilities of low-temperature SQUID[1]-based magnetic field receivers in an urban area and compared the results to induction coil results. In their study, SQUID-based $\mathbf{B}$-field data exhibits a superior data quality especially at late times. Nonetheless, coil measurements and a subsequent derivation of $\partial_t\mathbf{H}$, i.e. the partial time derivative of $\mathbf{H}$, are still the standard receiving method in ground-based time domain EM surveys along with the electric field $\mathbf{E}$. Therefore, this thesis concentrates on forward modeling studies of $\partial_t\mathbf{H}$ and $\mathbf{E}$.

There are four common techniques for solving Maxwell's equations in the time domain (*Börner*, 2010).

- *Explicit* time-stepping
- *Implicit* time-stepping
- Matrix exponentials / *Lanczos* reduction
- *Fourier* transform based methods

The simplest method for discretizing partial differential equations in time is the explicit time-stepping method using the *forward Euler* algorithm where the state of a system is calculated at a later time explictly from the state of the system at the current time. Explicit methods are comparably easy to implement but require usually very small time steps. They are computationally expensive and only stable if the time step $\Delta t \leq ch^2$, where c is a material constant containing the conductivity, and h denotes the smallest grid spacing (*Mulder et al.*, 2008). The DuFort-Frankel method helps getting around the strict stability condition by adding an artificial light-speed term that allows the time step

[1]Superconducting Quantum Interference Device

to grow with the square root of time without losing too much accuracy (*Mulder et al.*, 2008).

On the other hand, implicit methods like the *backward Euler* or the *Crank-Nicolson* method calculate the desired solution of a function involving the current system's state and the one at a later time. Implicit methods can be computationally more expensive than explicit methods but they can significantly increase the accuracy of the solution (*Börner et al.*, 2015). Examples for the application of the Euler backward method in CSEM time domain modeling are *Haber et al.* (2007) using finite volumes and *Um et al.* (2010) using finite elements.

Druskin and Knizhnerman (1988) proposed an alternative technique to time-stepping with their so-called *Spectral Lanczos Decomposition Method* (SLDM) on finite difference grids using Krylov subspaces. Here, the Lanczos method reduces the original sparse matrix into a smaller and denser matrix which is then used to calculate time evolution using matrix exponentials. According to *Börner et al.* (2008), the convergence of the SLDM depends mainly on the conductivity contrasts of the subsurface model. To improve convergence, the finite difference grids have to be very fine near jumps of electrical conductivity within the discretized region. No time discretization is necessary, therefore the size of time steps can be chosen arbitrarily (*Börner*, 2010). One drawback is that SLD methods cannot be used with adaptive mesh refinements (*Mulder et al.*, 2008).

Fourier transform based methods, or, to be more precise, their inverse transforms, convert frequency domain data into the time domain. This implementation approach is very common in time domain CSEM modeling, see Chapter 1.1. The group of Fourier-based transforms include sine/cosine, Laplace and Hankel transforms. Over the last decades, the greatest challenge of these approaches in 3D CSEM modeling was that for a solution, a large number of logarithmically equidistant frequencies has to be calculated. But with todays available parallel computational power this issue is more and more downsized. The transforms themselves are of negligible computational effort compared to the calculation of a certain number of frequency domain solutions.

Mulder et al. (2008) have analysed and compared the computational complexity of the different aforementioned numerical methods of modeling time domain CSEM diffusion problems. The authors state that a Fourier transform based conversion of frequency domain data may be an attractive approach depending on the required number of frequencies and discuss an adaptive frequency reduction technique.

A comparison of different Hankel and Fourier transform methods was presented by *Werthmüller* (2017) who proposed that the Fast Hankel Transform using digital filters is the best approach in terms of speed and precision for frequencies in the range of CSEM modeling.

2.4.2. Transformation into the Time Domain

In time domain (or transient) CSEM, two different current modes are usually distinguished: The switch-on and switch-off function. These two current functions are related with each other and with the direct current (DC) level as

$$f_{off} = f_{DC} - f_{on} \tag{2.69}$$

In case of a step-off signal, the current injected by the transmitter is assumed to be constant at times $t < 0$ and switched off at $t = 0$. On the other hand, in case of a step-on signal the current is switched off at times $t < 0$ and switched on at $t = 0$. In practice, both switching modes do not act instantaneously, they need a finite amount of time to reach their destination current level (zero or the DC level). During this specific time span, time-varying EM signales are being recorded. When a transmitter is operated in 100 % duty cycle, i.e. switching polarities without to pause transmitting, only step-on signals are instantiated. For other duty cycles like the very common 50 % duty cycle, both, the step-on signal and the step-off signal, are realized. The advantage of the switch-off mode is that no measured signal at a receiver position is superimposed by the primary EM field. Additionally, as stated by *Lippert* (2015), step-off functions of modern transmitters are usually faster and cleaner than step-on functions.

In case of linear equidistant sampled frequency data, a classical Fourier Transform (FT, see Eq. 2.12 and 2.13) or a Fast Fourier transform (FFT) would serve as a procedure of choice to transform the frequency data into the time domain. However, in transient or time domain CSEM, the time series usually consists of logarithmically equidistant time channels. In that case, the Fast Hankel Transform is superior to the FT. The reason behind is that the data points of the time series at late times are controlled by the lower frequencies of the source data. And to describe the frequency data for small abscissa values, a rather small sampling rate is required. In case of a FT or FFT, the small sampling rate needs to be kept constant throughout the entire frequency domain which would lead to a huge number of samplings in logarithmic scales. The FHT needs significantly less data points to provide comparable results (*Hönig*, 2002).

The switch-on excitation function of a current dipole source can be described by a Heaviside function in time domain by:

$$F_{on}(t) = \begin{cases} 0 & t < 0 \\ F_0 & t > 0 \end{cases}. \tag{2.70}$$

If the frequency domain function $F(\omega)$ is sufficiently smooth, it can be expressed by an inverse Fourier-transformed version (*Rätz*, 2000):

$$f(t) = \frac{1}{2\pi} \int_{-\infty}^{+\infty} \frac{F(\omega)}{i\omega} e^{-i\omega t}\, d\omega \tag{2.71}$$

with $1/i\omega$ denoting the Laplace Transformation of the excitation function (2.70). Applying *Euler's formula* $e^{ix} = cos(x) + i\, sin(x)$ yields:

$$f(t) = \frac{2}{\pi} \int_0^{\infty} \Re \left(\frac{F(\omega)}{\omega} \right) sin(\omega t) d\omega \tag{2.72}$$

$$f(t) = \frac{2}{\pi} \int_0^{\infty} \Im \left(\frac{F(\omega)}{\omega} \right) cos(\omega t) d\omega \tag{2.73}$$

for $t > 0$. The time series can therefore by described by using either sine or cosine functions with the real part $\Re(F(\omega))$ and the imaginary part $\Im(F(\omega))$ of the complex-

valued function $F(\omega)$. By using

$$J_{-1/2}(x) = \sqrt{\frac{2}{\pi x}}\, cos(x) \tag{2.74}$$

$$J_{1/2}(x) = \sqrt{\frac{2}{\pi x}}\, sin(x), \tag{2.75}$$

the real and imaginary part of $f(t)$ can be expressed by Bessel integrals of the form:

$$f(t) = \sqrt{\frac{2t}{\pi}} \int_0^\infty \Re\left(\frac{F(\omega)}{\sqrt{\omega}}\right) J_{1/2}(\omega t)\, d\omega \tag{2.76}$$

$$f(t) = \sqrt{\frac{2t}{\pi}} \int_0^\infty \Im\left(\frac{F(\omega)}{\sqrt{\omega}}\right) J_{-1/2}(\omega t)\, d\omega. \tag{2.77}$$

By replacing $F(\omega)$ with

$$\hat{F}(\omega) = \sqrt{\frac{\pi}{2\omega t}}\, F(\omega) \tag{2.78}$$

both equations have the form of a Hankel transform

$$f(t) = \int_0^\infty \Re\left(\hat{F}(\omega)\right) J_{1/2}(\omega t)\, d\omega \tag{2.79}$$

$$f(t) = \int_0^\infty \Im\left(\hat{F}(\omega)\right) J_{-1/2}(\omega t)\, d\omega \tag{2.80}$$

and can now be used for an efficient calculation of $f(t)$ by applying the Fast Hankel Transform using digital filters as described in Chapter 2.3. According to *Key* (2012) and *Janser* (2017), Equation (2.79) is to be preferred due to aspects of numerical stability.

Using $\Re\left(\hat{F}(\omega)\right) = -\Im\left(i^{-1}\hat{F}(\omega)\right)$ yields

$$f(t) = -\int_0^\infty \Im\left(i^{-1}\hat{F}(\omega)\right) J_{1/2}(\omega t)\, d\omega. \tag{2.81}$$

Equation (2.81) is finally used for the calculation of $f(t)$.

The switch-off function $f_{off}(\omega)$ can be calculated in the frequency domain as:

$$f_{off}(\omega) = f_{on}(\omega_0) - f_{on}(\omega) \tag{2.82}$$

where ω_0 is the lowest available frequency near the static or *DC* case. Modeling time domain EM fields using the switch-off current mode needs a previously calculated constant (DC) field as described in *Um et al.* (2010).

In the course of this thesis, 80 filter coefficients provided by Tilman Hanstein are used for the numerical transformation from frequency to time domain using the FHT. For the calculation of 10 samples per decade and N_T denoting the total number of time channels to be calculated then r_m and k_n used in (2.67) have the following discrete values:

$$r_m = r_0 \cdot 10^{\frac{m-1}{10}}, \quad m \in \{1, 2, \ldots, N_T\} \tag{2.83}$$

$$k_n = \frac{1}{r_0} \cdot 10^{\frac{N_T - n}{10}}, \quad n \in \{1, 2, \ldots, N_T + 79\} \tag{2.84}$$

Here, r_0 is the first time channel to be calculated. If, for example, 4 decades of time domain data and 10 time channels per decade are desired, a total of $79+41 = 120$ frequencies have to be calculated for a single forward modeling. In Chapter 4.2, the potential of reducing this number of frequencies by interpolation and extrapolation techniques without losing time domain data quality is examined.

CHAPTER 3

The TDcustEM Algorithm

In this chapter, the TDcustEM algorithm and the required third-party software is introduced. The functionality of the algorithm is proved by comparing its results against analytic solutions for uniform half-spaces and against well-established 1D and 3D forward modeling codes EMUPLUS and SLDMEM for more complex models. The chapter closes with an examination of the algorithms runtime and memory demand. Like custEM, the TDcustEM software package is written in Python 3.

3.1. Overview

To get a first idea about how the algorithm works, Figure 3.1 shows a flowchart containing the main steps of the TDcustEM algorithm. In practice, every TDcustEM forward modeling starts with the definition of a set of preferences and parameters. The red ellipses in Figure 3.1 denote user input data which need to be provided in form of a predefined formatted text file. The user is required to set the meshing parameters like layers, anomalies, topography, and also the configuration parameters for a specific forward modeling like transmitter type (e.g. a rectangular loop or a dipole) and size, receiver type and position, minimum and maximum time channels, etc. Moreover, the custEM-specific parameters like the solution approach, the polynomial degree and boundary conditions need to be given. On top of that, the parameter file contains placeholders for miscellaneous information for each specific run like a descriptive name or the number of CPUs to be used for parallel computing. If the desired Earth model is made of 2D or 3D geometries, an individual mesh generation script needs to be created and executed. For a more detailed description of the mandatory and optional parameters to be provided in the input file, please refer to the TDcustEM and the custEM manual.

The blue nodes in Figure 3.1 represent actual operational steps of the algorithm. After the generation of the 3D mesh according to the input parameters, the particular frequencies for the computation are determined. The total number of frequencies depends on the number of digital filter coefficients (usually 80 in the course of this thesis) and the minimum and maximum time channels. Assuming to calculate 10 time channels per decade, this results

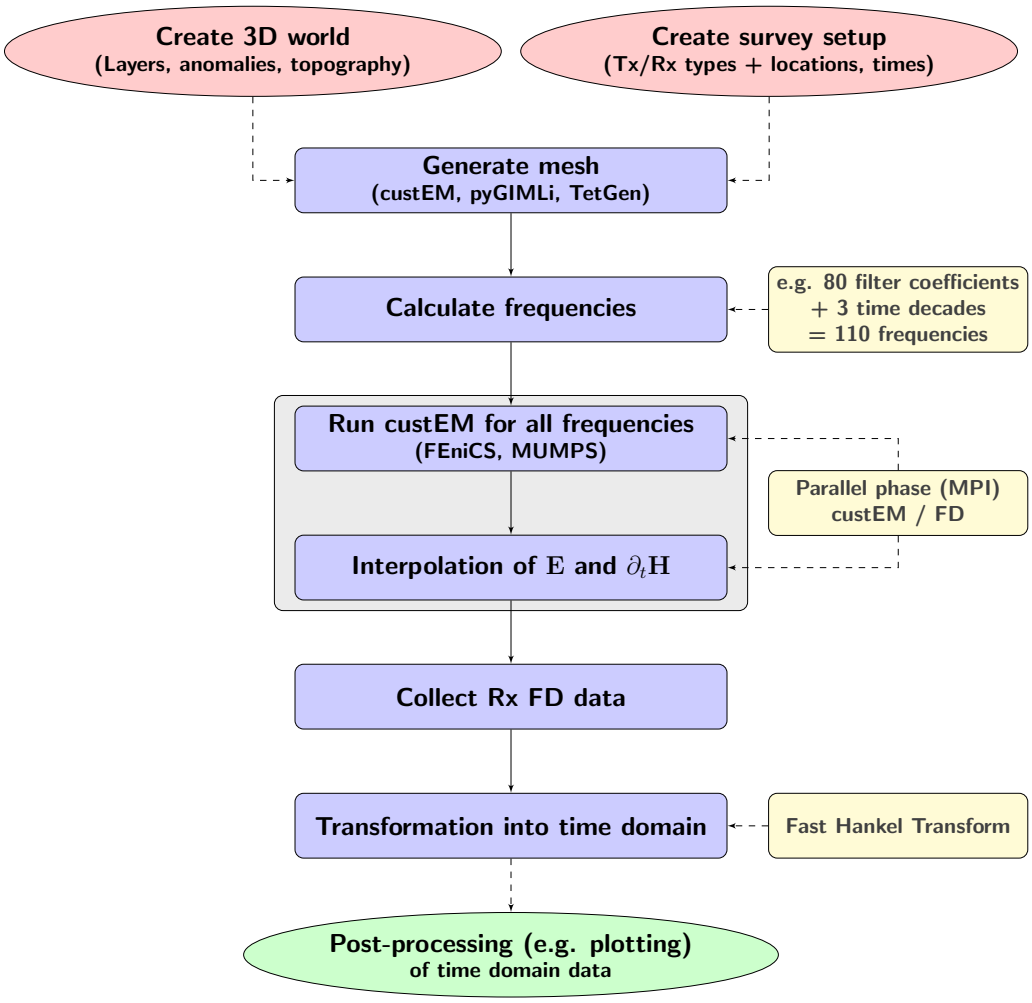

Figure 3.1.: *The TDcustEM algorithm flowchart: Red nodes denote user input, blue nodes automatic steps by the algorithm, comments are displayed in yellow nodes and an eventual post-processing in green. The gray-shaded area represents the parallel part of calculations processed by custEM.*

for example in 31 time channels when calculating transient data from $t_{min} = 10^{-5}\,s$ to $t_{max} = 10^{-2}\,s$. In this case, a total of 110 (Number of filter coefficients + the number of time channels - 1) frequencies needs to be computed.

In the next step, the custEM software is executed for each particular frequency. Here, the FEniCS framework and the MUMPS solver take action in the finite element calculation and solution. The custEM calculations are accomplished in the frequency domain for a predefined approach, e.g. the total E-field approach (see Chapter 2.1.3), other approaches that are implemented in custEM are not in the focus of this thesis. This step is the most expensive part of the entire procedure in terms of computational costs and therefore it is usually accomplished on a multiple number of CPUs using the common *MPI* interface. If requested by the user, after each custEM run the calculated $\mathbf{E}$ and the derived $\dot{\mathbf{H}}$ frequency domain data can optionally be interpolated. Interpolations are possible for arbitrary lines and planes within the entire 3D simulation domain.

After each custEM run, an FD dataset for the respective frequency is written to disk. These datasets contain the FD data for all tetrahedral elements of the 3D mesh and are therefore huge in terms of disk space. For all given receiver positions, the TDcustEM algorithms now collects the relevant data by crawling through the FD datasets.

In the final step, the algorithm transforms the modeled data from the frequency to the time domain by a Fast Hankel Transform (see Chapter 2.3). The resulting output of one forward modeling is written to a plain text file. For each receiver position, one text file is created. Each output file contains a header with meta information followed by seven columns of data: The first column contains the time vector with time channels from t_{min} to t_{max} and 10 time channels per decade. The following six columns contain three spatial components (x, y and z) of the electric field and three spatial components of the time derivative of the magnetic field.

Following *Um et al.* (2012), the magnetic permeability μ is kept constant and set to that of free space for all TDcustEM calculations within this thesis:

$$\mu = \mu_0 = 4\pi \cdot 10^{-7} \frac{Vs}{Am} \tag{3.1}$$

The electric conductivity $\sigma = \sigma(\mathbf{r})$ is implemented as a scalar function of space and therefore treated as isotropic. Implementing anisotropic conductivities in custEM, i.e. defining σ as a tensor, can be realized with little effort. But the investigation of anisotropic effects in 3D CSEM time domain modeling is not a subject of this thesis.

While most real-world problems in applied geophysics do not have natural boundaries, numerical simulations require a domain of finite volume $\Omega \subsetneq \mathbb{R}^3$ with boundary $\Gamma = \partial\Omega$. On the boundary Γ, the perfect conductor boundary condition

$$\mathbf{n} \times \mathbf{e} = \mathbf{0} \tag{3.2}$$

is imposed by default for the calculations throughout this thesis – if not stated otherwise. For each forward modeling, the domain size has to be chosen in the sense that the boundary is of sufficient distance to the source and receiver locations. If this is the case, the effects of the boundary conditions will be negligible.

The custEM toolbox offers an option to add a so called *bigger world* to the primary modeling domain. This additional domain is wrapped around the primary computation domain and consists of significantly larger tetrahedral elements, thus keeping the additional number of degrees of freedom and tetrahedra marginal. The bigger domain increases the entire 3D computing domain to greater sizes of for example two orders without increasing the corresponding total number of tetrahedra significantly. As an example, assuming that the "core" mesh has extents of 10^4 m in all directions, the bigger world domain would have extents of 10^6 m. The composition of a perfect conductor boundary condition (3.2) and huge domain extents due to this bigger world is assumed to be sufficient to disregard boundary effects at the modeled receiver positions. The effects of different domain sizes and boundary conditions on the data quality are investigated in Chapter 4.4.

3.2. Third-party Software

To enable TDcustEM (and custEM) to be executable on a computer system, a set of third-party programs (including FEniCS, TetGen, PyGIMLi, mpi4py and sympy) needs to be

installed. For more information on the installation process and software dependencies, please refer to the TDcustEM and the custEM manuals.

The fundament of the finite element calculations of the TDcustEM algorithm is FEniCS[2], a free and open-source computing platform. FEniCS provides a set of software tools, that allows for a rapid implementation and solution of PDEs using the finite element method. It was created in 2003 and developed in collaboration between researchers from universities and institutes around the world. For CSEM modeling, the most important interface of FEniCS is *DOLFIN* which provides an extensive library of Lagrange and curl-conforming Nédélec finite elements. FEniCS has built-in tools for the generation of different kinds of 3D meshes but also supports the usage of external mesh generators like *gmsh* or *TetGen*. FEniCS can be used with Python and C++ and it runs on all major operating systems.

TetGen (*Si*, 2015) is a state-of-the-art program to generate 3D tetrahedral meshes of any predefined domains consisting of so called *Piecewise Linear Complexes* (PLCs). PLCs are usually a set of vertices and non-intersecting segments and facets. TetGen has implemented methods for constructing *Delaunay* tetrahedralizations and quality tetrahedral meshes suitable for solving PDEs by the finite element or the finite volume method. Meshes generated with TetGen are subject to certain quality constraints for the size and shape of the mesh elements, e.g. aspect ratios (maximum edge length to minimum element height ratio) and radius-edge ratios (circumsphere radius compared to the length of the shortest edge) to avoid sliver tetrahedra. The source code of TetGen is freely available[3]. For the implementation of differently shaped electromagnetic transmitters and adding the according geometries to the generated meshes, custEM uses methods of *pyGIMLi*[4] (*Rücker et al.*, 2017) for the mesh generation with TetGen.

For the solution of a system of discrete equations like the discretized E-field equation system (2.42), FEniCS has built-in a number of direct and iterative solvers. In the course of this thesis, the parallel direct solver MUMPS[5] was used for all calculations.

The Python library *mpi4py* (MPI for Python) is necessary for parallel computing. MPI for Python provides bindings of the Message Passing Interface (MPI) standard for the Python programming language, allowing the usage of multiple processors at the same time. The Python library *sympy* serves as a library for symbolic mathematics which is utilized by custEM.

The time domain results calculated by the TDcustEM algorithm will be printed out as simple formatted text files. These files are only of small extent compared to the frequency domain data of custEM. The TDcustEM time domain results showed in this

[2]The FEniCS project (http://www.fenicsproject.org). FEniCS is an acronym where "FE" means Finite Elements and "CS" represents Computational Software. According to Anders Logg, one of the research scientists of the project, "the 'ni' sits nicely in the middle" (source.: https://answers.launchpad.net/fenics/+question/204935).

[3]TetGen: A Quality Tetrahedral Mesh Generator and a 3D Delaunay Triangulator (http://www.tetgen.org) by Hang Si of the Weierstrass Institute for Applied Analysis and Stochastics (WIAS).

[4]pyGIMLi: An open-source library for modelling and inversion in geophysics (http://www.pygimli.org).

[5]MUMPS: MUltifrontal Massively Parallel sparse direct Solver (http://mumps.enseeiht.fr/).

thesis have mainly been plotted using the *Matplotlib* Python 2D plotting library. For the optional visualization of the frequency domain data of custEM, it is recommended to use *ParaView*[6] which allows for an easy visualization of huge 3D datasets.

3.3. Cross-Validation

When *Rochlitz et al.* (2019) presented their first results calculated by the custEM algorithm, they proved the capabilities and the accuracy of custEM in the frequency domain by cross-validations of all implemented approaches against each other.

To ensure the reliability and accuracy of the developed time domain code TDcustEM, its results are cross-validated against analytic solutions and two different and well-established 1D and 3D time domain codes. A cross-validation of 2D subsurface models was omitted. The reason behind is that if the results of the 3D calculations are satisfactory, a cross-validation of 2D modelings is dispensable. Considering 1D forward modelings, the results are compared to the semi-analytic algorithm *EMUPLUS* (*Scholl*, 2005), a 1D modeling and inversion software package for different geophysical methods developed at the University of Cologne. The 3D results are compared to the code *SLDMEM* (*Druskin and Knizhnerman*, 1988, 1994, 1999), a 3D finite difference time domain code using a Krylov subspace projection technique and the *Spectral Lanczos Decomposition Method* (SLDM). Both, EMUPLUS and SLDMEM, are written in FORTRAN.

The figures presented on the following pages are usually made of the same design pattern: The results calculated by TDcustEM are displayed as dots of different colors while the corresponding validation results are displayed as gray solid lines in the upper part of the Figures. In the lower part of the figures, the relative differences between TDcustEM and the compared results are displayed in percent (see for example Figure 3.2).

3.3.1. 1D Cross-Validation with Analytic Solutions

As an initial validation, the TDcustEM results are compared to analytic solutions of $\dot{H}_z$ given by *Ward and Hohmann* (1991). The time derivate of the vertical magnetic field of an inductive loop transmitter on top of a homogeneous half-space in the center of the loop reads as

$$\frac{\partial}{\partial t} H_z\big|_{TxLoop} = -\frac{I}{\mu_0 \sigma a^3}\left[3\,erf(\theta a) - \frac{2}{\sqrt{\pi}}\theta a(3 + 2\,\theta^2 a^2)e^{-\theta^2 a^2}\right]. \tag{3.3}$$

The time derivate of the vertical magnetic field of an electric dipole source on top of a homogeneous half-space at distance y in the broadside[7] configuration reads

$$\frac{\partial}{\partial t} H_z\big|_{TxDipole} = \frac{Ids}{2\pi\mu_0\sigma}\frac{y}{r^5}\left[3\,erf(\theta r) - \frac{2}{\sqrt{\pi}}\theta r(3 + 2\,\theta^2 r^2)e^{-\theta^2 r^2}\right]. \tag{3.4}$$

[6] Paraview: an open-source, multi-platform data analysis and visualization application (http://www.paraview.org/).

[7] *Broadside* in this context means perpendicular to the transmitter dipole while *inline* means along the direction in that the transmitter dipole points.

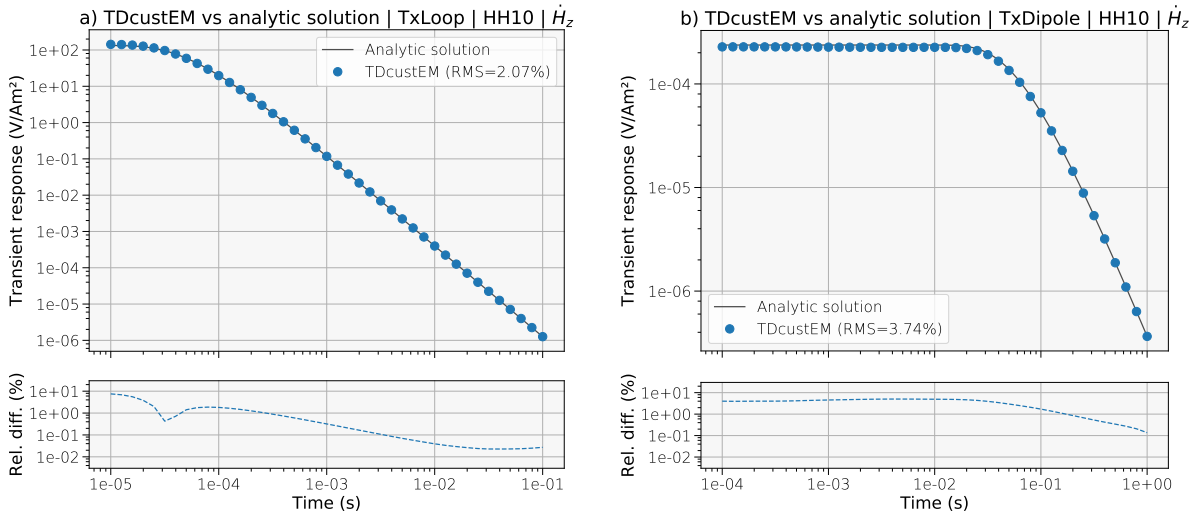

Figure 3.2.: *Comparison of TDcustEM forward calculations with analytic solutions after Ward and Hohmann (1991) for a homogeneous half-space of 10 Ωm. Left-hand side: An inductively coupled transmitter consisting of a* 100×100 m^2 *loop and a receiver in the central-loop configuration. Right-hand side: An electric dipole source of 1000 m length and a receiver in 2000 m distance (broadside). The injected current of both transmitters is 1 A. The upper images show the transient responses* ($\dot{H}_z$) *of the numerical and analytic solutions. The lower images show their relative differences in percent.*

where

$$\theta(\sigma, t) = \left[\frac{\mu_0 \, \sigma}{4 \, t}\right]^{1/2}. \tag{3.5}$$

I is the injected current, σ the homogeneous subsurface conductivity, a the equal circular transmitter radius of the rectangular loop transmitter, ds the length of the dipole transmitter in m, $r = \sqrt{x^2 + y^2}$ the receiver distance to the center of the dipole transmitter and t the time channels of interest. The error function erf is defined as

$$erf(x) = \frac{2}{\sqrt{\pi}} \int_0^x e^{-\tau^2} d\tau. \tag{3.6}$$

Figure 3.2a shows the analytic solution (gray solid line) and the TDcustEM forward modeled solution (blue dots) for a loop source transmitter and for times from 10^{-5} s to 10^{-1} s in the upper image. The lower image shows the relative difference between both time series in percent. The Root Mean Square (RMS) error between both time series is 2.07 % and is calculated after *Jupp and Vozoff* (1975) as:

$$RMS \;=\; \left[\frac{1}{N} \sum_{i=1}^{N} \frac{(f_i - d_i)^2}{d_i^2}\right]^{1/2}. \tag{3.7}$$

Here, f_i are the forward modeled values from TDcustEM and d_i the values from the analytic solution. N is the total number of values for each time series. Both time series agree to a satisfying degree, only for early times the solutions differ more than 1 %. Figure 3.2b shows the analytic solution (gray solid line) and the TDcustEM forward modeled solution (blue dots) for a dipole source transmitter and for times from 10^{-4} s to

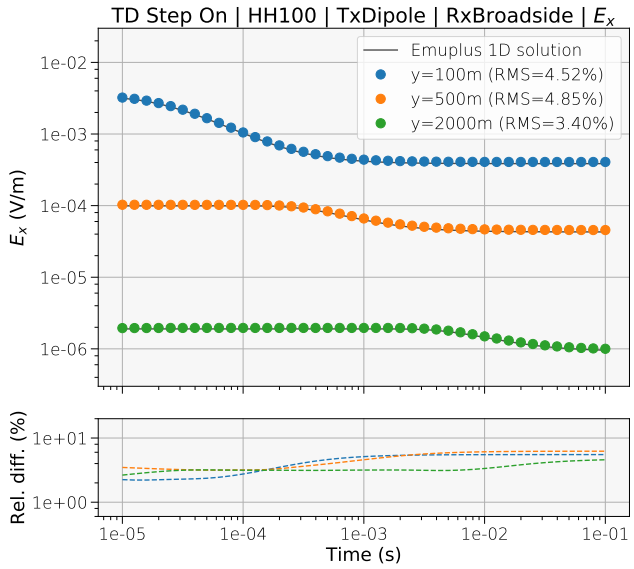

Figure 3.3: *Switch-on responses of a HED over a homogeneous half-space of 100 Ωm. The displayed component is the broadside E_x component for receiver distances of 100 (blue), 500 (orange) and 2000 m (green). The TDcustEM results were calculated using the total field approach and a polynomial degree of 1.*

1 s. Here, the RMS error between the numerical and analytic solution is slightly higher with 3.74 %.

Equations (3.3) and (3.4) are approximations of a vertical magnetic dipole (VMD) and a horizontal electric dipole (HED), respectively. Therefore, the results of the analytic solutions can only be confidently compared to modeled data (which is based on expanded transmitter geometries in 3D) in the far field. This explains the early time misfits between both simulations and the according analytic solutions in Figures 3.2 a and b.

For models more complex than the homogeneous half-space (even 1D layered subsurfaces), no analytic solution is known and their time domain responses need to be computed numerically. In the remaining part of this thesis, the time derivative of the magnetic flux density $\dot{\mathbf{B}}$ is displayed instead of the corresponding field strength $\dot{\mathbf{H}}$ because $\dot{\mathbf{B}}$ is the actually measured quantity in time domain CSEM field surveys. The time series in Figure 3.2 are an exception because the analytic solution of Equation (3.3) embodies the time derivative (impulse response) of the magnetic field strength $\dot{\mathbf{H}}$.

3.3.2. 1D Cross-Validation with EMUPLUS

In time domain electromagnetics, EMUPLUS can simulate transient responses for two different transmitter configurations: A VMD, approximated by a horizontal loop source and a HED, approximated by an extended horizontal bipole. During field surveys, VMDs are usually realized by a rectangular loop. In the forward modeling routine of EMUPLUS, they are replaced by circular loops of equal area. According to *Schaumann* (2001), this approximation is valid for times $t > 1$ μs and earlier times are not considered in this thesis.

The TDcustEM algorithm uses the E-field approach (Chapter 2.1.3) and therefore only the electric field quantities $\mathbf{E}$ are calculated directly. The values for $\dot{\mathbf{H}}$ (and $\dot{\mathbf{B}}$ respectively) are derived according to Equation (2.26). Hence, it is sufficient to cross-validate only the $\dot{\mathbf{H}}$ (or $\dot{\mathbf{B}}$) components because they are computed from the electric field.

Figure 3.3 is the only exception in the present chapter to validate the transformed electric field values. In this example, the transmitter is a 500 m long grounded dipole in x-direction centered around the origin with a current of 1 A. The subsurface model is a 100 Ωm homogeneous half-space and the displayed receivers are located broadside in distances of 100, 500 and 2000 m. The investigated component E_x is the switch-on response of the electric field parallel to the transmitter.

The transients of all three modelings have RMS errors between 3 and 5 % which is in an acceptable range. The TDcustEM results were calculated using the total field approach and a polynomial degree of 1. The underlying mesh was rather coarse with approximately only 30 k cells.

For the rest of this chapter, the time derivatives of the magnetic flux density **B** are investigated. Two different types of transmitters are modeled: A 500 m long grounded dipole (HED) acting as a galvanic coupled source and a 100 × 100 m^2 horizontal loop (VMD) acting as an inductively coupled source. Both transmitters are simulated with normalized currents of 1 A. The grounded dipole is located along the x-axis while both transmitter configurations are centered around the origin of the simulation domain. The air layer has a specific resistivity of 10^7 Ωm which is a sufficiently high value (*Rochlitz et al.*, 2019). If not stated otherwise, the total field approach was chosen and the polynomial degree was set to p = 1. The time range for the calculations was set to 10^{-5} s to 10^{-1} s (10 logarithmically equidistant time channels per decade) which is a typical range for time domain CSEM surveys of the chosen configurations. Regarding the plots, no attention was paid to sign reversals at this stage of the thesis and only the absolute values of the transients are displayed.

Homogeneous half-space

It is convenient to start the investigation of 1D layered subsurfaces with the homogeneous half-space because this is the most simple case to simulate. Figure 3.4 shows the transient response of a loop transmitter over a homogeneous half-space of 10 Ωm. The receiver is located in the center of the transmitter loop (central-loop configuration) and the displayed component is $\dot{B}_z$. For the chosen setup, the components $\dot{B}_x$ and $\dot{B}_y$ are supposed to be zero in the center of the transmitter loop. In 1D layered subsurfaces and using a horizontal transmitter loop, the induced currents inside the earth flow only horizontally. Hence, there is no vertical component of the electric field: $E_z = 0$ (everywhere) and $\dot{B}_x = \dot{B}_y = 0$ at the center of the loop. The RMS error between the TDcustEM results and EMUPLUS is only 0.47 % indicating a very good agreement between both algorithms. This RMS error is much smaller than the RMS value for the comparison of TDcustEM and the according analytic solution for a homogeneous half-space (Figure 3.2a) because in EMUPLUS the extended geometry of the source loop is represented as well.

The next step is to investigate laterally shifted receiver locations using an inductive source loop. Within this thesis, receiver positions inside the transmitter loop, but off-center, are denoted *in-loop positions* while receiver positions outside the transmitter loop are denoted *separate-loop positions*. Figure 3.5 shows the TDcustEM and EMUPLUS results for in-loop and separate-loop modelings. The left image shows the $\dot{B}_z$ transients of three different in-loop receiver offsets of 10 (blue), 20 (orange) and 40 m (green). All three transients look similar and they differ only at early times. The RMS errors are well below 1 % for all three in-loop offsets.

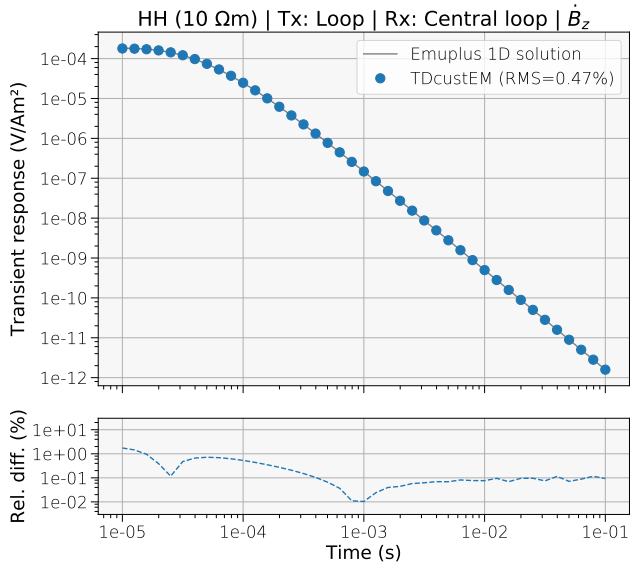

Figure 3.4: *Transient response (vertical component $\dot{B}_z$) of a central-loop setup on top of a homogeneous half-space of 10 Ωm. The TDcustEM result is displayed as blue dots while the EMUPLUS result is displayed as a solid gray line. The RMS error between both time series is 0.47 %.*

The right-hand side of Figure 3.5 shows the transient responses ($\dot{B}_z$) of three different separate-loop receiver offsets of 70 (blue), 100 (orange) and 200 m (green). Note that due to the geometry of the separate-loop setup, a sign reversal occurs within each transient. The closer the receiver is located to the transmitter loop, the earlier the sign reversal occurs. Sign reversals can usually be identified through a change of the transient's monotony when displaying only the absolute values in logarithmic scales. As stated before, the transmitter size was set to 100 × 100 m^2. Hence, every receiver offset > 50 m is located outside of the transmitter loop.

On average, the RMS errors for the separate-loop transients are larger than those for the in-loop transients, although the values for 70 m (RMS = 0.81 %) and 100 m (RMS = 1.22 %) are still satisfying. The large RMS error of the 200 m receiver can be attributed to the highly dynamical ranges around the sign reversal. This is confirmed by the relative differences of the TDcustEM transient compared to the EMUPLUS result (lower right part of Figure 3.5) where the relative difference is most prominent around the sign reversal with more than 10 %.

The impulse responses of the magnetic field for an exemplary LOTEM (Long-Offset Transient ElectroMagnetics) setup are displayed in Figure 3.6. Here, the TDcustEM results of a 500 m grounded dipole over a homogeneous half-space of 10 Ωm are compared to the 1D solution of EMUPLUS. The receivers are located broadside relative to the transmitter in distances of 100 (blue), 300 (orange) and 1000 m (green). On the left-hand side of Figure 3.6, the horizontal $\dot{B}_y$ component is shown while the right-hand side shows the vertical $\dot{B}_z$ component. The third component, $\dot{B}_x$ parallel to the transmitter dipole, is supposed to be zero for 1D subsurfaces at the investigated receiver locations.

The transients of the horizontal component $\dot{B}_y$ feature sign reversals for all three receiver locations and the TDcustEM results have RMS errors around 2 - 4 % compared to the EMUPLUS results. The transients of the vertical component $\dot{B}_z$ have straight forward shapes and the RMS errors are below 3 % for the modeled receivers. Therefore, both calculated components match the EMUPLUS results to a satisfying degree.

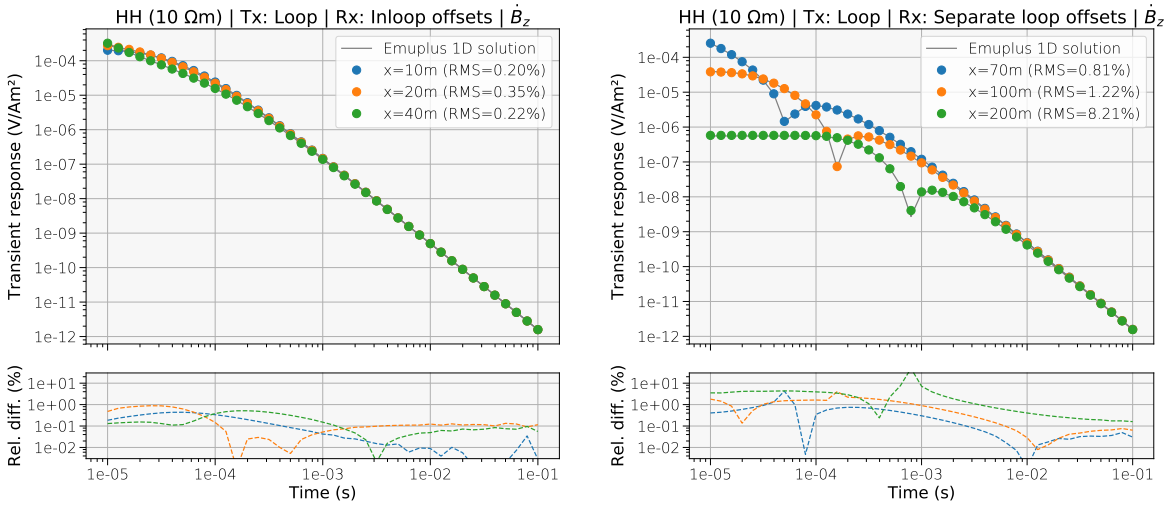

Figure 3.5.: *Transient responses (vertical component $\dot{B}_z$) of different receiver offsets for an in-loop (left-hand side) and a separate-loop (right-hand side) configuration on top of a homogeneous half-space of 10 Ωm using an inductive source loop (VMD). In the upper images, the TDcustEM results are displayed as colored dots while the corresponding results are displayed as solid gray lines. In the lower images, the relative differences of both results are displayed in percent.*

1D layered half-spaces

The next scope of 1D subsurfaces to be investigated are 1D layered half-spaces. In this chapter, the TDcustEM results for four different three-layer cases are cross-validated against 1D solutions from EMUPLUS. In Table 3.1, four different generic three-layer cases (H, K, A, Q) are listed. These kinds of 1D layered cases are commonly examined in applied geophysics.

The H model consists of a relatively conductive (10 Ωm) second layer in comparison to a more resistive first and third layer (both 100 Ωm). In contrast, the K model consists two conductive layers (10 Ωm each) surrounding a resistive second layer with 100 Ωm.

Model	Layer	Resist. [Ωm]	Thickn. [m]
H	1	100	40
	2	10	40
	3	100	

Model	Layer	Resist. [Ωm]	Thickn. [m]
K	1	10	40
	2	100	40
	3	10	

Model	Layer	Resist. [Ωm]	Thickn. [m]
A	1	1	40
	2	10	40
	3	100	

Model	Layer	Resist. [Ωm]	Thickn. [m]
Q	1	100	40
	2	10	40
	3	1	

Table 3.1.: *Resistivities and thicknesses of four different 1D three-layer models (H, K, A and Q).*

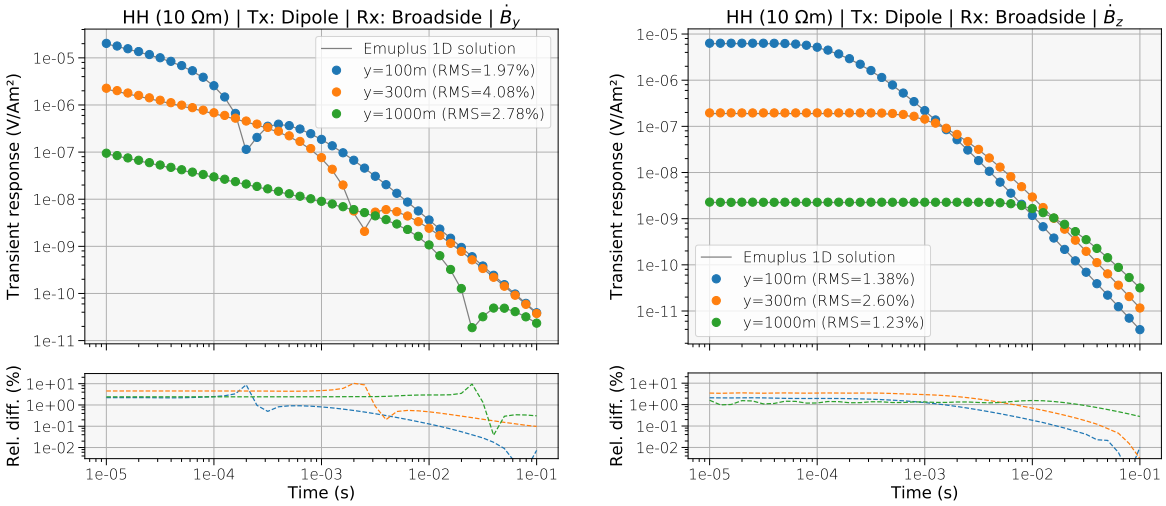

Figure 3.6.: *Transient responses of different broadside receiver offsets for a dipole transmitter configuration on top of a homogeneous half-space of 10 Ωm. On the left-hand side the $\dot{B}_y$ component is displayed and the right-hand side shows the $\dot{B}_z$ component. In the upper images, the TDcustEM results are displayed as colored dots while the corresponding EMUPLUS results are displayed as solid gray lines. In the lower images, the relative differences of both results are displayed in percent.*

The A model has a very conductive first layer (1 Ωm) and the resistivities increase with depth (10 and 100 Ωm for the second and third layer). On the other hand, the Q model is made up from layers where the resistivity is decreasing with depth (100, 10 and 1 Ωm). Within all four models, the thicknesses of the first layer and the second layer is 40 m each.

The choice of values for the resistivities and thicknesses of these models was a tradeoff between universality and comparability on the one hand, and, taking into account that the models produce examinable transient data in the investigated time range on the other hand.

Figure 3.7 shows the comparison of the TDcustEM and EMUPLUS modelings ($\dot{B}_z$ component) for each of the four 1D models using a 100 × 100 m^2 loop source. Each image in Figure 3.7 shows two results: one transient represents a central-loop setup (blue) in the center of the transmitter and one transient represents a separate-loop setup (orange) with a receiver offset of 100 m.

The central-loop transients have solid RMS errors of around 1 % or less. The separate-loop transients of all four models show sign reversals from early to intermediate times but nonetheless their RMS errors are satisfactory with values below 1.5 %.

Figure 3.8 shows the results for the horizontal component $\dot{B}_y$, perpendicular to the transmitter which is a 500 m grounded dipole with an injected current of 1 A. Each image shows transients for three different broadside offsets of 100, 300 and 1000 m. All transients provide the expected geometrical sign reversals except the green transient (1000 m offset) of the Q model (bottom right image of Figure 3.8). Here, the sign reversal happens after the modeled time range due to the very conductive third layer of 1 Ωm.

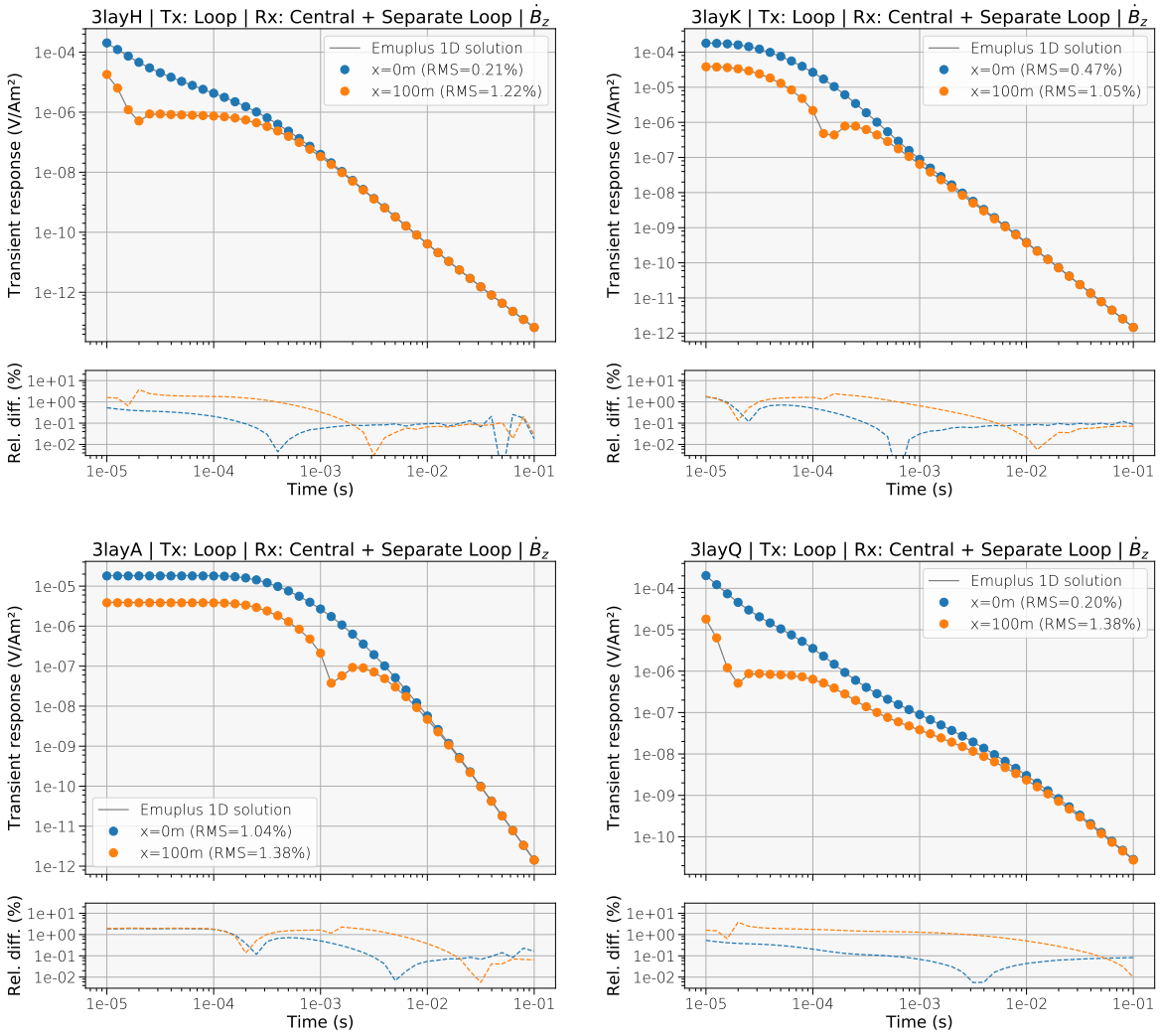

Figure 3.7.: *Transient responses (vertical component $\dot{B}_z$) of four generic three-layer subsurfaces (H, K, A, Q) using an inductive source loop. Each image shows the results of a central-loop setup (blue) and a separate-loop setup (orange) with a 100 m receiver offset. The TDcustEM results are displayed as colored dots while the corresponding EMUPLUS results are displayed as solid gray lines.*

The values of the RMS errors provide satisfying values of 1 - 5 % on average. Only the 100 m offset transients of the H and Q model have misfits between the TDcustEM and EMUPLUS results of more than 10 %. The reason behind is that both models consist of a relatively resistive first layer of 100 Ωm which leads to an earlier sign reversal, a steeper decaying slope and therefore to a higher dynamic of the transient compared to less resistive top layers. Generally, the numerical precision deteriorates when the computed physical parameter changes more rapidly in time.

The last setup for the cross-validation of 1D layered subsurfaces is a grounded dipole source (HED) as the transmitter and a broadside $\dot{B}_z$ as the receiver component. Figure 3.9 shows the corresponding results of three different receiver offsets for each of the four generic three-layer models as introduced in Table 3.1. The RMS errors between the

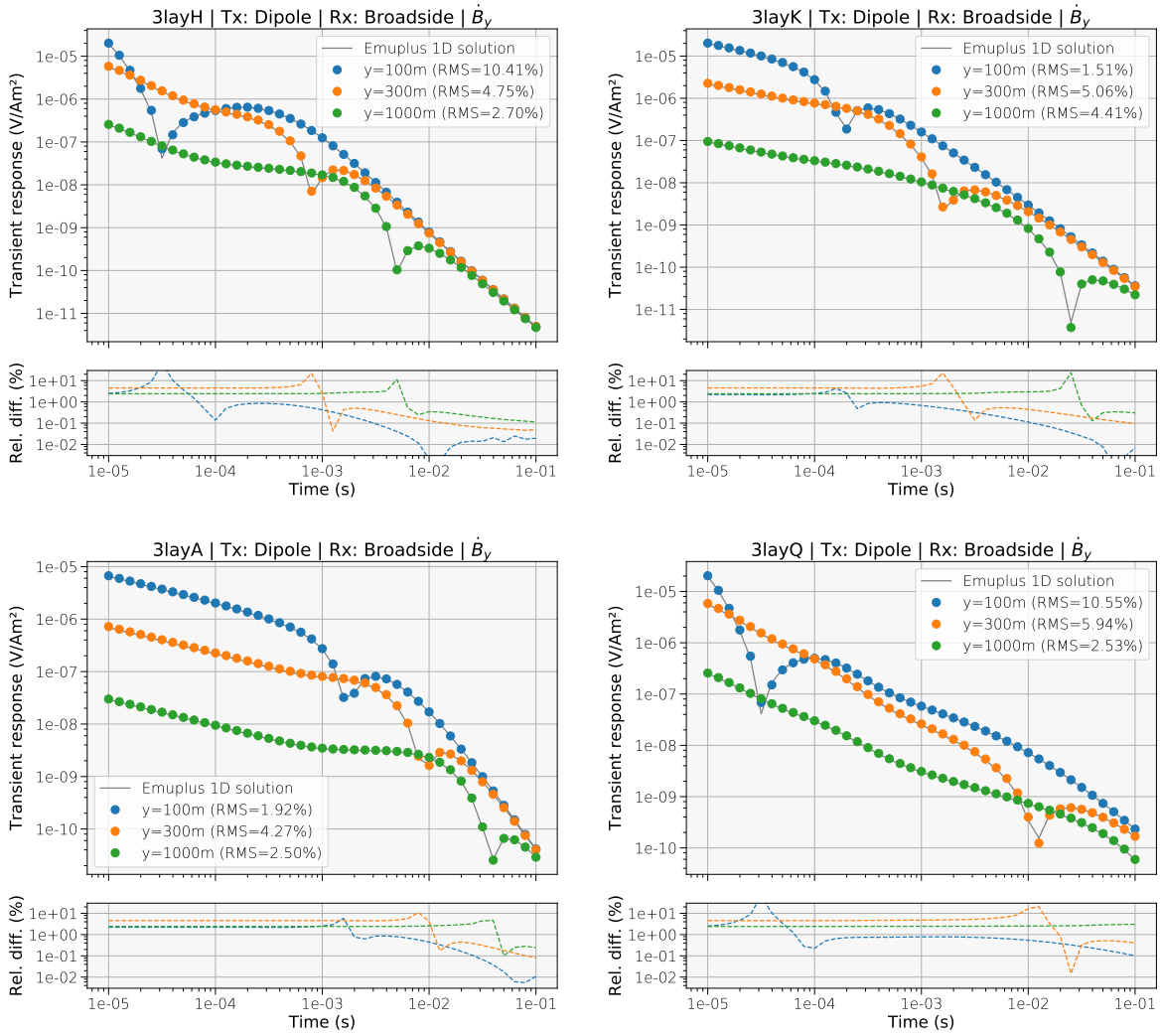

Figure 3.8.: *Transient responses (horizontal component $\dot{B}_y$) of four generic three-layer subsurfaces (H, K, A, Q) using a grounded dipole. The figure shows the results of the broadside $\dot{B}_y$ component with offsets of 100 (blue), 300 (orange) and 1000 m (green). The TDcustEM results are displayed as colored dots while the corresponding EMUPLUS results are displayed as solid gray lines.*

3D TDcustEM and the 1D EMUPLUS algorithms are in the range of 1 - 3 % which is a satisfactory outcome. The biggest contributions to these RMS errors between both algorithms comes from the relative differences at early times (see lower parts of each figure).

All in all, the presented 1D cross-validations between the 3D TDcustEM and 1D EMUPLUS algorithms show good results for the discussed models, setups and time ranges. While the results of the inductive loop transmitter modelings are accurate to a very satisfying degree, the comparisons of the grounded dipole source modelings lead to slightly higher RMS errors. The largest displayed RMS errors can usually be explained by the occurence of sign reversals. As stated before, it is numerically more demanding to provide accurate results for data points next to or in the vicinity of sign reversals.

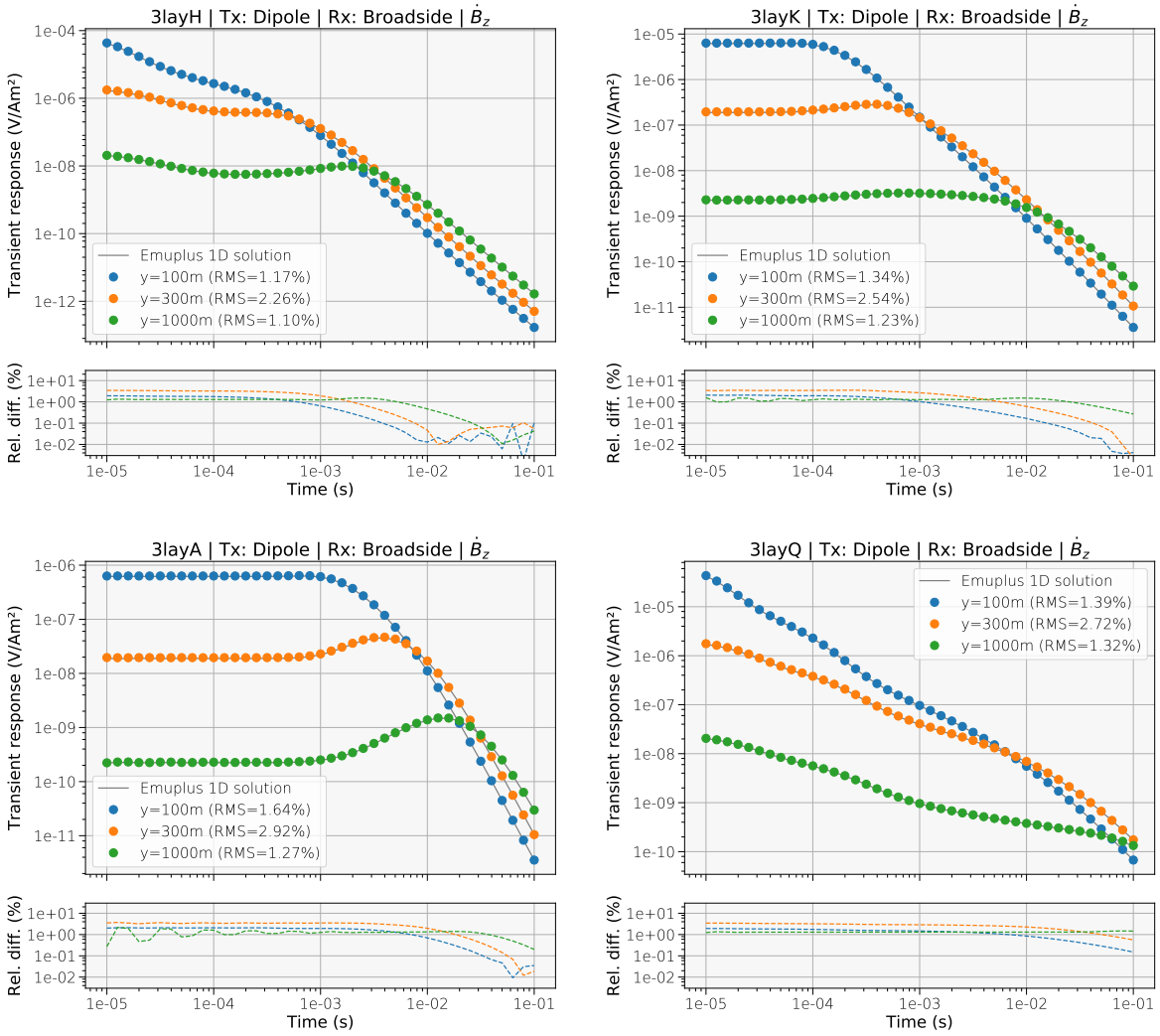

Figure 3.9.: *Transient responses (vertical component $\dot{B}_z$) of four generic three-layer subsurfaces (H, K, A, Q) using a grounded dipole. The figure shows the results of the broadside $\dot{B}_z$ component with offsets of 100 (blue), 300 (orange) and 1000 m (green). The TDcustEM results are displayed as colored dots while the corresponding EMUPLUS results are displayed as solid gray lines.*

One peculiar pattern of the modelings is that the 300 m receiver offset calculations using a HED transmitter provide generally larger RMS errors than the adjacent offsets of 100 m and 1000 m. Additionally, the relative difference plots of the grounded dipole modelings for the homogeneous half-space (Figure 3.6) and the 1D layered models (Figures 3.8 and 3.9) indicate larger differences between both algorithms mainly for the 300 m offset. This observation is possibly random but it may also be related to the chosen 3D mesh.

Using the RMS error (Equation 3.7) is one of several possible criterions to evaluate the quality of TDcustEM's results but it has some drawbacks. *Grayver et al.* (2013) presented the deficiencies of evaluations using the RMS error and concluded that RMS errors are

Conductive cuboid (Model A)	x [m]	y [m]	z [m]
Start	-25	50	-25
End	200	150	-75

Table 3.2.: *Start and end coordinates of the 3D conductive cuboid (1 Ωm) inside a homogeneous half-space (10 Ωm) for the 3D model A (separate-loop TEM).*

not the best choice when residuals[8] do not obey a standard normal distribution – which is the case in the vicinity of sign reversals.

One possible alternative to bypass large RMS errors caused by sign reversals is to use an error-weighted RMS-like criterion. In this case, data points adjacent or close to a sign reversal can be furnished with an additional relative error, see for example *Seidel and Tezkan* (2017) for such an approach.

3.3.3. 3D Cross-Validation with SLDMEM

In the following section, the 3D capabilities of the new algorithm are proved by comparing the TDcustEM results with the 3D finite difference time domain code SLDMEM[9] (*Druskin and Knizhnerman*, 1988, 1994, 1999). SLDMEM allows the computation of time domain CSEM data using a Krylov subspace projection technique. The algorithm is well established and has been used in many case studies over the last couple of years (*Hördt et al.*, 1992, 2000; *Yogeshwar and Tezkan*, 2017).

To get the most accurate early time results from the SLDMEM code, a grid needs to be dense around the transmitter. To allow for an additional good coverage of the late times, the grid needs also to be as large as possible. The generated meshes for the calculations in this chapter are therefore a tradeoff between both.

3D Model A: Separate-Loop TEM

The first investigated model A resembles a typical separate-loop TEM setup with several receiver locations outside of a squared transmitter loop. The subsurface consists of a conductive anomaly in form of a cuboid with a resistivity of 1 Ωm embedded inside a homogeneous half-space of 10 Ωm. The resistivities of both domains, the background half-space and the conductive anomaly, have been chosen to be relatively low to allow reasonable comparisons of the synthetic data also at late times. The conductive anomaly extends from a depth of 25 m to a depth of 75 m. The exact coordinates of the cuboid are given in Table 3.2. Although the chosen model and setup seem to be arbitrary, they are suitable for a cross-comparison of the two 3D algorithms. Because SLDMEM is a finite difference code and to avoid staircasing shapes, the subsurface model was chosen to have a regular, blocky structure. TDcustEM alone is not bound to these kind of limitations.

[8] In this case, the residual is the difference between the TDcustEM and the EMUPLUS results.

[9] The SLDMEM software suite can do forward calculations in the time domain and in the frequency domain. The corresponding codes are actually called SDLMEM3t and SLDMEM3f, respectively.

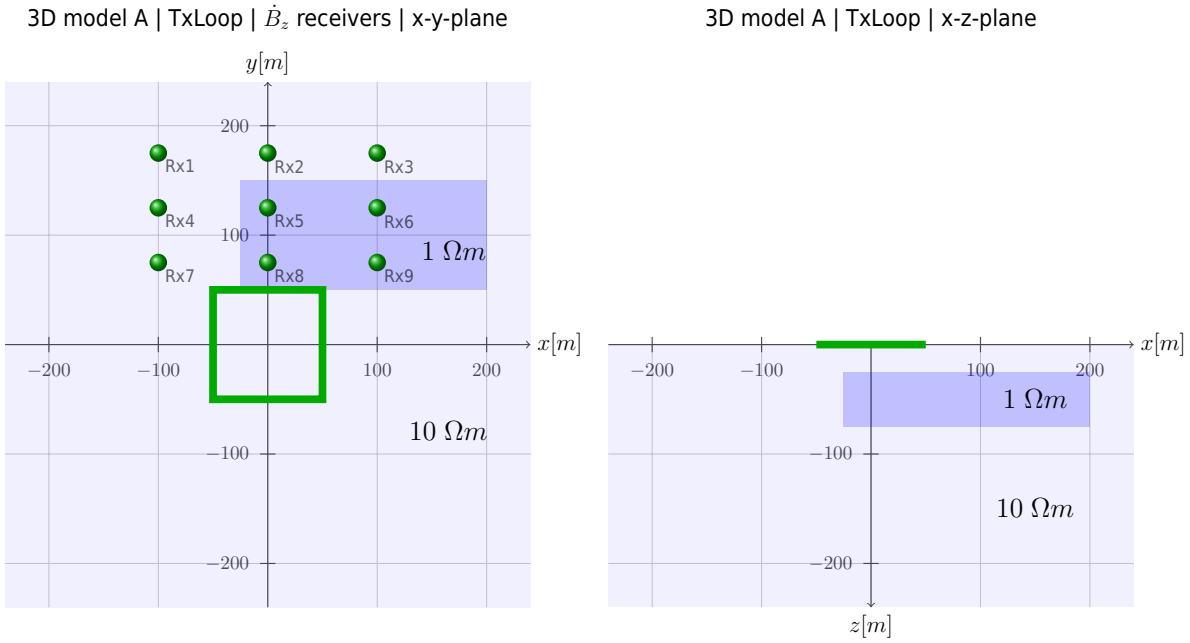

Figure 3.10.: *3D subsurface model A for a separate-loop TEM setup. The 100 × 100 m² transmitter is depicted as a green square in the x-y-plane (plan view, left image) and as a green line in the x-z-plane (cross-section, right image). The blue rectangle represents the position of the conductive anomaly, projected to the corresponding plane. The conductive cuboid is located 25 m underneath the surface, is 50 m thick and has a resistivity of 1 Ωm. It is embedded in a homogeneous half-space of 10 Ωm. The 3 × 3 $\dot{B}_z$ receiver locations are shown as green circles "north" of the source loop. They are partially covering the conductive anomaly.*

The chosen transmitter source is a 100 × 100 m^2 inductively coupled loop centered around the domain origin with an injected current of 1 A. The receivers are located along in a 3 × 3 separate-loop receiver grid at x = -100 m, x = 0 m and x = 100 m and y = 75 m, y = 125 m and y = 175 m. The receiver grid is partially covering the conductive anomaly. The modeled time range is 10^{-5} to 10^{-1} s and the investigated electromagnetic field component is the impulse response of the vertical magnetic field ($\dot{B}_z$).

Figure 3.10 (left-hand side) shows the described model A in the x-y-plane. The projected location of the conductive cuboid to the surface is displayed as a blue rectangle and the transmitter as a green square. The 3 × 3 receiver grid is shown as green circles. An x-z-plane view of the 3D separate-loop TEM model A is shown on the right-hand side of Figure 3.10. The projected location of the conductive cuboid is displayed again as a blue rectangle and the transmitter loop as a green line.

SLDMEM uses staggered grid Yee cells (*Yee*, 1966) on which the electric fields are edge-averaged while the magnetic fields are face-averaged. The size of the cells around the $\dot{B}_z$ receiver positions was 5 × 5 m^2 (in x and y directions). The grid was designed rather coarse around the magnetic receivers because the total number of gridlines is limited within SLDMEM and the grid had to support calculations in time over four decades. The size of the SLDMEM modeling domain was 5 × 5 × 5 km^3. Within the TDcustEM mesh, the tetrahedra adjacent to each receiver position has edge lengths of 1 m which leads to a much better resolution compared to the finite difference grid of SLDMEM.

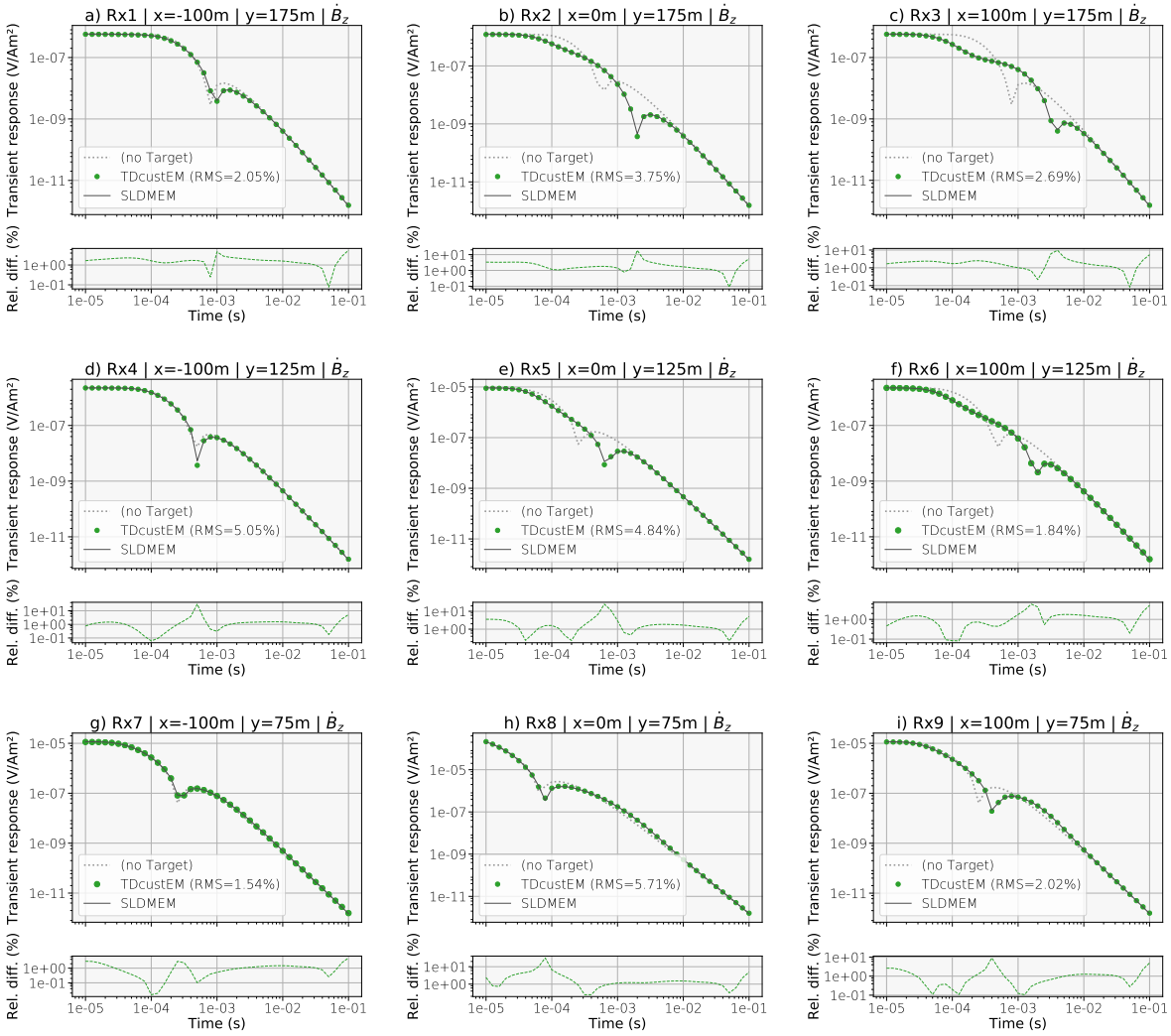

Figure 3.11.: *TDcustEM and SLDMEM comparison (vertical component $\dot{B}_z$) of the 3D loop transmitter model A for nine separate-loop receiver locations. The receiver grid is arranged as shown in the left-hand side image in Figure 3.10. The TDcustEM results are displayed as green dots and the SLDMEM data as gray solid lines. Transient curves for the homogeneous background ("no Target") case are displayed as gray dotted lines.*

The TDcustEM mesh used for the calculations consisted of $\sim$ 34 k tetrahedra and the modeling domain extents were 50 $\times$ 50 $\times$ 50 km^3. The polynomial degree was set to p = 2 using the total E-field approach.

The nine subfigures a - i in Figure 3.11 show the computed $\dot{B}_z$ transients of TDcustEM (green dots) and SLDMEM (solid gray lines) for each receiver position. The subfigures have been arranged in the same order than shown in the SLDMEM grid view of Figure 3.10. The corresponding RMS errors between TDcustEM's and SLDMEM's forward calculations are given in each subfigure's legend. Underneath the transients, the relative difference between both modelings is plotted.

To illustrate how much the transients are affected by the 3D geometry of the model, each subfigure contains an additional transient curve that shows the $\dot{B}_z$ data that would have been measured if no conductive cuboid was present (i.e. a transient decay curve for a homogeneous half-space of 10 Ωm). These additional transients have been calculated by TDcustEM and are plotted as gray dotted lines. The most prominent difference between the transients of the homogeneous case and the transients of the anomaly case are usually shifts in time of the geometrical sign reversal. As expected, receivers Rx4, Rx7 and Rx8 are least affected by the anomaly. The greatest impact can be seen at receiver location Rx3 where the sign reversal is shifted in time for almost half a decade. Additionally, the curve of Rx3 shows the most striking shape alteration compared to the homogeneous curve.

The RMS errors between both algorithms are below 6 % and sometimes only around 2 % which is a decent outcome taking into account that all transients provide a sign reversal. Looking at the relative difference plots underneath the curves reveals that the largest portions of the RMS errors again originate from the time channels around the sign reversals. On top of that, the very late times (the last or the last two time channels) contribute to higher RMS errors to a similar grade. These late time differences can probably be explained by a slightly poorer quality of the SLDMEM data because the SLDMEM domain is of much smaller extents and has a coarser resolution around the receivers. However, the calculated induced voltages at these very late times are often below the ambient noise level.

Model B: LOTEM dipole source

The investigated model for a typical LOTEM setup has a similar structure. Again, a conductive anomaly in form of a cuboid with a resistivity of 1 Ωm is embedded inside a homogeneous half-space of 10 Ωm. The conductive anomaly extends from a depth of 200 m to a depth of 400 m. The exact coordinates of the cuboid are given in Table 3.3.

The transmitter source is a 1 km long x-directed dipole centered at the domain origin with an injected current of 1 A. The receivers are located along in a 3 × 4 receiver grid at x = -0.5 km, x = 0 m and x = 0.5 km and y = 1 km, y = 1.5 km, y = 2 km and y = 2.5 km. The receiver grid is partially covering the conductive anomaly. The modeled time range is 10^{-4} to 1 s and the investigated electromagnetic field component is the broadside switch-on E_x component. SLDMEM is actually modeling only the switch-off response. The switch-on response was calculated using Eq. 2.69.

Figure 3.12 (left-hand side) shows the described model B in the x-y-plane. The projected location of the conductive cuboid is displayed as a blue rectangle and the transmitter as an orange line. The 3 × 4 receiver grid is represented by orange circles. An x-z-plane view of the 3D dipole source LOTEM model B is shown on the right-hand side of Figure 3.12.

Conductive cuboid (Model B)	x [km]	y [km]	z [km]
Start	0	0.5	-0.2
End	2	1.5	-0.4

Table 3.3.: *Start and end coordinates of the 3D conductive cuboid (1 Ωm) inside a homogeneous half-space (10 Ωm) for the 3D model B (LOTEM dipole source).*

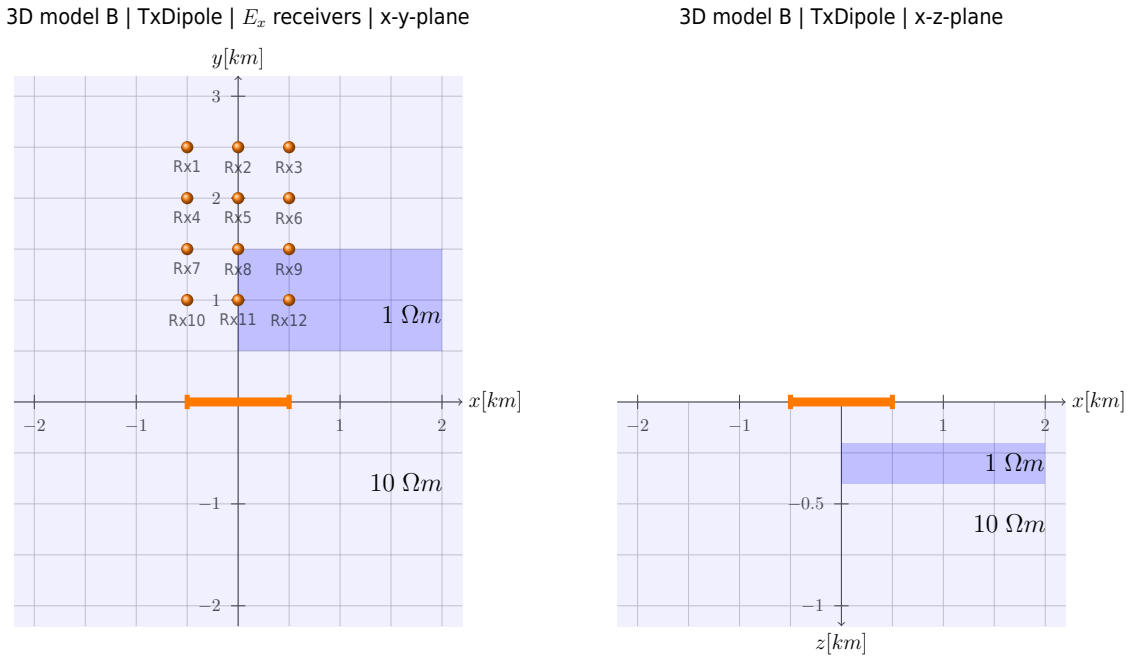

Figure 3.12.: *3D subsurface model B for a dipole transmitter LOTEM setup. The 1 km long x-directed source dipole is depicted as an orange line in the x-y-plane (plan view, left image) and in the x-z-plane (cross section, right image). The blue rectangle represents the position of the conductive anomaly, projected to the corresponding plane. The conductive cuboid is located 200 m underneath the surface, is 200 m thick and has a resistivity of 1 Ωm. It is embedded in a homogeneous half-space of 10 Ωm. The 3 × 4 broadside E_x receiver locations are shown as orange circles "north" of the source dipole. They are partially covering the conductive anomaly.*

The projected location of the conductive cuboid is displayed again as a blue rectangle and the transmitter dipole as an orange line.

The size of the SLDMEM modeling domain was 120 × 120 × 120 km^3. Within the TDcustEM mesh, the tetrahedra adjacent to each receiver position had edge lengths of 1 m. The TDcustEM mesh used for the calculations consisted of ∼ 100 k tetrahedra and the modeling domain extents were 750 × 750 × 750 km^3. The polynomial degree was set to p = 2 using the total E-field approach.

The subfigures in Figure 3.13 a - l show the computed switch-on E_x transients of TDcustEM (orange dots) and SLDMEM (solid gray lines) for each receiver position. The subfigures have been arranged in the same order than shown in the left image of Figure 3.12. The corresponding RMS errors between TDcustEM's and SLDMEM's forward calculations are given in each subfigure's legend. Underneath the transients, the relative difference between both modelings is plotted.

Like for the results for the separate-loop TEM model A, each subfigure contains an additional transient curve that shows the switch-on E_x data that would have been measured if no conductive cuboid was present (i.e. a transient switch-on curve for a homogeneous half-space of 10 Ωm). These additional transients have been calculated by TDcustEM and are plotted as gray dotted lines. The greatest impact of the anomaly can be seen at the receiver locations right on top of the conductive cuboid (Rx9 and Rx12). Addition-

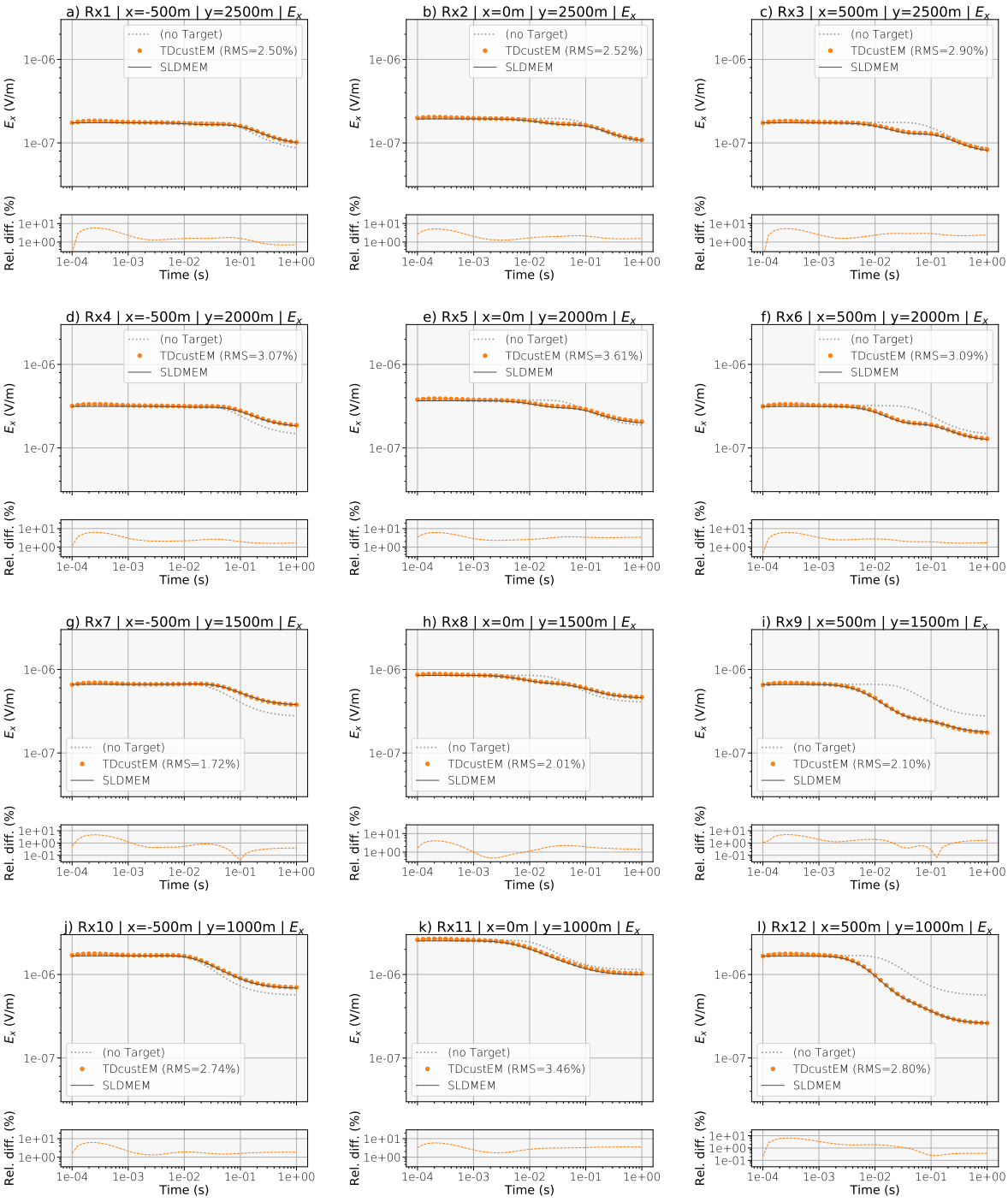

Figure 3.13.: *TDcustEM and SLDMEM comparison (switch-on broadside component E_x) of the 3D LOTEM dipole transmitter model B for twelve receiver locations. The receiver grid is arranged as shown in the left-hand side image in Figure 3.12. The TDcustEM results are displayed as orange dots and the SLDMEM data as gray solid lines. The relative differences of both forward modelings are plotted underneath every subfigure. Additional switch-on curves for the homogeneous background ("no Target") case are displayed as gray dotted lines for each receiver.*

ally, the transient curves of receiver locations Rx6 and Rx9 show the most striking shape alteration compared to the homogeneous curve.

The RMS errors in Figure 3.13 have values between 1.7 and 3.5 % which is satisfactory. A closer look to the relative differences in Figure 3.13 reveals that the RMS error comes mostly from the early times between 10^{-4} to 10^{-3} s. At these times, the TDcustEM values show a gentle oszillation at all receiver stations. The amplitudes of these oszillations depend primarily on the chosen mesh resolution. The finer the mesh is generated, the less is the degree of early time oszillations. Leaving out the first time decade for the calculation of the RMS errors, they would be reduced to 1.5 - 3 %.

For both comparisons of TDcustEM with SLDMEM (TEM model A and LOTEM model B), there seems to be room for a further improvement of the results by increasing the resolution of the underlying meshes or for example splitting up the forward calculation and mesh generation into two separate modelings: One for the first two time decades with an appropriate finer mesh and one for the last two time decades deploying a coarser but bigger mesh (multi-grid approach).

All in all, Figures 3.11 and 3.13 show decent results when comparing the TDcustEM results to those of SLDMEM. They prove that the TDcustEM algorithm is capable of computing forward modelings also for 3D subsurface models to a more than satisfactory degree. Together with the 1D results of Chapter 3.3.2 and the comparison to the analytic solution, it can be concluded that the TDcustEM algorithm delivers accurate and reliable multi-dimensional CSEM forward modeling data.

SLDMEM grid checks

As stated by *Yogeshwar* (2014), the finite differences grids used my SLDMEM have to be generated carefully to match a set of criteria like appropriate extents and local resolution to adapt to the chosen transmitter/receiver setup, the target time ranges and the given resistivity distributions.

To verify the applicability of the aforementioned grids and the SLDMEM numerical solution accuracy, the grids for the models A and B are tested in the way that the results of SLDMEM are compared to solutions of the semi-analytic algorithm EMUPLUS. As EMUPLUS is a 1D code, the comparisons are conducted for homogeneous half-spaces which are created omitting the conductive cuboids and have a resistivity of 10 Ωm (i.e. the background resistivity of both subsurface models).

For both models, the separate-loop TEM model A and the dipole transmitter LOTEM model B, the "western-most" receiver profiles with x = -100 m (model A, Rx1, Rx4 and Rx7) and x = -500 m, (model B, Rx1, Rx4, Rx7 and Rx10) have been chosen for this verification (see Figure 3.14). Due to the symmetry of the setup, the receivers of the "eastern" profiles have the same values as the receivers of the corresponding "western" profiles when forward modeling values for a uniform half-space (except for the sign, depending on the component). Investigating the results of a side profile seems to be more interesting than showing the results of the central profile due to the more complex geometry.

Figure 3.15 shows the $\dot{B}_z$ comparisons of three receiver locations (x = -100 m, y = 75, 125 and 175 m, loop model A) between the EMUPLUS and SLDMEM forward modelings for the 10 Ωm uniform half-space. The SLDMEM transients are displayed using colored

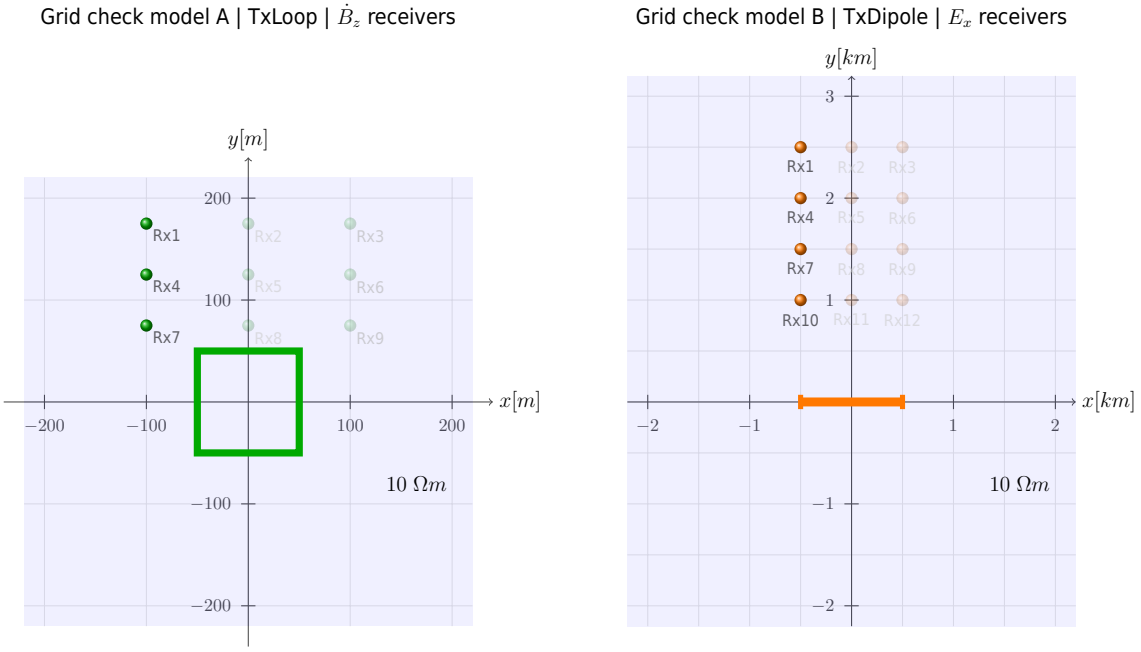

Figure 3.14.: *Simplified versions of the separate-loop TEM model A (left side) and the dipole source LOTEM model B (right side) for SLDMEM grid check comparisons with EMUPLUS. Only the "western-most" profiles are evaluated on a uniform half-space of 10 Ωm without the conductive anomalies.*

markers and the EMUPLUS transients as gray solid lines. The calculated RMS errors of each transient are given in the legend. The first value denotes the *regular* RMS error, taking into account every value of both particular time series. The second value denotes a reassessed RMS error for which the two adjacent values left and the two adjacent values right of each sign reversal have been excluded from the RMS calculation. This reassessment of the RMS error is a simple approach to increase its overall comparability.

Surprisingly, the RMS error of Rx1 at location y = 75 m increases from 1.25 to 1.3 % when leaving out the four values near the sign reversal. But the RMS values of the remaining two transients experience an expected improvement from 2.82 to 2.41 % (Rx2, y = 125 m) and from 5.09 to 2.39 % (Rx3, y = 175 m), respectively.

Selected switch-on E_x comparisons between SLDMEM and EMUPLUS for the dipole source LOTEM model B on top of a 10 Ωm uniform half-space are presented in Figure 3.16. The RMS errors between both algorithms for the receiver positions y = 1.5, 2 amd 2.5 km are 0.43, 0.66 and 0.88 %. Only the RMS error of the closest receiver location at y = 1 km has an increased value of 2.22 %. EMUPLUS is only capable of calculating electric fields for the switch-on case while SLDMEM is only capable of creating switch-off responses. Therefore, the SLDMEM results had to be transformed from a switch-off to a switch-on response to allow for a quantitative comparison.

Overall, the chosen SLDMEM grids for both models seem to be applicable for the cross-validations with TDcustEM, as shown in Chapter 3.3.3. The RMS errors for the loop model A are slighty higher than those of model B, which can partly be explained through the sign reversals, but they are still in a satisfactory range. The results for model B are

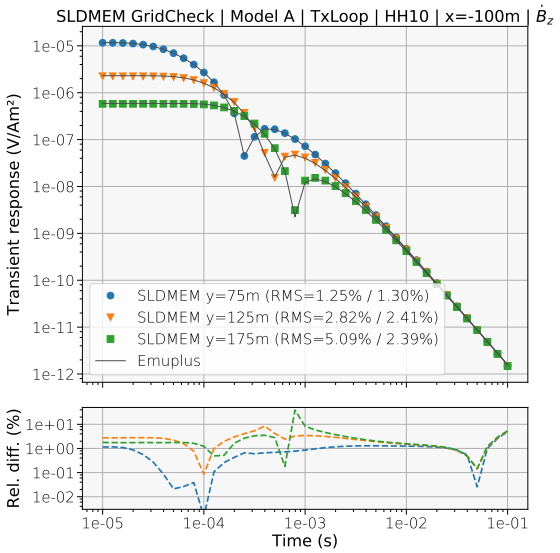

Figure 3.15.: *Grid check comparison ($\dot{B}_z$) between SLDMEM (colored marks) and EMUPLUS (grey solid lines) for the separate-loop TEM model A. The transients for three different receiver positions (Rx1, Rx4 and Rx7) of the "western-most" profile are plotted. The first RMS error is the regularly calculated value, the second RMS error is a reassessed version leaving out the four time channels next to the sign reversal.*

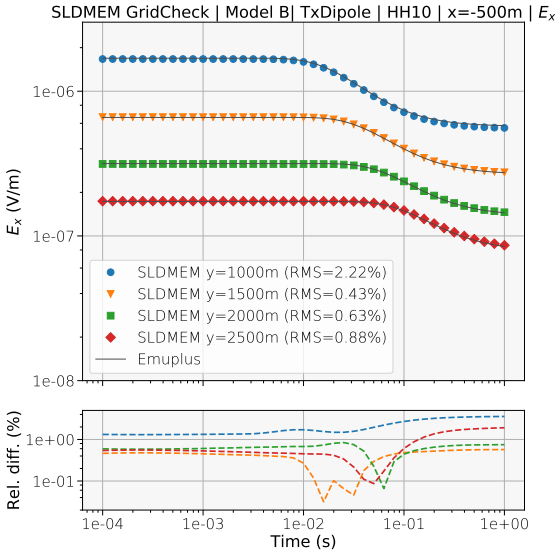

Figure 3.16.: *Grid check comparison (E_x) between SLDMEM (colored marks) and EMUPLUS (grey solid lines) for the dipole source LOTEM model B. The transients for four different receiver positions (Rx1, Rx4, Rx7 and Rx10) of the "western-most" profile are plotted. The presented time series do not provide any sign reversal. Therefore, in contrast to the RMS errors in Figure 3.15, only the regular RMS error is shown.*

much better with values below 1 % except for Rx10 at y = 1000 m with an RMS above 2 %. Here, the SLDMEM mesh could probably be optimized to reduce any discrepancy between the two algorithms. Yet, the results of the grid check comparisons show that the utilized SLDMEM grids are applicable to the chosen models and setups.

3.4. About Runtimes

The TDcustEM algorithm transforms 3D CSEM frequency domain data into the time domain using a Fast Hankel Transform. For this purpose, the custEM software has to be executed for a considerably large number of frequencies which can turn out to be time consuming depending on the size of the utilized 3D mesh and the number and speed of the parallel used CPUs. The relation between runtime and factors like the mesh size is examined below.

The presented benchmark results have been acquired on a Ubuntu 16.04.4 (Linux kernel release: 4.4.0-139-generic) server with 128 GB RAM using an Intel® Xeon® E5-2687W v3 CPU with 10 cores in parallel. Open MPI was used for parallel computations and the system equation set was solved by the direct solver MUMPS.

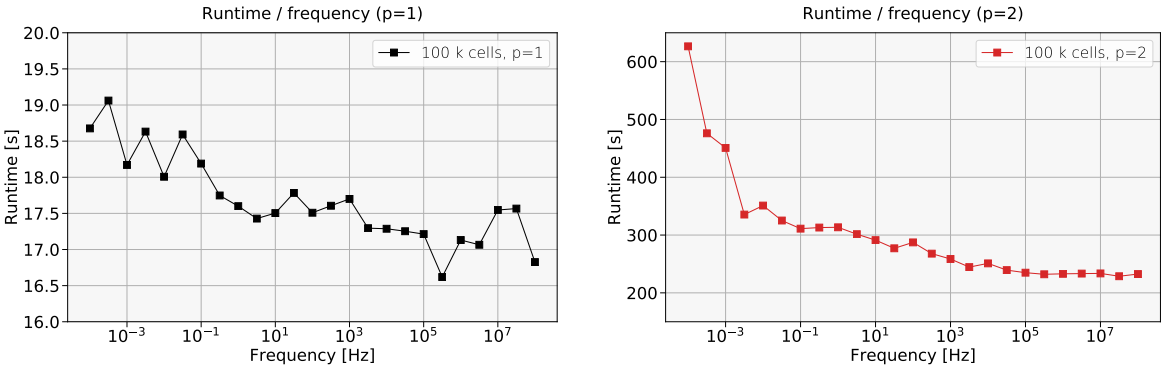

Figure 3.17.: *Single custEM runtimes depending on the frequency for polynomial degrees of p = 1 (left) and p = 2 (right) for a mesh with ∼ 100 k tetrahedra.*

First, the dependency of the runtime on a specific input frequency is investigated. Figure 3.17 shows the runtime in seconds for frequencies from 10^{-4} to 10^{8} Hz. The mesh used for these calculations consisted of ∼ 100 k cells. The image on the left-hand side of Figure 3.17 shows the result for p = 1. Here, the tendency that smaller frequencies need a longer runtime can be identified. For the polynomial degree of p = 2 this upward tendency is obvious. The reason is that for very small frequency values the condition of the system matrix deteriorates which complicates the numerical solution process.

Next, the parallel performance of custEM is investigated. For one fixed frequency of 1 Hz, the runtime in seconds depending on the parallel used cores from 2 to 20 is displayed in Figure 3.18 for the polynomial degrees of p = 1 (left image) and p = 2 (right image). The left-hand side of Figure 3.18 shows the runtime for three different mesh sizes from ∼ 50 k to ∼ 200 k tetrahedra. For the smallest mesh with 50 k cells, a runtime reduction of about 30 % using 4 cores can be observed. Using more cores does not lead to a significant speedup for this problem size. The same can be concluded for the double sized mesh with 100 k cells. Only for bigger meshes, like the 200 k cells mesh, a further speedup of the runtime is achieved by increasing the cores to approximately 10.

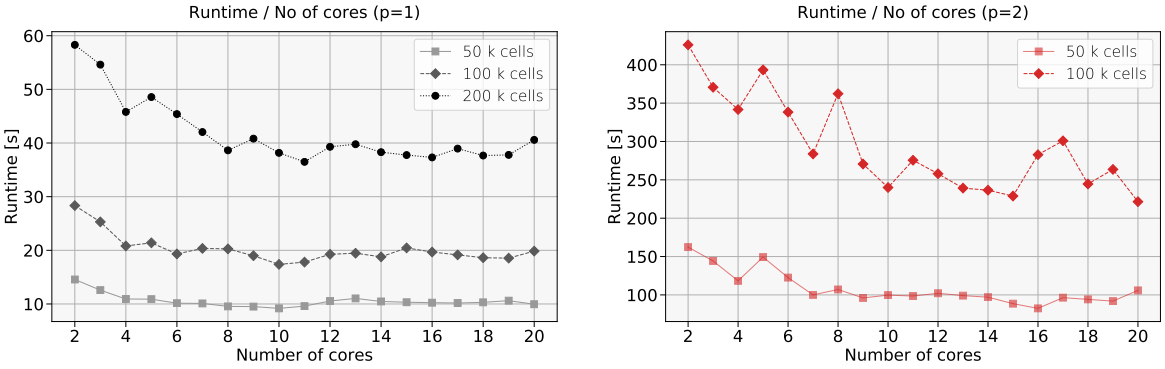

Figure 3.18.: *Single custEM runtime depending on the parallel used cores for polynomial degrees of p = 1 (left) and p = 2 (right) for different mesh sizes.*

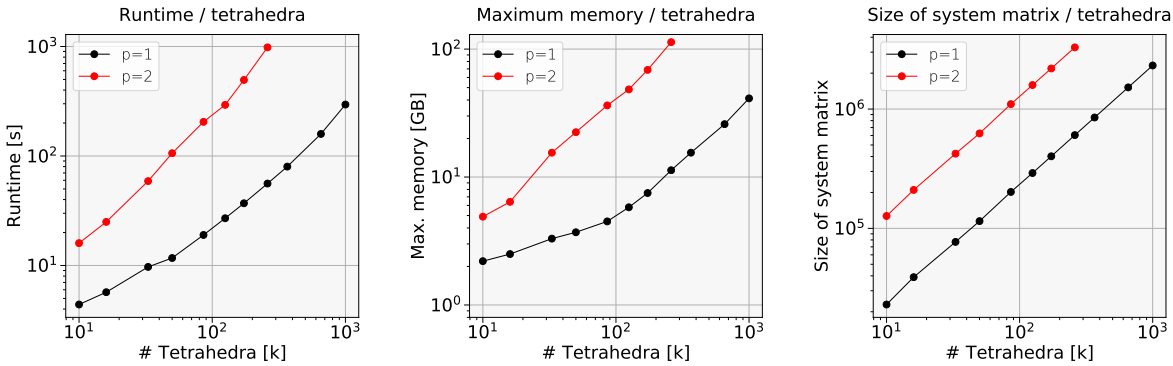

Figure 3.19.: *Runtime (left), memory usage (center) and size of the system matrix (right) displayed for different numbers of tetrahedra (in thousands) for polynomial degrees of p = 1 (black) and p = 2 (red). 10 CPU cores have been used for the parallel computation of one single frequency.*

For the polynomial degree of p = 2, two meshes have been investigated (right-hand side of Figure 3.18). For the 50 k cells mesh, a runtime speedup can be observed until increasing the number of cores to 7. For the 100 k cell mesh, a speedup is achieved until using 10 cores. A 200 k cell mesh was not investigated because its demand of memory would have been close to or greater than the total available memory of the utilized hardware. Demanding more memory than available would lead to a swapping of data to disk and eventually to an inconclusive evaluation of the runtime.

Achieving a runtime speedup by increasing the number of parallel used cores up to 10 is a satisfactory result. In some cases, an increasing number of cores leads to an unintentional increase of runtime. The driving factors of these limitations are the percentage of custEM's parallel portion, the overhead on communication between the MPI processes and the huge amount of frequency domain data which is written to disk. In the case of the present scenario, the underlying file system is the networked-based distributed file system "AFS" which may act as a bottleneck in terms of parallel computation speed.

The main outcome of the results displayed in Figure 3.18 is that a total number of 10 parallel used cores for a forward calculation seems to be enough on the utilized hardware. With this, an overall speedup factor of ~ 2 could be achieved.

Eventually, simple homogeneous half-space models have been created to investigate the impact of different mesh sizes with tetrahedral numbers from $10,000$ to $1,000,000$ on the runtime. The benchmarks have been generated for the polynomial degrees of p = 1 and p = 2.

Figure 3.19 shows the benchmark results for the measured runtimes (left), maximum memory usage (center) and the size of the system matrix (right). The values for the runtimes and the maximum memory usage are slightly fluctuating because they depend on unpredictable[10] factors like sparsity of the system matrix, the MPI handling, etc.

[10] "Unpredictable" in the sense that little changes of the input parameters may lead to significant changes in terms of runtime and memory usage

In qualitative regards, the results are sufficient to understand the memory needs and expected solving runtimes for meshes of different sizes.

The following example illustrates that one forward modeling in the time domain using TDcustEM may be computationally quite expensive: Assuming 80 filter coefficients and four time decades to simulate leads to a needed calculation of 120 frequencies. Using a 100 k cell mesh with a polynomial degree of p = 1 and 10 cores of the formerly mentioned CPU, one forward modeling would approximately take 40 minutes. For the same setup, and using the more precise polynomial degree of p = 2, the algorithm would need approximately six and a half hours to calculate solutions for 120 frequencies.

Even if the computing capabilities will increase within the next years, there is definitely the need of a runtime reduction. In this sense, the most obvious parameter to work on, despite reducing the size of the mesh, is reducing the necessary number of frequencies to simulate. Chapter 4.2 is discussing possible approaches.

CHAPTER 4

Synthetic Data Studies

This chapter shows various modeling studies regarding the evaluation of the implemented FHT filter coefficients and a possible reduction of the necessary number of frequencies by extrapolation and interpolation techniques is discussed. Following this, modeling studies regarding precise receiver positioning, reasonable domain sizes and resistivity contrasts are presented.

4.1. Testing different Filters

When using the digital filter algorithm of a Hankel Transform (Chapter 2.3), two factors determine the choice of the set of digital filters: The speed and the accuracy of forward modelings. The more coefficients a set of filters provides, the higher is the assumed accuracy. And on the other hand, the more time-consuming the forward modelings get. The calculations in the present thesis are usually using 80 filter coefficients provided by Tilman Hanstein[11]. Nowadays, typical filter set lengths contain a minimum of 50 to 100, on average 100 to 200 and in some cases up to a several hundred coefficients (*Key*, 2012; *Werthmüller*, 2017).

Zhao et al. (2018) investigated the performance of their newly developed 101- and 201-point sine and cosine filter sets. A comparison of their filters to the 101- and 201-point filters of *Key* (2012) showed that the new filters by *Zhao et al.* (2018) are superior when comparing transformed $\dot{H}_z$ data to the analytic solution of a horizontal electric dipole over a homogeneous half-space (Equation 3.4).

To evaluate the performance of the 80 filter coefficients by T. Hanstein, acting as the standard filter set in TDcustEM, they are compared to the two before mentioned filter sets by *Zhao et al.* (2018) containing 101 and 201 coefficients. For a quantitative comparison, the two analytic solutions for $\dot{H}_z$ presented in Chapter 3.3.1 (Eq. 3.3 and 3.4) for a loop and a dipole source are consulted. *Zhao et al.* (2018) published coefficients for the sine and

[11] Formerly working at the Institute of Geophysics and Meteorology, University of Cologne, now employed at KMS Technologies, Houston, Texas.

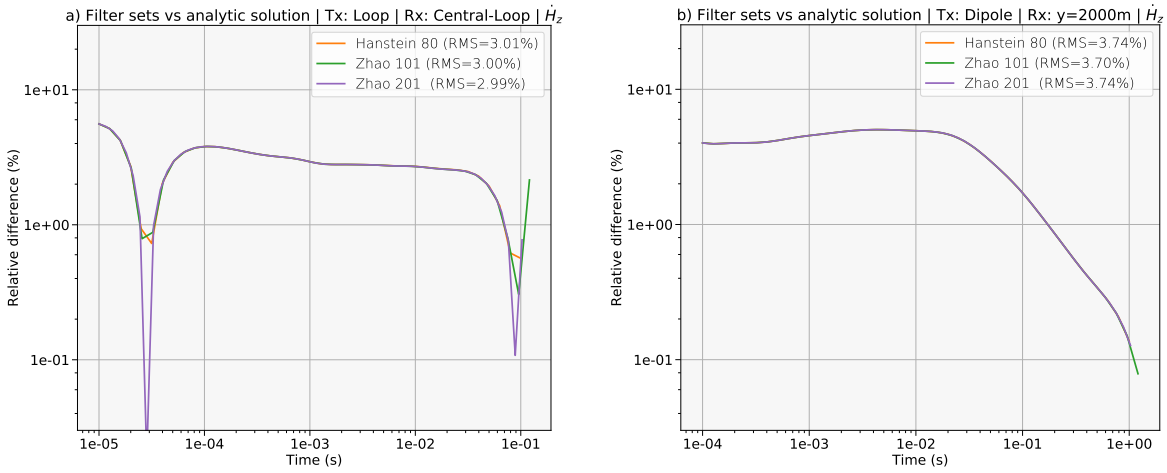

Figure 4.1.: *Comparing the performance of three filter sets for a loop and a dipole transmitter by calculating the relative difference between the transformed $\dot{H}_z$ data to an analytic solution for a homogeneous half-space of 10 Ωm. Left-hand side: Central-Loop TEM setup with a 100 × 100 m^2 loop source with an injected current of 1 A. Right-hand side: LOTEM setup with a 1000 m x-directed dipole transmitter and the receiver positioned 2000 m broadside. Each filter set produces time series of different lengths due to varying sampling intervals.*

the cosine transform, see Eq. (2.79) and (2.80), but in this Chapter only the coefficients of the sine transform are considered.

The 80 standard coefficients by T. Hanstein have been obtained to facilitate a computation of 10 time channels per decade, yielding an time increasing factor Q = exp(s) of

$$Q_{H80} = 10^{1/10} \approx 1.2589254 \tag{4.1}$$

in the time domain with s = the sampling interval in logarithmic space. However, the coefficients from *Zhao et al.* (2018) are designed for different sampling intervals $s_{Z101} = 0.235$ and $s_{Z201} = 0.149$. The resulting time increasing factors Q are:

$$Q_{Z101} \approx 1.2649088 \tag{4.2}$$

$$Q_{Z201} \approx 1.1606730. \tag{4.3}$$

The sampling interval for the Hanstein filter is $s_{H80} = \log(10^{1/10}) \approx 0.2302585$. These unequal sampling intervals implicate different time channels for the comparing forward modelings. Thus, for each filter set a different kernel function needs to be computed and an appropriate analytic solution had to be obtained to ensure an accurate comparison. For all TDcustEM modelings, the same mesh was taken and the polynomial degree was p = 2. For the 80-point Hanstein (*H80*) and the 101-point Zhao (*Z101*) filters, 41 sampling points have been computed. For the 201-point Zhao (*Z201*), 63 samples were required.

Figure 4.1 shows the performance of three filter sets as a relative difference of each filter set and the corresponding analytic solution in percent. The receiver for the loop source is located in the center of the transmitting loop (x = 0 m, y = 0 m) and the associated results are shown in Figure 4.1a. The receiver of the 1000 m long x-directed dipole source is located 2000 m broadside of the transmitter, the results for this setup are shown in

Figure 4.1b. Both setups have been calculated for a 10 Ωm uniform half-space. Additional to the relative difference per time channel, the RMS errors between the transformed data and the analytic solution are presented in the legends of Figure 4.1. The corresponding transients of both configurations can be found in Figure 3.2. Due to the different spatial scales of a central-loop TEM and a LOTEM setup, the time ranges have been chosen differently. The loop source data was computed from 10^{-5} to 10^{-1} s and the dipole source data from 10^{-4} to 1 s.

The loop source comparison (Figure 4.1a) shows a good agreement between the results of all three filters. Only at early times around 30 μs and at late times around 800 ms, the 201-point Zhao filter shows a marginal better performance. The differences of the RMS errors are neglectable with values from 2.99 to 3.01 %. The results of the dipole source comparison (Figure 4.1b) show a similar good agreement between the three filters. There are no significant differences in the performance of a filter at any time. Again, the RMS errors are on a comparable level with values between 3.70 and 3.74 %. For both setups, the RMS values can be treated as being approximately the same, taking into account that they are computed using different sampling points.

It can be concluded, that the default Hanstein filter with 80 coefficients provides as accurate results as the two Zhao filters with 101 and 201 coefficients, at least for the homogeneous half-space. But taking into account that a larger set of coefficients yields a longer computation time, the default Hanstein filter set is to be preferred. Eventually, all three filters are implemented in TDcustEM and can be used for the transformation into the time domain if desired. Moreover, additional sets of DLF coefficients can easily be implemented in TDcustEM.

4.2. An adequate Quantity of Frequencies

The following section is dealing with the possible reduction of the total number of frequencies to be calculated with TDcustEM without losing too much solution accuracy. Reducing the total number of frequencies would directly result in a significant speedup of a single time domain forward calculation. By default, TDcustEM is working with 10 frequencies per decade, which yields up to 130 mandatory frequencies on average - depending on the desired number of resulting time channels and when using 80 filter coefficients.

As stated in Section 2.4.2, it is numerically more stable to use the imaginary part of the frequency domain data for the Fast Hankel Transform. Therefore, an obvious question on how to reduce the necessary frequencies is: What is the impact on the transformed time domain result of modifying or entirely omitting individual frequency domain values?

One possible approach is to calculate only every second or every third frequency for example and interpolate the values in between. *Rätz* (2000) stated that 4 frequencies per decade are sufficient for an FHT of frequency domain data into the time domain.

Another approach is to omit for example the first or the last decade of frequencies and use extrapolation techniques to estimate these values. Within TDcustEM, typical FD data covers frequency ranges from 10^{-4} to 10^{8} Hz, which is a huge span and should intuitively comprise space for improvements.

The first investigation in the present chapter is to find out the weight of every frequency sample in the convolution for an exemplary frequency domain data set. Figure 4.2 shows the imaginary part of the H_z component of three FD data sets for different loop transmitter setups with a loop source of 100 × 100 m^2 and a current of 1 A.

The blue curve in Figure 4.2 shows the data for a central-loop configuration (x = 0 m, y = 0 m) on top of a homogeneous half-space of 100 Ωm. The data is monotonously rising for the first ∼ 8 decades and is then monotonously decreasing. The amplitudes cover values from approximately 10^{-11} to 10^{-2} A/m.

The FD data for a separate-loop setup (x = 0 m, y = 100 m) on top of a uniform half-space of 100 Ωm is displayed as an orange curve containing a sign reversal at approximately 30 kHz. Apart from that, the shape of the curve looks similar to that of the central-loop calculation (blue curve). The maximum amplitude is located at a similar frequency.

The last curve in Figure 4.2 is the green curve which belongs to receiver location Rx9 from the 3D subsurface TEM model A (see Figure 3.10). The shape of this curve is more complex than the previous two. It provides two sign reversals near 10 Hz and near 10 MHz and the global maximum amplitude is shifted more than 2 decades to lower frequencies.

To find out the convolutional weight of each frequency sample, every value from the original data series is multiplied one after another with a so-called Modification Factor (MF) of for example 10 % and then an FHT is conducted on this *modified* frequency domain data set. A more precise example: First, the data point of the lowest frequency is modified by for example 10 % and then the FHT is conducted. Afterwards, the time domain result is compared to the FHT time domain result of the original, unaltered frequency data set. The outcome of this comparison is quantified in terms of an RMS error. In a second step, the corresponding value of the next frequency is modified by the MF and again an RMS between the modified data and the original data is computed, and so on. All RMS errors of these single variations are eventually plotted as a function of the frequency.

For each curve in Figure 4.2, the above mentioned RMS errors per frequency are shown in Figure 4.3 a-c. The blue curves in Subfigure 4.3a correspond to the blue curve of Figure 4.2, the orange curves in 4.3b correspond to the orange curve in 4.2, etc. The RMS errors have been computed for modification factors of 10 % (dotted lines), 100 % (dashed lines) and 1000 % (solid lines). A horizontal black line represents the RMS error = 1 % level in each subfigure.

An important outcome of the results in Figure 4.3 is that modifying single frequency values higher than 10^7 Hz and lower than 10^{-2} Hz even by 1000 % has almost no impact (RMS errors $< 10^{-7}$ %) on the time domain result after the FHT. The frequencies with the greatest impact for these kinds of loop source modelings are in the range of 10 Hz to 1 MHz.

The next investigation is to find out the importances of frequencies for different 1 km long x-directed dipole transmitter (LOTEM) setups with a 1 A current. Figure 4.4 shows the imaginary part of the H_z and E_x components of three exemplary FD data sets for different dipole transmitter configurations. The blue (H_z) and orange (E_x) curves belong the broadside receiver locations at x = 0 m and y = 1000 m for a homogeneous half-space of 100 Ωm. The green curve corresponds to data from receiver location Rx12 (x = 500 m, y = 1000 m) of the LOTEM model B (Figure 3.12).

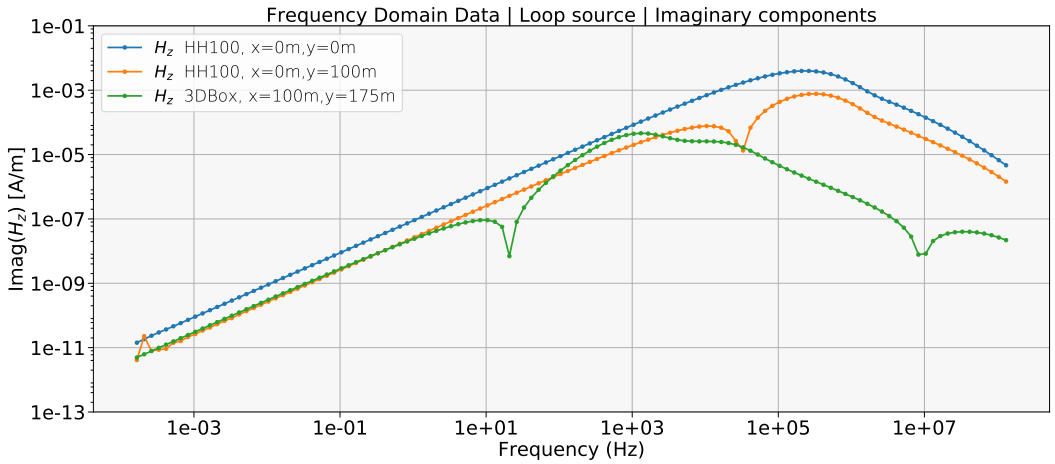

Figure 4.2.: *Frequency domain data (imaginary part of the H_z component) of three different loop source setups. Blue: Homogeneous half-space of 100 Ωm in the central-loop configuration. Orange: Homogeneous half-space of 100 Ωm in the separate-loop configuration with an offset of y = 100 m. Green: Rx9 from the 3D TEM model A (see Figure 3.10).*

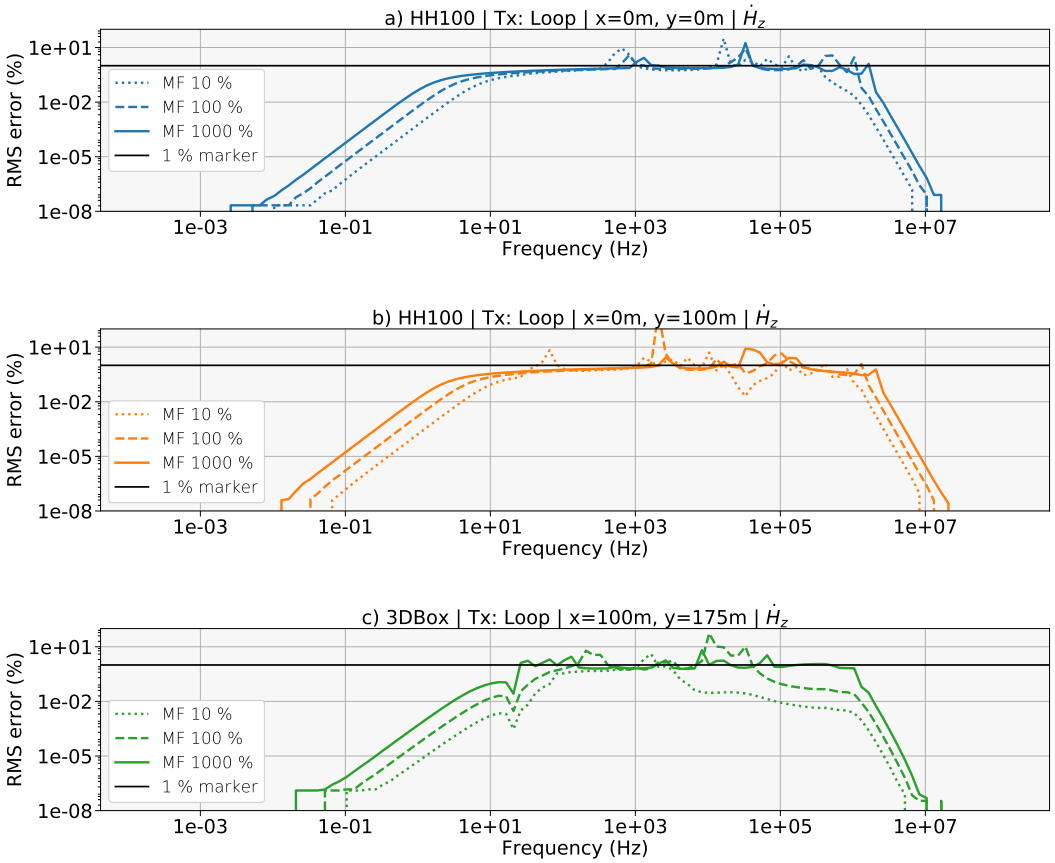

Figure 4.3.: *Single variation RMS errors of three different loop source setups. Displayed are the RMS errors between time domain transformations with each value in the frequency domain being solely varied by a modification factor (MF) of 10, 100 and 1000 % and the unmodified (original) transformation; a) corresponding to the data of the blue curve in Figure 4.2, b) corresponding to the orange curve in Figure 4.2 and c) corresponding to the green curve in Figure 4.2.*

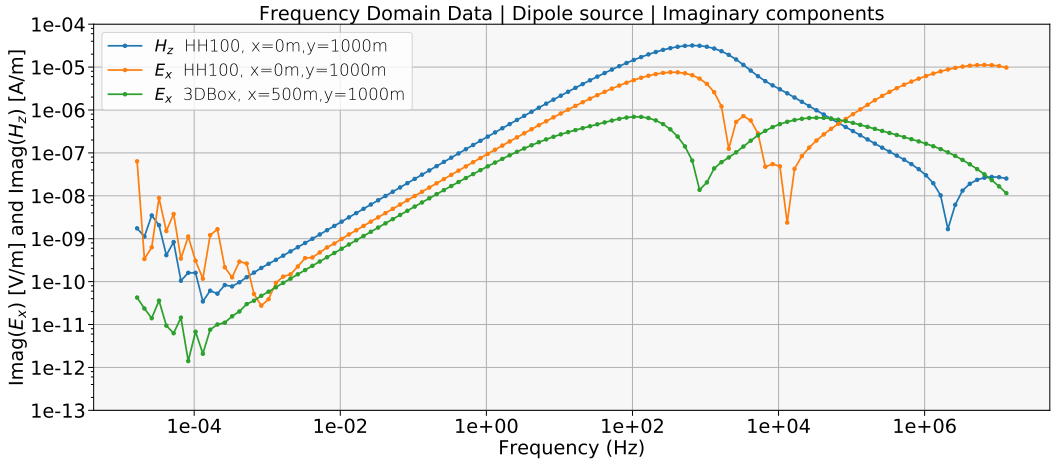

Figure 4.4.: *Frequency domain data (imaginary part of the E_x and H_z component) of three different dipole source setups. Blue: H_z of a 100 Ωm homogeneous half-space at $y = 1000$ m broadside. Orange: E_x of a 100 Ωm homogeneous half-space at $y = 1000$ m broadside. Green: Rx12 from the 3D LOTEM model B (see Figure 3.12).*

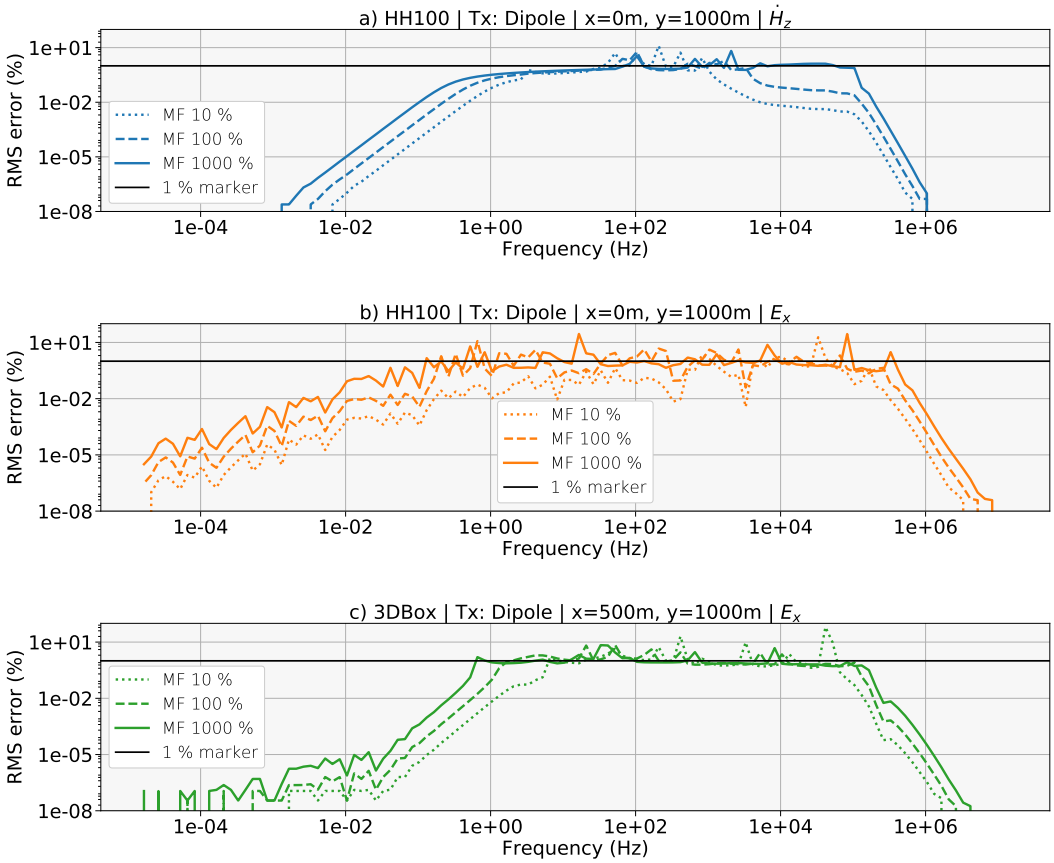

Figure 4.5.: *Single variation RMS errors of three different dipole source setups. Displayed are the RMS errors between time domain transformations with each value in the frequency domain being solely varied by a modification factor (MF) of 10, 100 and 1000 % and the unmodified (original) transformation; a) corresponding to the data of the blue curve in Figure 4.2, b) corresponding to the orange curve in Figure 4.2 and c) corresponding to the green curve in Figure 4.2.*

The first observation is that all three data series seem to be "noisy" at frequencies below 10^{-3} Hz. The blue curve (H_z of the homogeneous half-space) resembles the blue curve of Figure 4.2 (H_z in the central-loop configuration) but with lower amplitudes of approximately two orders. Additionally, it contains a sign reversal slightly above 1 MHz. The imaginary parts of the electric field components E_x (orange and green curve), the E_x component of the homogeneous half-space comprises three sign reversals (knowingly ignoring several sign reversals in the noisy region below 10^{-3} Hz) while the green curve representing the 3D model only provides one sign reversal. All three data series behave monotonously increasing between frequencies from $\sim 10^{-3}$ to 1 Hz. The data at these frequency ranges and below can possibly be calculated by extrapolation techniques without losing too much accuracy.

Like for the loop source frequency data, all values from the dipole source data series are multiplied one after another with Modification Factors of 10, 100 and 1000 % and the differences to the unmodified FHT result in terms of an RMS error are presented in Figure 4.5 a-c. The colors of figures 4.5 a-c match the colors of the corresponding curves in Figure 4.4.

The RMS errors of the modified $\dot{H}_z$ component behave similar to the loop source $\dot{H}_z$ errors and individual frequencies below 10^{-2} Hz have almost no impact on the time domain result. In contrast, both E_x results of the dipole transmitter study (Figures 4.5 b and c) show that the influence of low frequency modifications is stronger compared the H_z results. This can probably be explained by the fact that electrical field components are divided by $i\omega$ prior to the actual FHT convolution for switch-on or switch-off modes (see Chapter 2.4.2).

The results in this chapter suggest that extrapolation techniques for low frequencies and interpolation techniques for the entire spectrum can assist in obtaining FD data without the need of computing costly custEM solutions and therefore significantly save overall computation time. An extrapolation of data on the high frequency end of the spectrum seems to be unfeasible because all six investigated frequency data sets in Figures 4.2 and 4.4 exhibit an observable curvature within the highest frequency decade in the double-logarithmic presentation. A reliable prediction of these non-linear structures in terms of a linear extrapolation to higher frequencies is not possible. Here, a quadratic or cubic spline extrapolation could be useful. A more profound study of the behavior and different shapes of FD data at these high frequencies could gain better insights about possible extrapolation methods.

One task beyond the scope of this thesis is to find out what is causing the "noisy" region for the dipole source at frequencies below 10^{-3} Hz which come directly from custEM.

4.2.1. Extrapolation

In the present section, the potential of saving computation time by applying extrapolation methods to the low frequency end of the spectrum is investigated. The extrapolation of data below a given cutoff frequency is computed by applying the class *scipy.interpolate.interp1d* of the open-source scientific Python library *scipy*. Prior to the extrapolation, the data needs to be transformed to logarithmic space to allow for a linear

extrapolation. Subsequently, the data is transformed back from logarithmic space and the FHT is conducted on the extrapolated data set.

Two simple CSEM setups are presented: First, a 100 × 100 m^2 inductively coupled loop source in the central-loop configuration on top of uniform half-space of 100 Ωm. Second, a 1 km x-directed dipole source on top of uniform half-space of 100 Ωm with a broadside receiver location at y = 1000 m. Both transmitters are operating at 1 A. The investigated component is H_z in the frequency domain and $\dot{H}_z$ in the time domain. In each case, only the imaginary parts of the complex values are discussed.

The complete and "original" (non-extrapolated) frequency data series of the two mentioned setups calculated by custEM are shown as the blue curves in Figure 4.2 (loop source) and Figure 4.4 (dipole source), respectively. Both frequency series are increasing linearly up to approximately 1 kHz for the loop source and approximately 10 Hz for the dipole source. Figures 4.3a (loop source) and 4.5a (dipole source) provide information about which individual frequencies have a significant impact on the time domain result and which do not. A frequency of 1 Hz was chosen for both setups as the cutoff frequency because near 1 Hz, the presented RMS errors of individual value modifications start to drop below 1 %. In the following, the data points for frequencies below 1 Hz have been extrapolated.

Figure 4.6 shows the original and the extrapolated frequency domain data of both presented setups. The loop source data is depicted in green and the dipole source data in orange. Here, only the frequencies of interest below 1 Hz are shown, because the compared data sets are identical for higher frequencies. The relative differences in percent between the original and the extrapolated data sets are shown in the lower parts of each

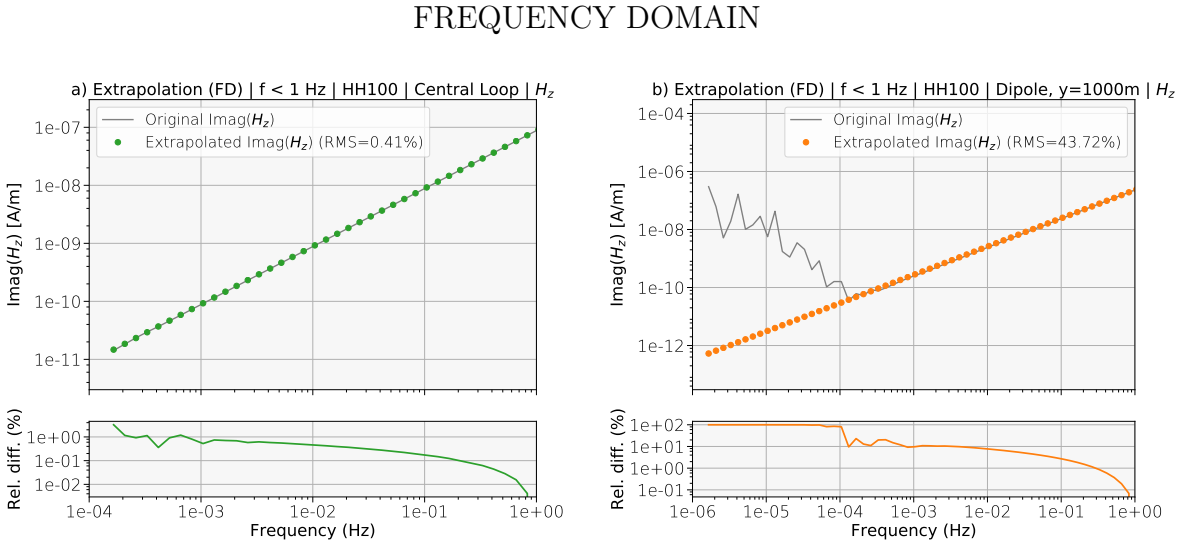

Figure 4.6.: *Original and the extrapolated frequency domain data (imaginary part of the H_z component) of a loop source and a dipole source setup on top of a homogeneous half-space of 100 Ωm. a) Central-loop transmitter with an area of 100 × 100 m^2 and an injected current of 1 A, b) x-directed dipole source with a length of 1 km and an injected current of 1 A. Only the frequency data and the relative difference in percent below a certain cutoff frequency of 1 Hz are displayed.*

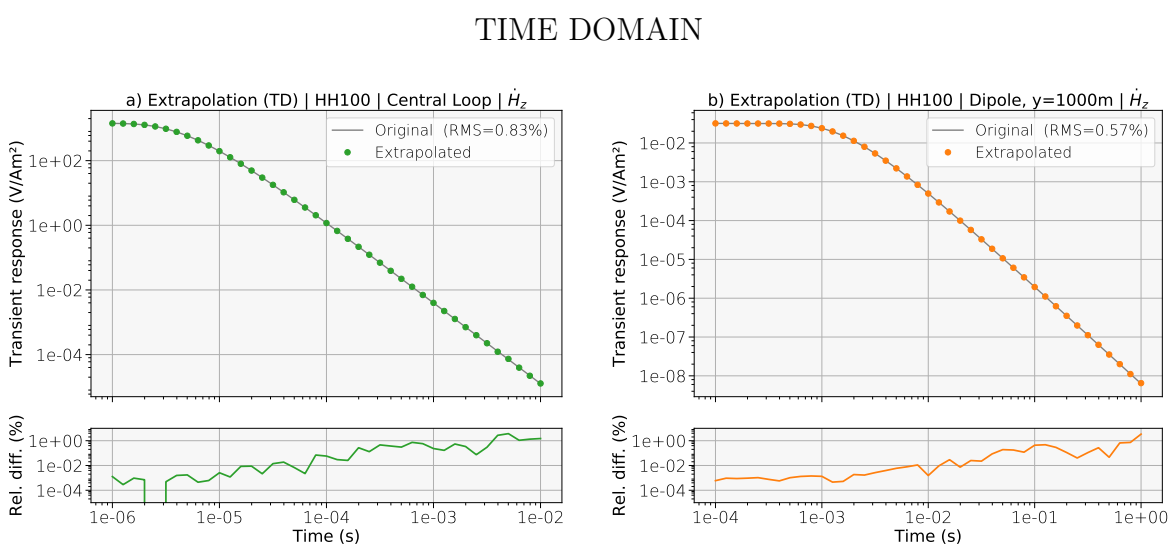

Figure 4.7.: *Time domain data ($\dot{H}_z$ component) after an FHT of the original and the extrapolated data of a loop source and a dipole source setup on top of a homogeneous half-space of 100 Ωm. a) Central-loop transmitter with an area of 100 × 100 m² and an injected current of 1 A, b) x-directed dipole source with a length of 1 km and an injected current of 1 A.*

subfigure. The loop source data in Figure 4.6a has an RMS error of 0.41 % and only the extrapolation value of the lowest frequency has a relative difference of more than 1 %. The dipole source data of Figure 4.6b again shows the original "noisy" area at the lower frequency end and in comparison to that, a smooth extrapolated data series. Accordingly, the overall RMS error is much greater with 43.72 % due to the noisy region.

Note that the starting frequency of the loop source setup is two orders greater than the dipole setup which leads to an extrapolated dipole source data set of two more decades. The reason behind is that the target time range of the dipole source forward modeling starts from two decades later in the time domain. Instead of $t_{min} = 10^{-6}$ s for the loop source modeling, the dipole source modeling starts at $t_{min} = 10^{-4}$ s which immediately influences the minimum frequency to be calculated.

In the next step, the extrapolated data is transformed into the time domain by TD-custEM's default FHT and the results are compared to the FHT transformed results of the non-extrapolated data sets. Figures 4.7a and 4.7b show these comparisons for both setups. The target time range for the loop source setup is 10^{-6} to 10^{-2} s and for the dipole source 10^{-4} to 1 s. The RMS errors of both comparisons between the original and the extrapolated data are below 1 % which is a decent result (0.83 % for the loop source data and 0.57 % for the dipole source data).

The relative difference plots of Figure 4.7 indicate that the largest deviations between the original and the extrapolated data occur at late times, which reflects the fact that the extrapolations have been made on the low frequency end of the spectrum. This means that an extrapolation of the low frequencies in the FD do have an impact in the time domain result at late times. The question now is: Which time domain result is more trustworthy, the result of the original FD data or the result of the extrapolated data?

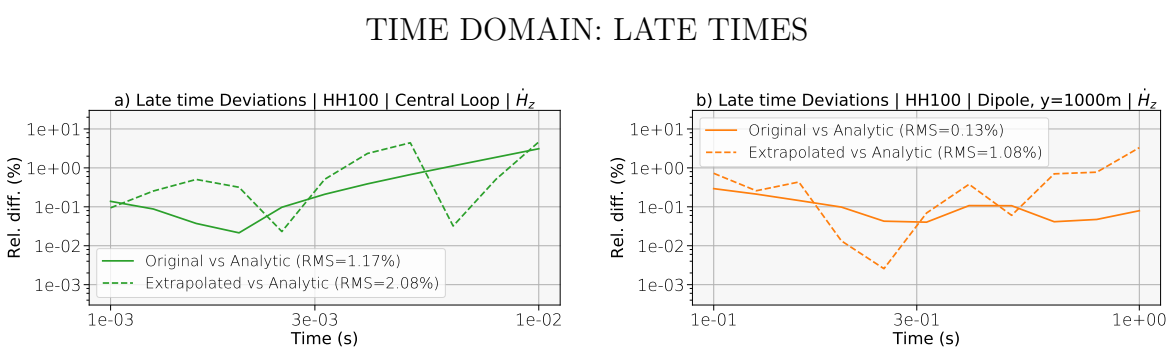

Figure 4.8.: *Comparison of late time extrapolated and original data ($\dot{H}_z$ component) with the analytic solution of a loop source and a dipole source setup on top of a homogeneous half-space of 100 Ωm. a) Central-loop transmitter with an area of 100 × 100 m^2 and an injected current of 1 A, b) x-directed dipole source with a length of 1 km and an injected current of 1 A.*

To answer this question, the analytic solutions for the given setups (Equations 3.3 for the loop source and Equation 3.4 for the dipole source) can be consulted. Figure 4.8 shows the relative differences between the original transformed data and the analytic solution as well as the relative differences between the extrapolated transformed data and the analytic solution only for the respective last decade of the loop and the dipole source CSEM setup.

The RMS errors mentioned in the legends of Figure 4.8a and 4.8b indicate that the original FD data is to be preferred. For the loop source setup the RMS error of the original data set is 1.17 % and for the extrapolated data set 2.08 %. For the dipole source setup the RMS error of the original data set is 0.13 % and for the extrapolated data set 1.08 %. But the shape of the curves in both subfigures show that the RMS errors of both extrapolated-vs-analytic curves are predominantly caused by outliers while the both original-vs-analytic curves are much smoother and their RMS errors are more conclusive.

At this stage, a conclusion about the quality of the two examined extrapolated data sets in comparison to the original data is difficult to make. But taking into account that applying an extrapolation can save significant amounts of runtime, it is worth to pursue this approach. To get quantitative numbers: for the loop source setup, 38 of 130 frequency samples have been obtained by extrapolation which would have decreased the TDcustEM total runtime by 29.2 %. For the dipole setup the total runtime would have been decreased by 44.6 %.

The present investigation of applying extrapolation techniques is of course just a simple approach to find out if there are possible ways to save computation time without losing too much accuracy. Just two CSEM cases have been studied without testing more complex subsurface models or greater transmitter/receiver offsets, etc. The larger the receiver distance and the longer the modeling times are, the more important the low frequency values of the FD data sets get. Further investigations on the shapes of the FD curves for low frequencies are necessary to improve the reliability of the extrapolated data. But if the FD data is sufficiently smooth for low (or high) frequencies, obtaining data by extrapolation has a significant potential of saving computation times.

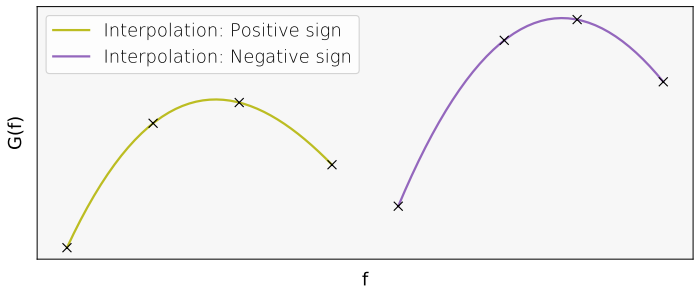

Figure 4.9: *Exemplary sketch of two cubic spline interpolations on a data set G(f) (black crosses) that provides a sign reversal.*

4.2.2. Interpolation

The second approach on speeding up computational runtime is a partly interpolation of the frequency data set. Again, the class *scipy.interpolate.interp1d* of the open-source scientific Python library *scipy* is utilized for cubic spline interpolations within this chapter. As well as for the extrapolation, the data needs to be transformed to logarithmic space prior to a spline interpolation. After the interpolation, the data is transformed back from logarithmic space and the FHT is conducted on the interpolated data set.

Data sets that contain one or more sign reversals are in the need of a special treatment, i.e. each block of the same sign needs its own spline interpolation. Figure 4.9 shows a sketch of two cubic spline interpolations for an exemplary data set G(f) that contains one sign reversal. The green curve denotes an interpolation on the first data block with a positive sign and the purple curve a second interpolation on the data with a negative sign. When trying to conduct a cubic spline interpolation on the entire data set at once, the interpolated values in the vicinity of the sign reversal would change significantly.

Prior to any interpolation of CSEM FD data, it is therefore important to know if the considered data set provides sign reversals and where they occur. Approaches on how to find this out for a given FD data set is not in the scope of this chapter. For the present case, the positions of possible sign reversals are assumed to be known. The subject of interest instead is: How many original data points can be omitted at the stage of calculation and later be obtained by interpolation without losing accuracy in the time domain solution? In the following, two frequency domain data sets are investigated using cubic spline interpolations. Note that only the imaginary part of the vertical magnetic component H_z is displayed and discussed.

Firstly, every 2nd value of the original FD data set was omitted and replaced by an interpolated value. In the following steps, the same was done with every 4th and 6th value of the original FD data set. This would infer a reduction of approximately 50, 25 and 16 % respectively of the total number of necessary frequencies. The according calculations are abbreviated E2, E4 and E6 for replacing every 2nd, 4th and 6th value in an FD data set.

To prevent inaccuracies due to an unintentional "interpolation" of the first or last frequency (which would actually be an extrapolation), all maximum and minimum frequency values have been safeguarded against the interpolation. Then, an FHT of the interpolated data sets was conducted and the time domain results were compared to the transformed results of the original data sets.

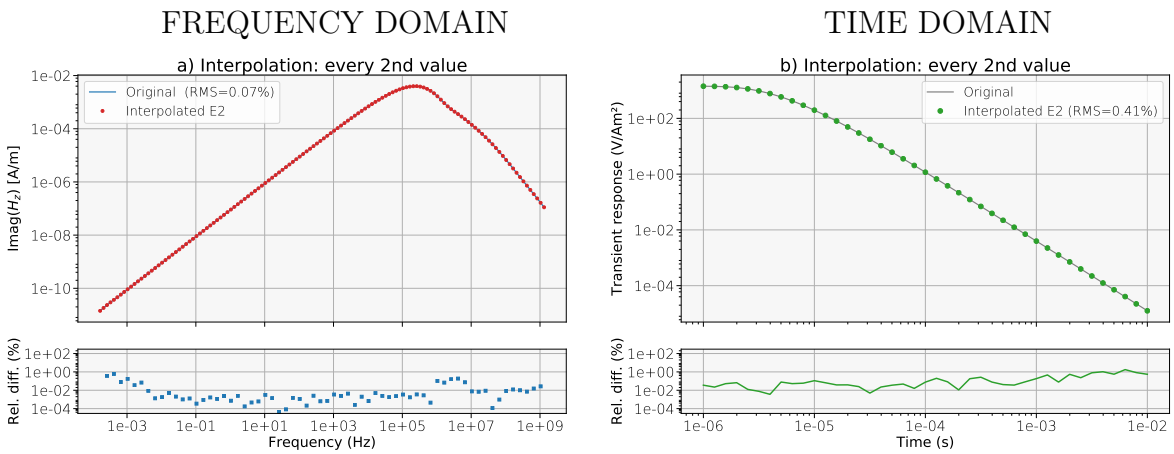

Figure 4.10.: *Comparison of interpolated (E2) and original data for a central-loop TEM setup in the a) frequency and b) time domain. In the frequency domain the imaginary part of H_z is displayed, in the time domain the impulse response $\dot{H}_z$ after conducting an FHT.*

The first investigated set corresponds to the blue curve of Figure 4.2 which belongs to a central-loop TEM setup above a 100 Ωm uniform half-space and has no sign reversal. The second investigated data set is that of a separate-loop TEM setup above the same half-space with an offset of 100 m and corresponds to the orange curve in Figure 4.2. The second data set contains a sign reversal.

Figure 4.10 shows the frequency domain (a) and the time domain (b) data of the central-loop TEM interpolation E2, in which every 2nd value of the FD data set was omitted and replaced by an interpolated value. In the frequency domain, the RMS error between the interpolated and the original version is 0.07 % which makes the blue curve of the original data set almost invisible. The largest portions of this error is coming from values at frequencies below 10^{-2} Hz and from frequencies between 10^6 and 10^7 Hz where the FD curve is slightly oscillating, as can be seen in the relative difference plot. The spline interpolation seems to work very well in the immediate vicinity of the global maximum where the relative differences are below 0.01 %.

The according time domain results of the original and interpolated FD data sets are displayed on the right-hand side of Figure 4.10 with an RMS error of 0.41 %. This result is already satisfying so the calculations of the interpolations E4 and E6 are not further investigated.

The interpolation of the second investigated data set (the separate-loop receiver TEM configuration) is more challenging due to the sign reversal in the imaginary part of the H_z component. Figure 4.11 shows the according frequency domain (left-hand side) and time domain (right-hand side) data of investigations E2, E4 and E6 (from top to bottom). The RMS values in the frequency domain are 21.50 (E2), 4.28 (E4) and 2.24 % (E6) already indicating that the E2 approach is probably not working well and that the E4 an E6 approaches might provide satisfying results. In the FD, the largest portions of the RMS come from very low frequencies, where the original data set is a little noisy, and from the vicinity of the sign reversal. Regarding the E2 approach, the cubic spline interpolation is obviously not able to reconstruct the original values to a satisfying degree.

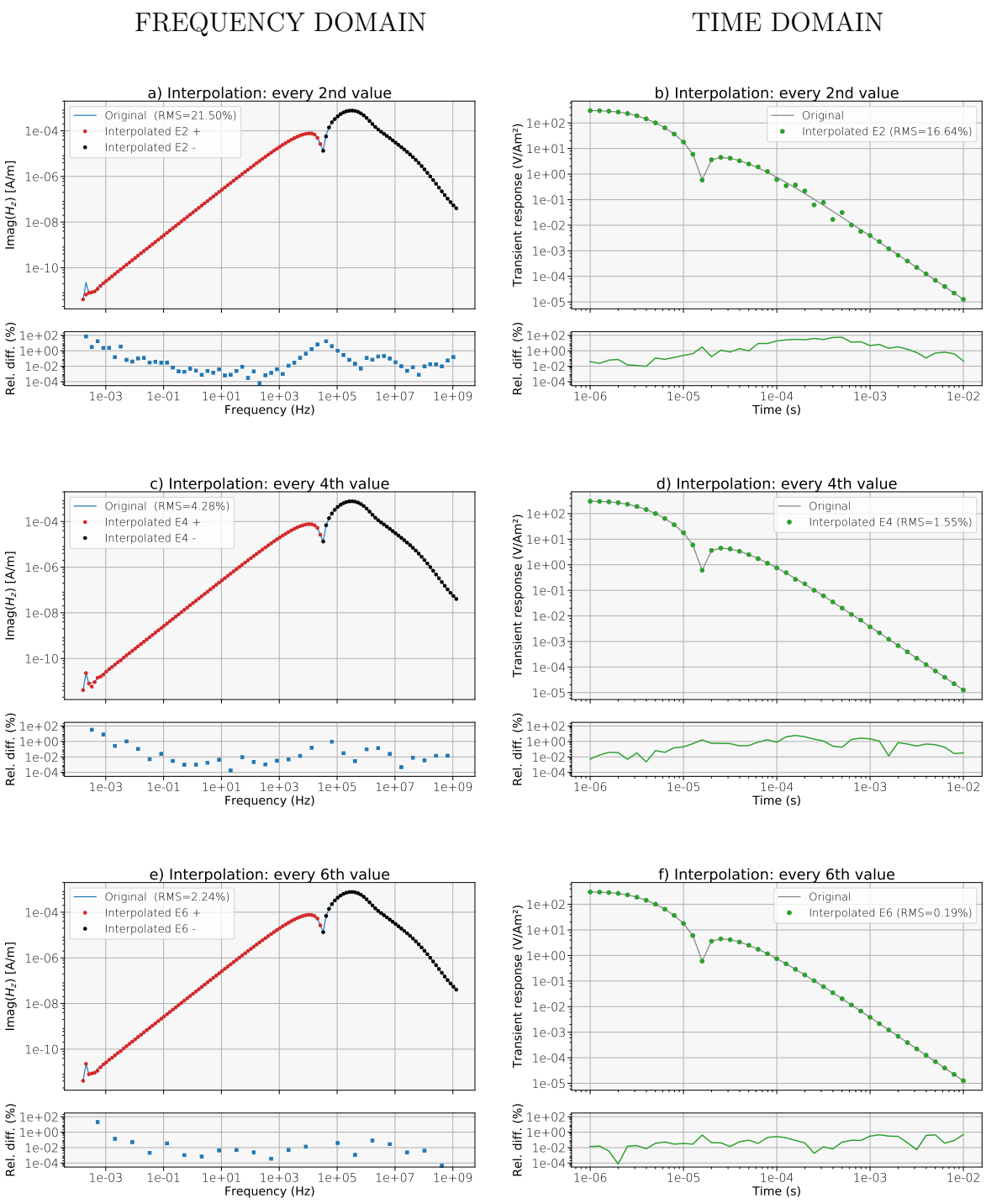

Figure 4.11.: *Comparison of interpolated (E2, E4 and E6) and original data for a separate-loop TEM setup with a receiver offset of 100 m in the frequency domain (left-hand sides) and in the time domain (right-hand sides). The sign reversal in the frequency domain is highlighted by using different colors. Red circles denote positive values, black circles denote negative values. In the frequency domain, the imaginary part of H_z is displayed, in the time domain the impulse response $\dot{H}_z$ after conducting an FHT is shown.*

Correspondingly, the transformed time domain result of the E2 approach (Figure 4.11b) has an RMS error of 16.64 % compared to the original transformed data set. The deviations between both time domain series can easily be seen at intermediate times. The E4 approach closes with a time domain RMS error of 1.55 % which can neither be seen as a satisfactory outcome nor can it be treated as failed. Instead, it should be treated as somewhere in the gray zone between both evaluations. With an RMS error of 0.19 % in the time domain, the E6 approach can finally be called successful.

Conclusively, an interpolation of every 2nd value in the frequency domain failed, a rating of the E4 approach is difficult but may be called effective and the E6 approach was successful regarding the investigated FD data set.

Applying an approach like the aforementioned on a data set with one or more sign reversals, i.e. stepping through the data and picking every n-th value for an interpolation, can be successful or it can fail in terms of an subsequent time domain transformation. Sometimes it's just a matter of luck if an important sample near a sign reversal is hit or missed by this procedure.

If the shape of the frequency domain data set and the number of enclosed sign reversals is unknown to a transformation algorithm, extrapolation and interpolation techniques might fail. A more sophisticated approach would be to firstly examine the frequency domain data with a small sampling rate and secondly, upon that, determine frequency ranges that can probably be obtained by interpolation / extrapolation purely on evaluating the coarse and approximated shape of frequency domain data. In other words: In frequency areas where the data series behaves smoothly (i.e. a straight line in the double logarithmic space), a smaller sampling rate would be sufficient. But in areas with strong curvature or a sign reversal, calculating the default 10 samples per decade is inevitable.

Therefore, it is impossible to conclude that a particular amount of frequencies per decade is generally sufficient for a CSEM 3D forward modeling using a convolutional transformation from frequency to time domain.

4.3. Precise Receiver Positioning

In CSEM field surveys, the precision and reliability of the recording instruments are fundamental to obtain trustworthy results. Another maybe not less important issue is the accuracy of the receiver location with respect to the transmitter location. What are the effects of small deviations of these transmitter/receiver distances on the recorded signals? This question is going to be answered in this chapter.

The focus will be on common TEM central and separate-loop constellations with transmitter/receiver offsets of not more than 100 m and a squared inductively coupled loop transmitter with an area of 100×100 m^2 and an injected current of 1 A. The investigated subsurface is a homogeneous half-space of 10 Ωm. With rising distances between the transmitter and the receiver, like for a typical LOTEM setup with offsets of several km, the effects of small deviations of the receiver location can be more and more neglected. Therefore, long-offset TEM modelings are not included in this study.

In the following, the transmitter locations are assumed to be fixed and the receiver locations are slighty varied in horizontal directions. Two typical TEM receiver positions

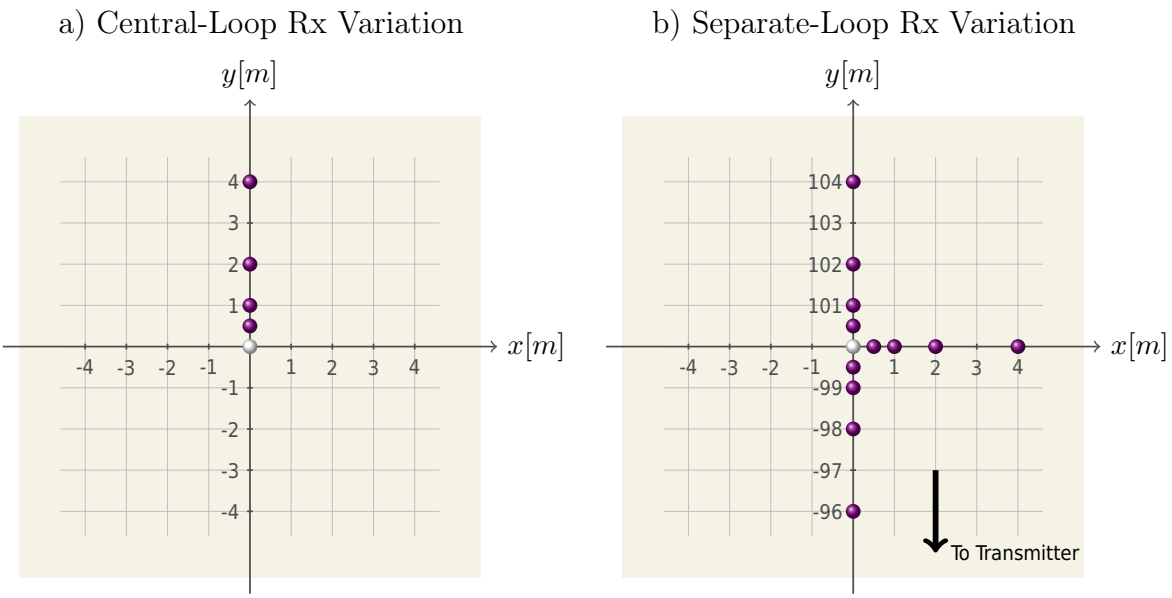

Figure 4.12.: *Variation of the receiver position for a) a central-loop setup with the receiver located in the center of the transmitter at x = 0 m, y = 0 m and b) a separate-loop setup with a receiver location of x = 0 m, y = 100 m. The white dots denote the reference positions for each setup, the purple dots denote the investigated displacements.*

are considered: A central-loop setup (x = 0 m, y = 0 m) and a separate-loop receiver (x = 0 m, y = 100 m). The investigated components are the vertical magnetic component $\dot{B}_z$ and the horizontal magnetic component which is facing into the same direction like the transmitter/receiver offset, in the present case, the y-direction ($\dot{B}_y$). The third magnetic component $\dot{B}_x$ is disregarded because it is supposed to be zero when modeling loop sources in the present setup on a uniform half-space or on 1D layered subsurfaces.

Figure 4.12 illustrates the modeled deviations from the receiver location for a) a central-loop receiver position in the center of the transmitter and b) a separate-loop receiver position with an offset of 100 m. For the central-loop setup, it is sufficient to investigate only one direction because the electromagnetic fields are expected to have a radial symmetry around the center. The modeled deviations in y-direction are y = 0.5, 1, 2, and 4 m.

At the separate-loop receiver position, the deviations are modeled in positive and negative x- and y-directions, again with offsets of 0.5, 1, 2 and 4 m in all directions. Due to symmetry reasons, the results of the positive and negative x-directed deviations are expected to be equal. Hence, the displacements into the negative x-direction are not modeled.

The results of displacing the receiver position in the central-loop setup for the components $\dot{B}_y$ and $\dot{B}_z$ are shown in Figure 4.13. The horizontal $\dot{B}_y$ component is supposed to be zero at the reference location (x = 0 m , y = 0 m) for uniform or layered half-spaces and no reference transient or relative difference can be computed. The results of Figure 4.13a indicate that for recording a horizontal magnetic component with a central-loop setup in case of an non 1D layered or homogeneous half-space, a precise receiver positioning is tremendously important. Even small displacements of 0.5 m generate horizontal magnetic

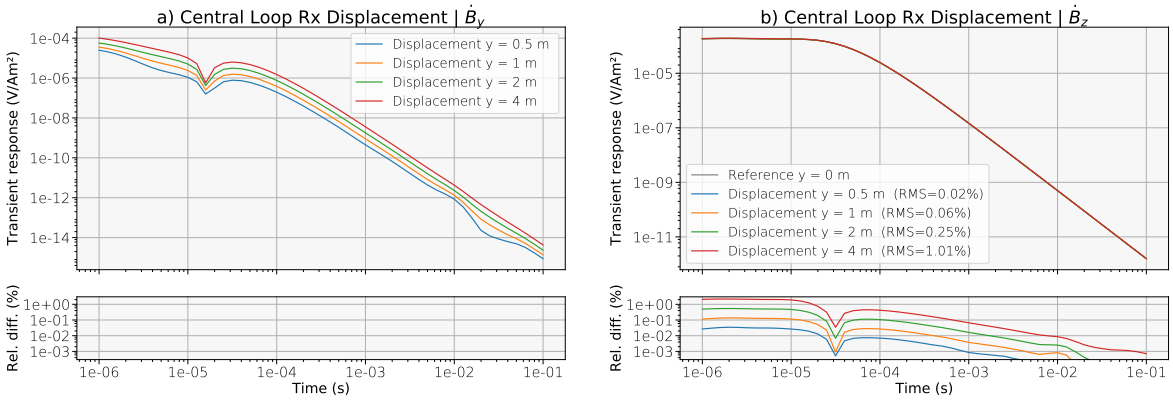

Figure 4.13.: *$\dot{B}_y$ and $\dot{B}_z$ components of small receiver displacements in the central-loop configuration. For the horizontal $\dot{B}_y$ component, no reference transient and therefore no relative differences are available.*

components that are purely based on the geometry of the magnetic dipole field and can not exclusively be contributed to resistivity contrasts in the subsurface. Moreover, the signal difference of the horizontal component between the 0.5 m dislocation and the 4 m dislocation is almost of the order of 1 magnitude. Interestingly, the time channel of the sign reversals is the same for all simulated receiver dislocations.

The importance of these consequences is illustrated by the following comparison. As presented later in Chapter 5.1.1, vertical and horizontal $\dot{B}$-field components have been measured during a field a campaign on a very open and flat area in Ethiopia. During the field work, the positions of the central-loop receivers and the corners of the 100 $\times$ 100 m^2 transmitter loop have been determined using a common handheld GPS receiver with an estimated lateral accuracy of a few meters. Figure 4.14 shows synthetic data for a 0.3 Ωm uniform half-space (which - in a rough estimate - was the case in survey area) and synthetic $\dot{B}_y$ data modeling different receiver dislocations of 0.5, 1 and 2 m together with field data of the horizontal component of one exemplary survey station.

The measured field data resembles the modeled dislocation data to a striking degree. A false assumption that the receiver is perfectly positioned might therefore lead to misinterpretations of the data because it is uncertain what causes the recorded signals. This example emphasizes the importance of precise receiver positioning when horizontal components are being measured. In the displayed case, the shape of the recorded signal is probably due to a receiver dislocation.

In comparison to Figure 4.13a, the sign reversal occurs several time channels later which is attributed to the lower background resistivity of 0.3 Ωm in the synthetic results of Figure 4.14.

Figure 4.13b shows the corresponding displacement results for the $\dot{B}_z$ component. Here, a precise positioning of the receiver seems less strict than for the horizontal component. A displacement of 0.5 m yields a transient with an RMS error of 0.02 % with respect to the reference station in the exact center of the transmitter loop. Even a displacement of 1 or 2 m can be neglected with RMS errors of 0.06 and 0.25 %. A receiver displacement

Direction	Rx Coordinate [m]	$\dot{B}_y$ [%]	$\dot{B}_z$ [%]
+y	100.5	6.71	5.26
	101	13.2	10.5
	102	25.7	20.7
	104	48.3	40.3
-y	99.5	6.90	5.32
	99	14.0	10.7
	98	28.8	21.7
	96	60.8	44.3
+x	0.5	0.02	0.01
	1	0.05	0.05
	2	0.15	0.19
	4	0.53	0.78

Table 4.1.: *Maximum relative differences ($\dot{B}_y$ and $\dot{B}_z$) in percent for selected receiver location displacements of a separate-loop TEM setup (see Figure 4.12b). The reference receiver location is $x = 0$ m and $y = 100$ m. Due to symmetry aspects, the negative x direction has been omitted.*

of 4 m yields an RMS of 1.01 % which means that a significant deviation from the desired signal can be expected.

The corresponding figures of the separate-loop calculations are not displayed because there are rarely any visible differences between the computed displacement transients except near the sign reversals. The plots of the relative differences with respect to the transient of the reference location are only shifted (similar to the relative differences in Figure 4.13b) and are also omitted.

Instead, the maximum relative differences in percent for the $\dot{B}_y$ and $\dot{B}_z$ component between each calculated displacement transient and the reference transient are given in Table 4.1. For the calculation of these maximum differences, the values next to a sign reversal have been ignored. Due to the sign reversals in all of the separate-loop transients, no RMS errors are considered as a tool of evaluation.

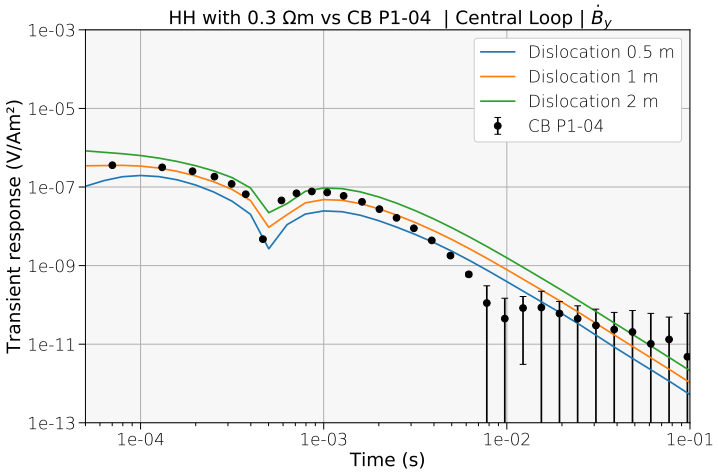

Figure 4.14: *Comparison of synthetic $\dot{B}_y$ data of a homogeneous half-space of 0.3 Ωm modeling different receiver dislocations of 0.5, 1 and 2 m and exemplary $\dot{B}_y$ field data.*

Firstly, the results in Table 4.1 show a huge discrepancy between displacing a separate-loop receiver into the direction of the transmitter/receiver offset (y-direction) and displacing it into the perpendicular direction (x-direction). That difference is of approximately two orders. Secondly, the results indicate that a displacement in the positive y direction (i.e. away from the transmitter) yields a smaller misfit than a displacement into the negative y-direction (i.e. to the transmitter). A final result from Table 4.1 is that receivers of the vertical magnetic component $\dot{B}_z$ are more sensitive to x-directed dislocations and less sensitive to y-directed dislocations than the horizontal $\dot{B}_y$ component.

4.4. About Domain Sizes

Other factors of the solution's accuracy are the size of the computational domain and the imposed boundary conditions. Chosing the domain to be too small can generate erroneous data at late times. Choosing the mesh to be too coarse around the transmitter and the receiver results in early time inaccuracies. Moreover, the larger the mesh is, the longer the computation runtimes will be. Creating a mesh is always a tradeoff between solution accuracy and runtime.

During the calculations for Chapter 3 and 4, two things turned out regarding the discretization of transmitters and receivers. For transmitters, an average segmentation length of 10 m per segment is sufficient (i.e. subdivide a 1 km dipole source in 100 segments with 10 m per segment). For the receiver discretization lengths, values of 1 to 10 m for LOTEM setups (dipole sources) and 0.1 to 1 m for TEM (loop sources) on average seemed to be appropriate. Receiver discretization lengths define the minimum edge length of tetrahedra adjacent to the receiver location.

As mentioned in Chapter 3.1, custEM provides a technique to extent the primary computation domain by a so-called *bigger world*. This technique simply wraps a secondary, much coarser cube around the primary domain increasing the size of the computation domain by for example the factor 10 or 100 without adding significantly more cells to the mesh. This boundary technique is also known as a *tetrahedron boundary*. The cell sizes of this extension are of course much larger than the cell sizes of the primary mesh. Typical primary mesh dimensions[12] for TEM setups are a few kilometers, for LOTEM setups the primary mesh can have a few tens of kilometers. For example, wrapping a secondary mesh with a factor of 100 around a primary mesh with a dimension of 10 km would yield total domain extents of 1000 km $\times$ 1000 km $\times$ 1000 km = 10^9 km^3. In the following, wrapping a secondary mesh around the primary is defined as multiplying the primary mesh extents with an Extension Factor (EF). An EF of 1 denotes no extension.

Table 4.2 shows the total number of cells used for the conducted calculations in thousands. The 1 km sized primary mesh without a bigger world extension is made of $\sim$ 17 k tetrahedra. Applying an EF of 10 to this primary mesh increases the total mesh size to 10 km $\times$ 10 km $\times$ 10 km but the total number of cells only to $\sim$ 24 k. An extension by the factor 100 yields only $\sim$ 25 k cells.

[12] A dimension of 1 km means that the entire simulation box has extents of 1000 m $\times$ 1000 m $\times$ 1000 m = 1 km^3.

EF	1 km Dim.	2 km Dim.	5 km Dim.	10 km Dim.
1 (no extension)	17 k	18 k	21 k	28 k
10	24 k	25 k	26 k	37 k
100	25 k	27 k	28 k	40 k

Table 4.2.: *Total number of cells per mesh for differently sized primary uniform half-space meshes and extension factors.*

In this section, the solution accuracy of different half-space mesh sizes and secondary mesh extensions are compared against an analytic solution (Equation 3.3). The scenario is a central-loop TEM configuration on top of a 100 Ωm uniform half-space and the transmitter is a 100 × 100 m^2 loop source with 1 A. The investigated component is $\dot{B}_z$. The modeled time range is from 10^{-6} to 10^{-1} s which is a very late time regarding the chosen TEM setup. But to investigate possible boundary effects, this late time seems to be reasonable. The performance of *Zero-Dirichlet* (ZD) boundary conditions are investigated as well as the performance of the code when omitting the boundary conditions entirely. The following results and implications are also valid for dipole source transmitters in LOTEM setups by simply multiplying the dimensions of the primary mesh by a factor of 10.

Figure 4.15 shows the relative differences between the modeled transient data and the according analytic solution. Four different primary mesh dimensions from 1, 2, 5 and 10 km have been calculated with EF of 1, 10 and 100. Additional to the relative difference plots, each subfigure shows the according RMS error between the modeled transient and the analytic solution in each subfigure's legend. The left-hand side of Figure 4.15 shows the results without imposing any boundary condition and on the right-hand side the results for imposing ZD boundary conditions are shown.

There seems to be no significant difference between the ZD boundary conditions and omitting the boundary conditions entirely. Actually, when comparing all RMS errors of the left and the right side of Figure 4.15, the results of imposing ZD boundary conditions are slighty higher. EFs of 1 yield inaccurate results at late times in all cases. This implies that a mesh extension by the factor 10 is always recommended. Although the times after 10^{-2} s are usually too late and signals are too weak for the given TEM setup. A primary mesh size of 2 km × 2 km × 2 km with an EF of 10 seems to be sufficient for the given central-loop setup. An EF of 100 is only useful for the smallest primary mesh dimension of 1 km and does not improve the solution accuracy in the other cases.

The persistent relative differences of more than 1 % at early times before 10^{-5} s in all the results of Figure 4.15 are probably related to the coarseness of the mesh around the transmitter. The transmitter segment length was set to 10 m. However, these early times and the corresponding shallow penetration depths are usually not of interest when conducting TEM field surveys with a 100 × 100 m^2 transmitter loop.

4.5. About Resistivity Contrasts

Within 3D CSEM, modeling huge resistivity contrasts in the subsurface can be numerically challenging. To test the capabilities of TDcustEM regarding the range of resitivity

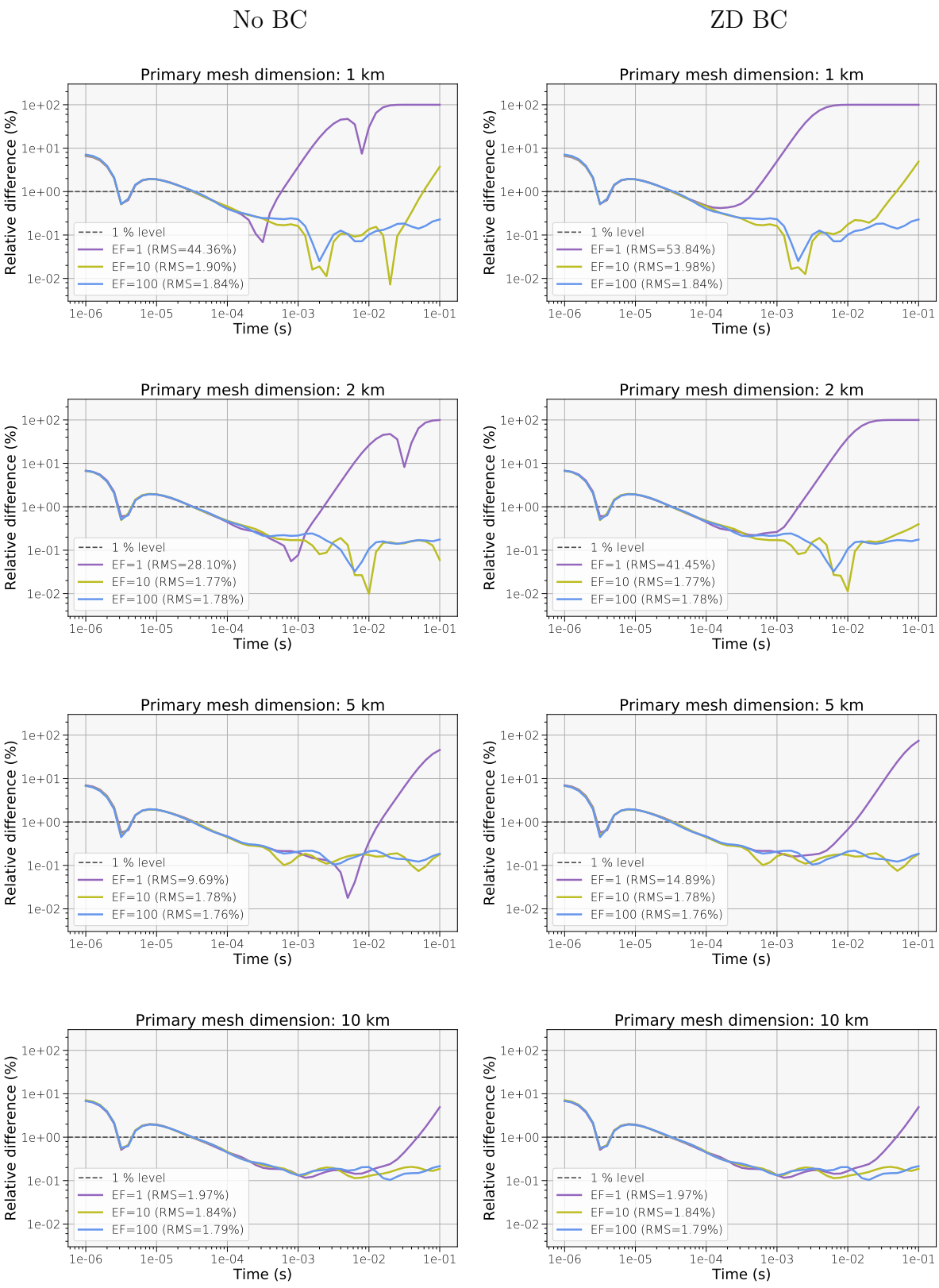

Figure 4.15.: *Relative differences in percent between $\dot{B}_z$ TEM transients of differently sized primary meshes / Extension Factors and the according analytic solution. Primary domain dimensions are from top to bottom: 1, 2, 5 and 10 km. The Extension Factors are 1, 10 and 100 in each subfigure. On the left-hand side, the forward calculations without boundary conditions are shown and on the right-hand side, the results for imposing Zero-Dirichlet boundary conditions are displayed. The black dashed lines denote the 1 % relative difference threshold.*

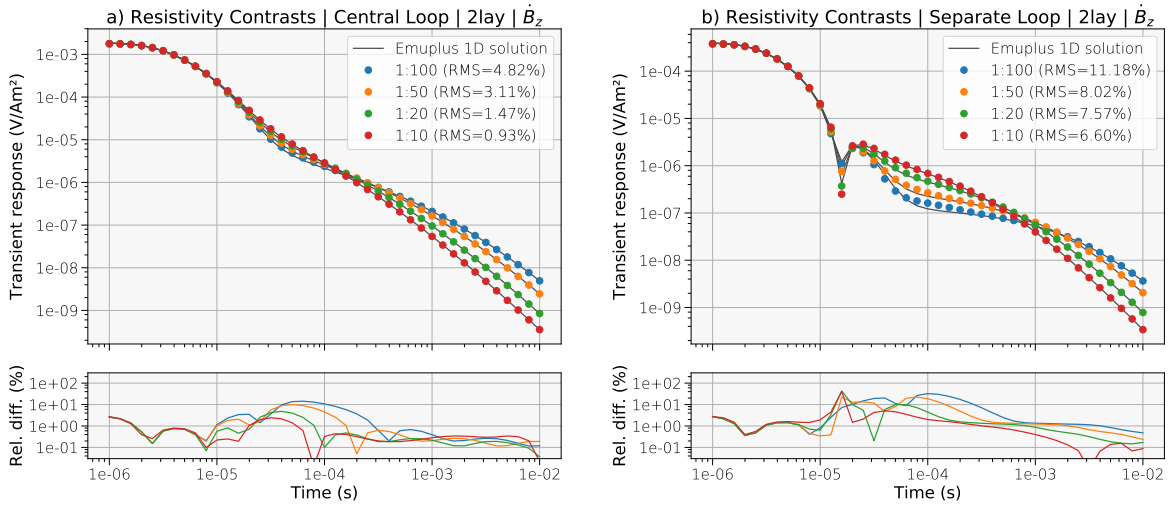

Figure 4.16.: *Transient data and relative differences between TDcustEM and EMUPLUS for modeling resistivity contrasts from 1:100 to 1:10. The transmitter is a 100 × 100 m² loop source and the receivers are positioned in a central-loop location (a) and a separate-loop location (b) with an offset of 100 m.*

contrasts that the code can handle, a synthetic study simulating a central- and separate-loop TEM setup has been performed. The transmitter again was a 100 × 100 m² loop source with 1 A and two $\dot{B}_z$ receiver position are investigated. One in the center of the transmitter loop and one in the separate-loop configuration with an offset of 100 m. The subsurface was a 2-layer case where the top layer had a resistivity of 100 Ωm and the resistivity of the second layer had variable resistivities of 10, 5, 2 and 1 Ωm. The modeled ratios are therefore 1:10, 1:20, 1:50 and 1:100. The thickness of the first layer was fixed at 50 m.

The TDcustEM results are compared to the semi-analytic results computed by EMUPLUS. Figure 4.16 shows the transients of the modeled resistivity contrasts for both receiver locations. The TDcustEM transients are marked as colored dots and the corresponding EMUPLUS data as black solid lines. Underneath the transients, the relative difference between both results are shown in percent. The RMS errors are given in the legends of Figure 4.16.

Regarding the central-loop simulation (Figure 4.16a), RMS errors < 2 % indicate that resistivity contrasts of 1:20 and below are easily handeled by TDcustEM. A contrast of 1:50 yields an RMS error of ~ 3 % which is not satisfying, yet tolerable. However a contrast of 1:100 yields an RMS error of > 4 % which is a rather poor outcome. For the data points at intermediate times from 30 to 100 μs, the relative difference between TDcustEM and EMUPLUS is more than 10 %.

For the separate-loop calculations (Figure 4.16b), the RMS errors are even greater than for the central-loop calculations which can be explained for the most parts by the geometrical sign reversal. But beside the sign reversal, the relative differences of the contrasts 1:50 and 1:100 are again > 10 % for some data points at intermediate times. One reason behind these relatively large differences might be the fact that due to the chosen geometry of the subsurface and the transmitter/receiver offset in the separate-loop setup, the effects of

the very conductive second layer appear almost immediately after the sign reversal in the transients.

Obviously, there is need of improvement regarding the calculations of huge resistivity contrasts. In general, the mesh resolution should be high in conductive regions and can be lower in resistive regions. Maybe a higher mesh resolution should be provided to the boundaries of large resistivity contrasts.

.

CHAPTER 5

Application - CSEM Field Data from Ethiopia

The practical part of the present thesis consisted of two field surveys in Eastern Africa where several sedimentary basins have been investigated with two-dimensional transient electromagnetics. Following this introduction, the survey details, the survey areas and 1D inversion results are shown and discussed. Subsequently, the recorded data was subject to laterally and spatially constrained inversion using the software AarhusInv from the Hydrogeophysics Group of Aarhus, Denmark. After that, to assess the detectability of possible bedrock layers underneath the investigated basins, an extensive 3D CSEM forward modeling study of synthetic data using TDcustEM has been performed.

5.1. Survey Areas and 1D Inversion Results

In the framework of the Collaborative Research Centre 806 (CRC 806) *Our way to Europe*[13], two multidimensional CSEM surveys have been conducted on sedimentary basins in southern and central Ethiopia. Combining geoscientific and archeological methods, the CRC 806 is designed to reconstruct the passageway of Modern Man from eastern Africa to central Europe ("Out of africa" theory) covering a period of the last 190,000 years.

Climate and environment have been the driving factors for the migration times and routes of Homo sapiens. Hence, the reconstruction of the paleoclimate is a crucial factor in understanding prehistoric migration and settlements in the arid regions of North-East Africa.

The role of geophysics within this project is to assist with the identification and definition of possible paleoenvironmental archives such as sedimentary deposits. Exploring the basement morphology and the sedimentary structure is a prerequisite to derive suitable borehole locations for core drillings. The geological and geochemical analysis of these sample cores allows for a subsequent reconstruction of the paleoclimate. The East African Rift Valley (EARV) and the Ethiopian Highlands are suitable places that provide several

[13]http://www.sfb806.uni-koeln.de/

Figure 5.1.: *Map of Ethiopia and the three survey areas Chew Bahir, Bisare River and the Dendi Lakes located inside or close by the main trench of the East African Rift Valley (Modified version of http://commons.wikimedia.org/wiki/File:Ethiopia.png. License: public domain).*

of these sedimentary basins. The obtained geophysical data is analysed by conventional 1D as well as laterally and spatially constrained inversion techniques.

The first survey took place in November and December, 2014, with the destination *Chew Bahir*, a saline mudflat in southern Ethiopia near the border to Kenya. In February and March, 2015, the second survey was conducted with two target locations: *Bisare River* and the *Dendi Lakes* in southern and central Ethiopia. While Chew Bahir is a purely tectonically-formed basin, Bisare River and the Dendi Lakes are volcanically-formed basins.

Figure 5.1 shows a map of Ethiopia and the three survey locations inside or near to the main trench of the EARV. On each location, two-dimensional transient electromagnetic measurements have been conducted. All TEM measurements have been performed in the central loop configuration using a *Zonge International* system consisting of an NT-20 transmitter unit and an GDP-32II receiver unit. If applicable, TEM/3 induction coils from Zonge served as receiver loops for measuring the time derivative of the vertical and one horizontal component of the magnetic field. Apart from that, single loop wires served as receivers.

The Zonge NT-20 transmitter operates in two different modes that address different investigation depths. The NanoTEM (NT) mode is working with relatively short acquisition times and shallow investigation depths. In contrast, the ZeroTEM (ZT) mode uses higher induced currents, longer acquisition times and facilitates greater investigation depths. The TEM/3 induction coils have a ferrite core, an own pre-amplifier and effective receiver areas of 10,000 m^2. They are only applicable for ZT measurements due to a quite long antenna delay of 15 μs (*Zonge*, 2002).

In a first step, the recorded $\dot{B}_z$ data were inverted individually by means of 1D interpretations, utilizing different inversion techniques such as Occam and Marquardt. The 1D inversions were conducted using the Software EMUPLUS. Additionally, equivalent models are shown together with the inversion results. When using error weighted data, several models can explain the data likewise within the error bounds. *Scholl* (2005) implemented an approach into EMUPLUS that creates equivalent models using a Monte-Carlo concept by perturbating the model parameters randomly.

For details on data processing steps and the theoretical background of the applied inversion techniques like Occam or Marquardt, see *Yogeshwar* (2014). Along with the 1D inversion results, $\rho_{a,lt}$ transformations are shown which qualitatively represent the distribution of the apparent resistivity at late times. The transformation after *Spies and Frischknecht* (1991) reads:

$$\rho_{a,lt} = \frac{I^{2/3}\ \mu\ a^{4/3}}{20^{2/3}\ \pi^{1/3}\ t^{5/3}} \cdot \left(-\partial_t H_z^{lt}\right)^{-2/3} \tag{5.1}$$

with a = the equal circular transmitter radius for a rectangular loop transmitter, I = the injected current and $\mu = \mu_0$ (the magnetic permeability of free space). According to *Spies* (1989), the maximum depth of investigation (doi) for a central loop TEM setup is

$$\delta_{doi} \approx 0.55 \left(\frac{I A_{Tx}}{\sigma\ \eta_\nu}\right)^{1/5} \tag{5.2}$$

with the transmitter area A_{Tx}, the mean subsurface conductivity σ and the ambient noise level η_ν. Typical noise levels after stacking are 0.5 nV/m^2 (*Spies*, 1989). The diffusion depth, i.e. the depth when a particular layer is detectable for a fixed time t reads: (*Ward and Hohmann*, 1991):

$$\delta_{TD} = \sqrt{\frac{2\ t}{\mu\ \sigma}} \tag{5.3}$$

An alternative approach to estimate an effective maximum exploration depth for TEM soundings depending on (5.3) is given by *Meju* (1995):

$$\delta_{eff} = \frac{\delta_{TD}}{2.3} \tag{5.4}$$

This equation approximates the maximum depth of investigation much more conservative than *Spies* (1989).

Secondly, the recorded TEM data sets were inverted using the software *AarhusInv*[14] from the Hydrogeophysics Group of the University of Aarhus, Denmark. Here, all data and models are inverted as one system, producing layered solutions with laterally smooth transitions. The models are regularized through lateral constraints that tie interface depths or thicknesses and resistivities of adjacent layers (*Auken and Christiansen*, 2004).

When the data is recorded along a single profile, the method is referred to as Laterally Constrained Inversion (LCI). When deploying a 2D surface grid of measurements, the method is called Spatially Constrained Inversion, or SCI (*Viezzoli et al.*, 2008). According

[14]Formerly known and distributed under the name *em1dinv*.

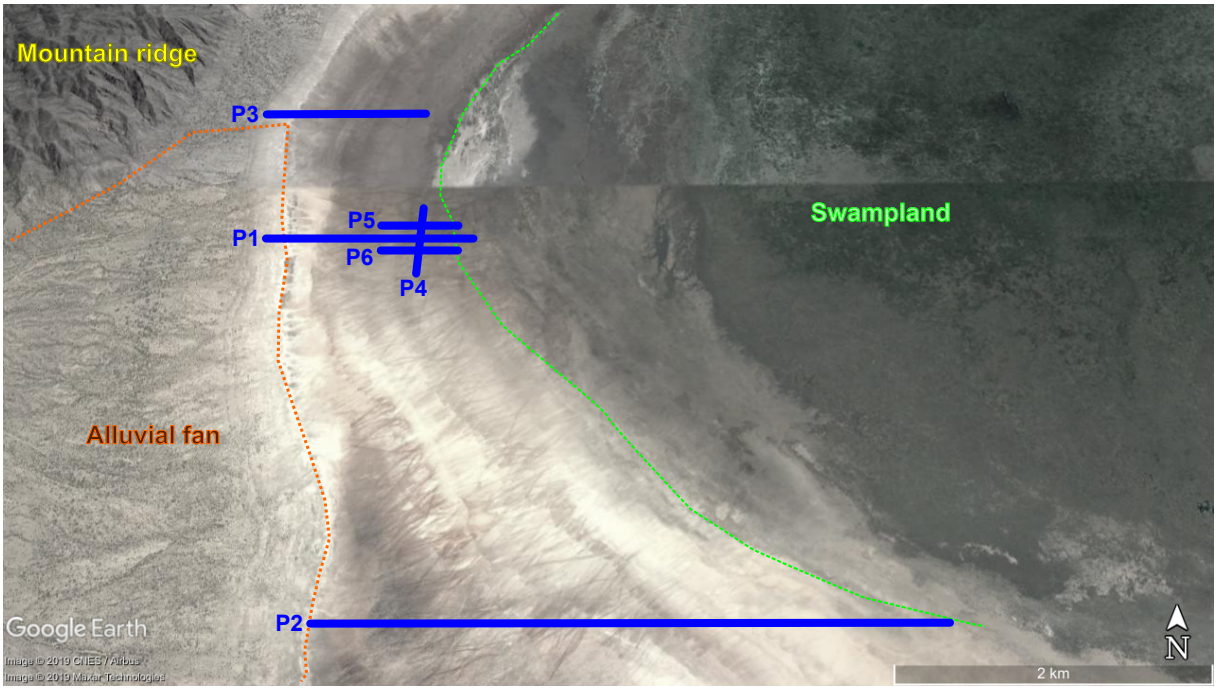

Figure 5.2.: *Survey area and location of TEM profiles at the western border of Chew Bahir. Profiles P2 and P3 have only been measured in parts (background image: Google Earth).*

to the Hydrogeophysics Group of Aarhus, these inversion techniques are well suited for data recorded within sedimentary environments.

The AarhusInv software writes out a summary file containing a DOI range for every station which is calculated from the model parameter sensitivities (*Christiansen and Auken*, 2012). The major limit of these DOI ranges is plotted together with the LCI/SCI results when constrained inversion results are shown in this chapter.

5.1.1. Chew Bahir

The Chew Bahir (amharic: "salty lake", E 36.84, N 4.684) basin is a 30 $\times$ 70 km^2 saline mudflat that only episodically fills to a shallow lake during rainy season in spring and summer. Chew Bahir is located in the Broadly Rifted Zone between the mountains of the Hammar Range in the west and the Teltele Plateau in the east. According to airborne gravity and seismic reflection data, the thickness of its sedimentary deposits is assumed to be of up to 5 km (*Foerster et al.*, 2012) in the center. Therefore, the basin potentially provides sedimentary archives that extend far beyond the Quaternary.

Along 6 profiles, a total of 60 two-dimensional TEM soundings were taken. Five profiles were east-west oriented, only profile P4 was north-south oriented, see Figure 5.2. The station distance was 100 m for all profiles. The transmitter consisted of a 100 x 100 m^2 loop and two Zonge TEM/3 coils served as receivers for the vertical and for one horizontal component of the time derivative of the secondary magnetic field. The TEM devices were only operated in ZeroTEM mode to allow for an investigation as deep as possible.

For every station, the horizontal component was measured in east-west direction, perpendicular to the nearby western mountain ridges of the Hammar Range. This alignment

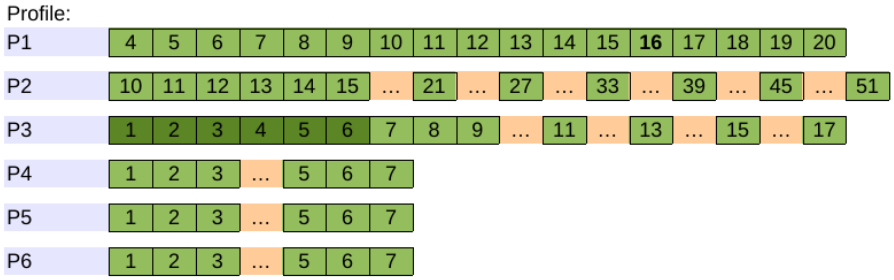

Figure 5.3.: *Listing of stations per profile of the Chew Bahir survey. Only the mentioned stations with a green background have been measured. Stations 1 to 6 of profile P3 were operated with a transmitter size of 50 × 50 m², instead of the default 100 × 100 m². At station P1-16, two deep ICDP-HSPDP drillings have been conducted.*

was chosen to study possible 2D effects of either the mountains and their underlying crystalline bedrock or alluvial fans intruding from the basins western boundaries.

Shortly before the TEM measurements at Chew Bahir, two deep drillings were conducted in the framework of the ICDP-HSPDP (International Continental scientific Drilling Program - Hominin Sites and Paleolakes Drilling Project) in collaboration with colleagues of the CRC 806. The drillings reached depths of approximately 280 m each and the cores bases could be dated back 620,000 years (*Prof. Dr. Frank Schäbitz*, personal communication, Aug. 21st, 2019). The junction of profiles P1 and P4, TEM sounding P1-16, is located at the position of these drillings.

Figure 5.3 shows an overview of the recorded stations per profile. Only the actually mentioned stations (with green backgrounds) have been recorded. The numbering starts either in the west or in the north (only profile P4). Profiles P1, P4, P5 and P6 have been measured station-to-station, i.e. the center positions of the 100 × 100 m² transmitter loops are in a distance of 100 m.

Profiles P2 and P3 have been measured only in parts. The six western-most stations of P2 have been measured station-to-station, after that, only every 6th station was recorded. Due to increasing vegetation and rough terrain, the western-most six stations of profile P3 have been operated using a smaller transmitter size of 50 × 50 m². Stations 7, 8 and 9 have been operated regularly and east of that only every second station was recorded.

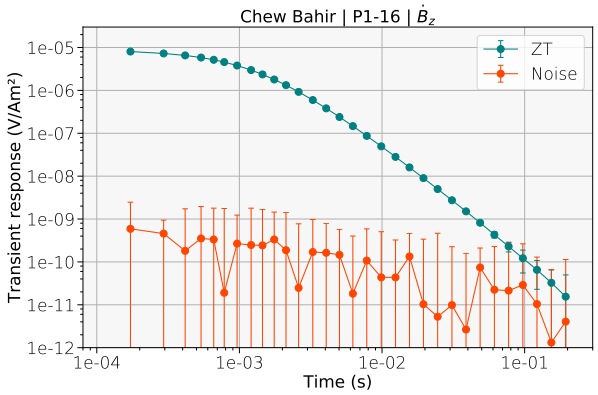

Figure 5.4: *ZeroTEM transient ($\dot{B}_z$) and noise floor of station P1-16 at Chew Bahir.*

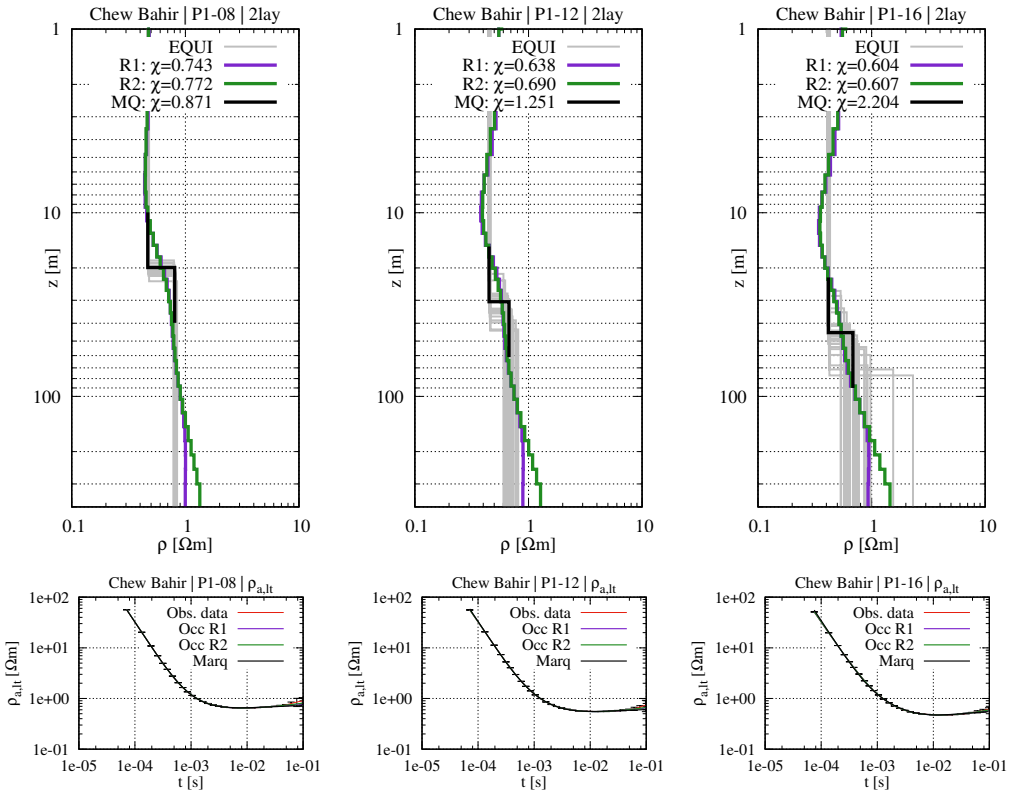

Figure 5.5.: *1D inversion results and $\rho_{a,lt}$ conversions (data and fittings) for selected soundings 08, 12 and 16 of profile P1 at Chew Bahir.*

On profiles P4, P5 and P6, the fourth stations were omitted because they coincided with measurements already taken on other profiles. Profile P5 was positioned 100 m north of profile P1 and profile P6 100 m south of P1. Missing station numbers at the start of profile P1 and P2 in Figure 5.3 indicate that these stations were planned in advance but their realization was skipped due to vegetation or rough terrain.

Exemplarily for the collected $\dot{B}_z$ data set at Chew Bahir, Figure 5.4 shows a ZT transient of station P1-16 along with a noise measurement of the same location. The noise floor was quite low with values around 10^{-10} V/Am^2 and even lower for late times.

1D inversion results and $\rho_{a,lt}$ conversions of selected stations 08, 12 and 16 of profile P1 are shown in Figure 5.5. In purple and green, the Occam R1 and Occam R2 inversion results are shown, the black line marks the results of the Marquardt inversions. These are visually accompanied in gray by results of equivalent models. Both, the Occam and the Marquardt inversion results indicate a very conductive subsurface with resistivities below 1 Ωm for the most part. The starting model for the Marquardt inversions was a 2-layer model with a 20 m thick first layer. The resistivity was 1 Ωm for both layers.

The resistivities are increasing only slightly with greater depths, as can be seen from the Occam results and from the $\rho_{a,lt}$ conversions of Figure 5.5. The 1D inversion results of the

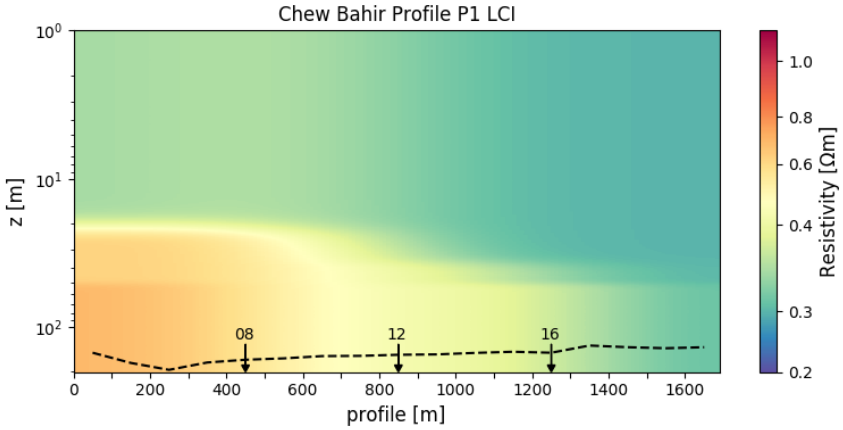

Figure 5.6.: *Interpolated and smoothed LCI 2D result of Chew Bahir profile P1. The position of stations 08, 12 and 16 shown in Figure 5.5 are marked with black arrows for comparison. The dashed line denotes the DOI provided by the AarhusInv software.*

remaining stations of profile P1 as well as the results of the other profiles at Chew Bahir look similar. Plots of all 1D inversion results from Chew Bahir are shown in Appendix A.

The maximum depth of investigation after *Spies* (1989), Equation 5.2, yields unrealistic values of $\sim$ 550 m using typical values of the Chew Bahir survey of I = 10 A, A_{Tx} = 10,000 m^2, σ = 1 S/m and η_ν = 0.1 nV/m^2. The diffusion depth (5.3) for a very late time of t = 0.1 s and σ = 1 S/m yields $\delta_{TD} \sim$ 400 m. The effective depth of investigation after *Meju* (1995), Equation 5.4, yields a depth of $\sim$ 170 m. The latter seems to be the most trustworthy estimation taking the low resistivity of the subsurface into account. This value corresponds approximately to the DOI provided by the LCI result, which is printed as a dashed line in Figure 5.6.

Figure 5.6 shows an interpolated and smoothed, two-dimensional LCI result of profile P1. The starting models for the constrained inversion were the same that were used for the 1D Marquardt inversions. The linear 2D interpolation was computed using the *interp2d* routine of *scipy* and for the smoothing, a 2D Gaussian filter was applied. The total profile length is 1.7 km.

Only slight resistivity contrasts can be seen at depths of 20 to 40 m where the resistivity is increasing from 0.3 to 0.6 Ωm. This contrast is dipping from west to east but fades out east of profile meter 1200. To simplify a comparison with Figure 5.5 the locations of stations 08, 12 and 16 have been marked with black arrows.

Eventually, the recorded data of all profiles from Lake Chew Bahir turned out to be barely challenging from a scientific point of view. The electrical resistivity of the Earth underneath lake Chew Bahir lacks conductivity contrasts for the uppermost $\sim$ 200 m of sediments and electrical resistivities are very low, mainly between 0.3 and 1 Ωm. These low resistivities, which probably originate from highly saline contents in the subsurface, impede great investigation depths.

The first conclusion is that even at the western-most stations of the investigated profiles that are closest to the mountains, no signature of an underlying bedrock could be found in the results. The LCI results of the remaining profiles look similar monotonous and are

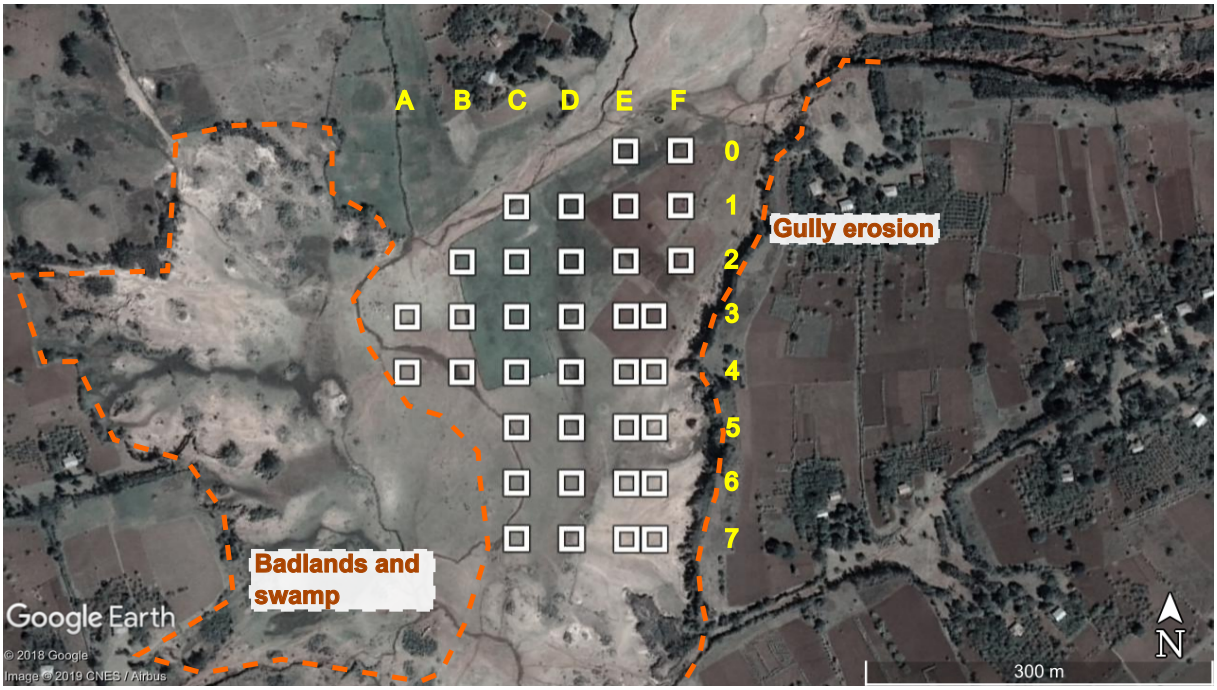

Figure 5.7.: *Survey area and grid of 35 TEM stations at Bisare River. Stations 3 - 7 of profile F had to be shifted 25 m west due to the gully erosion ridge.*

not shown. The second conclusion is that the Occam R1 and R2 inversion results indicate a slight increase of resistivity with depth for all profiles. But resistivities do not exceed 2 Ωm.

5.1.2. Bisare River

The source area of the Bisare River (E 37.854, N 6.847) is located within the caldera of the Hobitcha volcano 10 km east of Wolaita Sodo in southern Ethiopia. The volcanically-formed basin north of Lake Abaya serves as a sedimentary trap due to its natural geomorphologic shape. The Hobitcha caldera has an approximate maximum diameter of 6 km but only a small area in the center of the caldera was flat, unsettled and therefore suitable for TEM measurements.

At Bisare River, a 2D grid of 35 TEM stations was measured covering an area of approximately 300 × 500 m^2, see Figure 5.7. The station distance was 50 m in both lateral dimensions. For each sounding, the vertical and one horizontal $\dot{B}$ component was recorded but this time, a 50 × 50 m^2 square loop was used as a transmitter. For the receivers, we utilized a 20 × 20 m^2 single square loop for the NT mode and a Zonge TEM/3 coil for the ZT mode. The direction of the Zonge TEM/3 coil for the horizontal component again was east-west aligned and therefore quasi perpendicular to the surrounding caldera. However, the position of the survey area inside the caldera was probably too central to expect identifiable 2D patterns in the recorded data.

The survey area was restricted to the east by gully erosions with heigths of approximately 5 m. In the west, badlands and swamps from the Bisare River limited the area. Figure 5.7 shows the locations of 35 TEM soundings and their grid positions from A - F in east-west

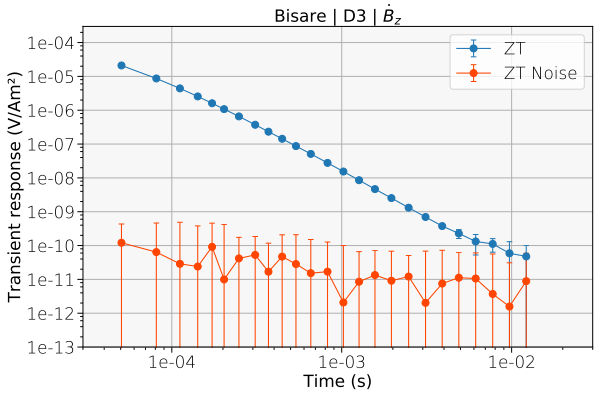

Figure 5.8: *ZeroTEM transient ($\dot{B}_z$) and noise floor of station D3 at Bisare River.*

and 0 - 7 in north-south direction. Stations 3 to 7 of profile F needed to be shifted 25 m to the west because of the erosion ridge. The acquisition time of the receiver was shorter than in the Chew Bahir survey because the main goal was not only to investigate the subsurface as deep as possible but also to record as many soundings as possible and cover a large area.

Figure 5.8 shows exemplary ZeroTEM field data ($\dot{B}_z$) and a noise measurement of station D3 from the center of the survey area. The noise level was in the order of 10^{-10} V/Am^2 and below for late times.

1D inversion results and $\rho_{a,lt}$ conversions of selected stations D2, D4 and D6 of profile D are shown in Figure 5.9. The inversion results indicate that, in general, the resistivity is increasing with depth below the first layer which is usually just a couple of meters thick. Moreover, the Occam inversion results (green and purple lines) show clear indications that at depths around 100 m, the resistivity is again increasing which is interpretated as a possible signature of the crystalline bedrock. This assumption is supported by an increase of resistivity in the $\rho_{a,lt}$ conversions in Figure 5.9.

The starting model for the Marquardt inversions and for the subsequent constrained inversion was a 4 layer model derived from the Occam inversion results. The thicknesses of the first three layers in the starting model have been set to 5, 10 and 80 m, the resistivities of all four layers have been 20, 10, 20 and 100 Ωm, respectively (from top to bottom).

Qualitatively, the inversion results of the other stations look similar and they are shown in Appendix A. Only the depth of the resistive bottom layer is slightly changing from north to south.

On the data set of Bisare River, a spatially constrained inversion was performed that generates a quasi-3D resistivity distribution of the subsurface. In contrast to the LCI where the constraints are set between adjacent stations along a single profile, the constraints of an SCI are horizontally defined between model parameters of neighboring soundings in two dimensions. The constraints are generated using a Delaunay triangulation which ensures an automatic adaption to data density variations. An SCI produces laterally smooth inversion results with sharp layer boundaries reflecting the geology of sedimentary settings (*Viezzoli et al.*, 2008).

Figure 5.10 shows linearly-interpolated and Gaussian-smoothed SCI results of two centrally located profiles: the north-south oriented profile D and the east-west oriented profile

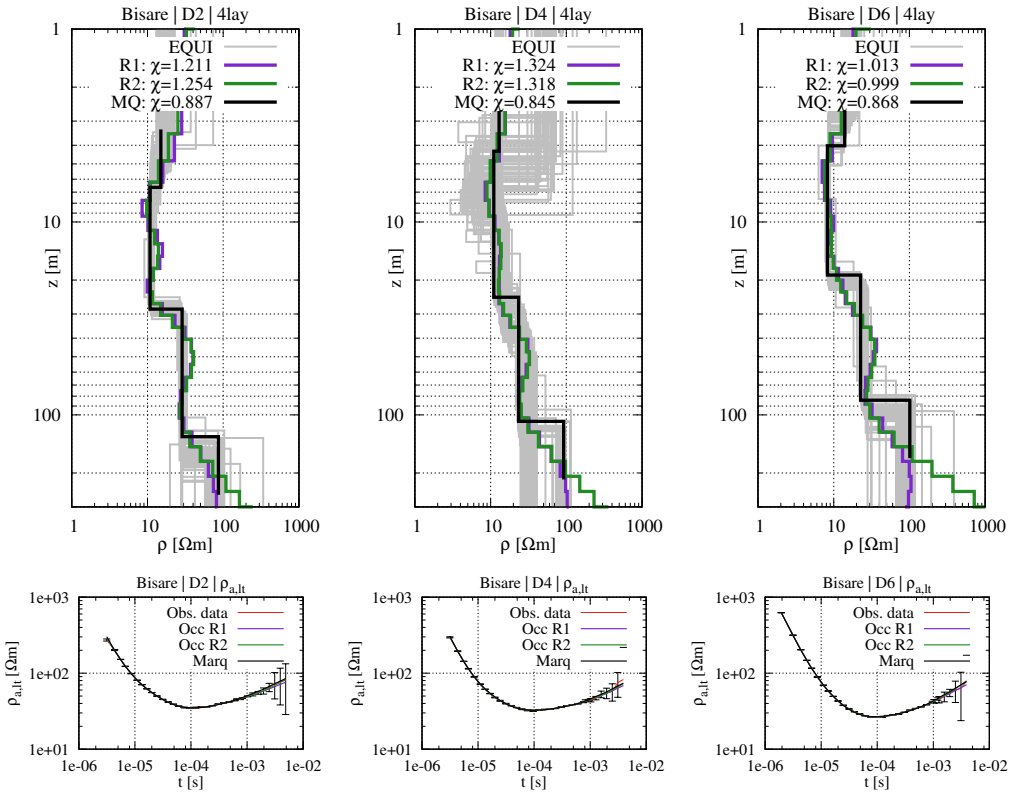

Figure 5.9.: *1D inversion results and $\rho_{a,lt}$ conversions (data and fittings) for selected soundings D2, D4 and D6 of profile D at Bisare River.*

4. In both images, the formerly mentioned four layers can clearly be distinguished. The top layer consists of a $\sim$ 5 m thick overburden with resistivities of about 10 to 20 Ωm. The second layer is more conductive with resistivities of 5 to 10 Ωm and a thickness of 10 to 15 m. The third layer has a resistivity of 20 Ωm and reaches down to approximately 80

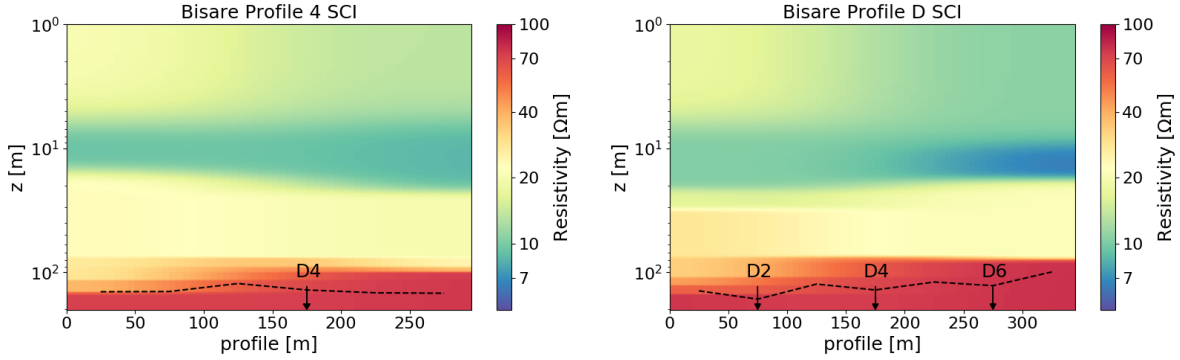

Figure 5.10.: *Interpolated and smoothed SCI results of Bisare River profiles 4 and D. The position of stations D2, D4 and D6 shown in Figure 5.9 are marked with black arrows for comparison. The dashed line denotes the DOI provided by the AarhusInv software.*

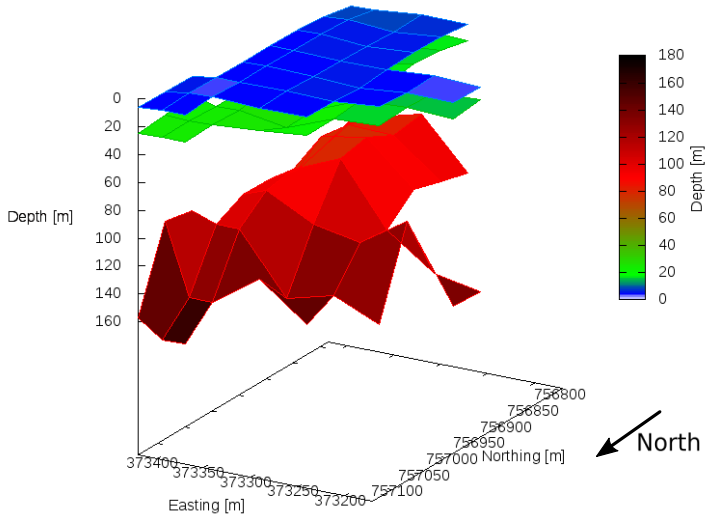

Figure 5.11.: *3D view of the SCI results from the Bisare River survey. The colors denote the depths of the boundary layers.*

- 100 m. Assumed to be the underlying bedrock, a fourth layer follows with resistivities of $\sim$ 100 Ωm. The SCI results of all profiles from the survey at Bisare River are shown in Appendix B.

To what extents these results can be trusted may be answered by looking at the exploration depths. The DOI after *Meju* (1995) yields values of approximately 150 m for t_{max} = 7 ms, I = 10 A, and a conservative choice of $\sigma = 0.1$ S/m. The DOI from the AarhusInv software provides values between 100 and 150 m, these DOIs are plotted as black dashed lines in Figure 5.10. Therefore, a resistive fourth layer is assumed to be existent. If it is the underlying crystalline bedrock or just a resistive layer - maybe of volcanic origin - remains to be clarified.

Nevertheless, Figure 5.11 shows an SCI generated 3D view of the three layer boundaries. The colors denote only depths, not the electrical resistivity. For a more realistic perception of the result, the depths axis is plotted linearly. The blue layer represents the first layer boundary at depths of approximately 5 m followd by the second layer boundary in green denoting depths of about 20 m. In the southern region of the survey area, the boundary between the third and the fourth layer is 80 to 100 m deep (red). The layer is dipping towards the north where it is reaching depths of about 150 m. Regardless of the nature or composition of the resistive bottom layer, sediment thicknesses are therefore assumed to be of up to 150 m.

5.1.3. Dendi Lakes

The double crater system of the Dendi Lakes is located at Mount Dendi (3270 m asl, E 38.02, N 8.836) 80 km west of Addis Ababa on the West Central Ethiopian Plateau. The oval shaped caldera of Mount Dendi has an approximate diameter of 6.5 to 8.5 km and it contains two round lakes in the center of the crater's depression. Each lake has a diameter of approximately 2.5 km and nowadays they are connected via a relatively

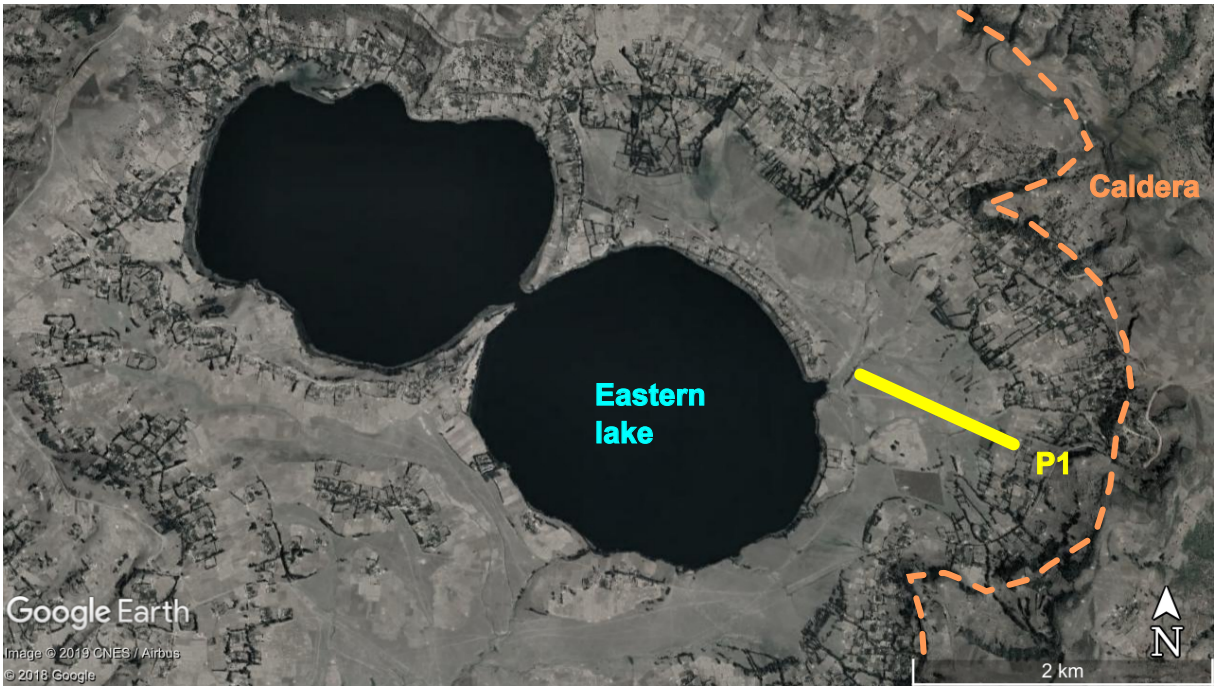

Figure 5.12.: *Survey area of the Dendi Lakes and profile P1 containing 23 TEM stations.*

shallow sill (*Wagner et al.*, 2018). The maximum altitude difference between the caldera's peaks and the surface of the lakes is 440 m.

At the shore of the eastern lake, one TEM profile containing 23 TEM stations was recorded. The length of the profile was 1,150 m and it was aligned approximately east-west. To the west, the profile was starting near the shore and in the east it was reaching as close as possible to the beginning slopes of the caldera. Again, 50×50 m^2 square loops were deployed as a transmitter. For the receivers, a 20×20 m^2 square loop was used for the NT mode and a Zonge TEM/3 coil for the ZT mode. The horizontal component was measured along the profile direction, perpendicular to the sea shore and the surrounding caldera in the east.

Figure 5.13 shows an exemplary ZeroTEM transient ($\dot{B}_z$) and a noise measurement of station P1-01. The noise floor can be determined to be around 10^{-10} V/Am^2 for intermediate times and 10^{-11} V/Am^2 for the very late times.

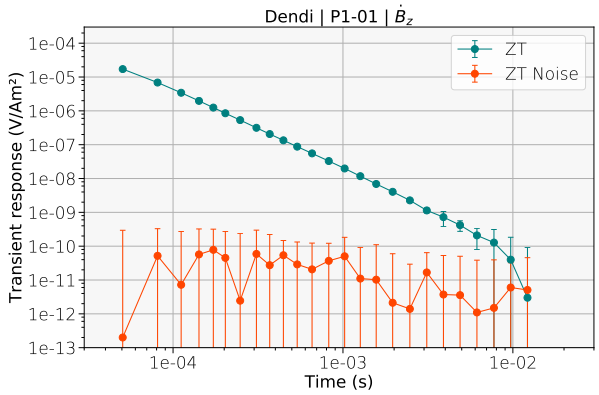

Figure 5.13: *ZeroTEM transient ($\dot{B}_z$) and noise floor of station P1-01 at the Dendi Lakes.*

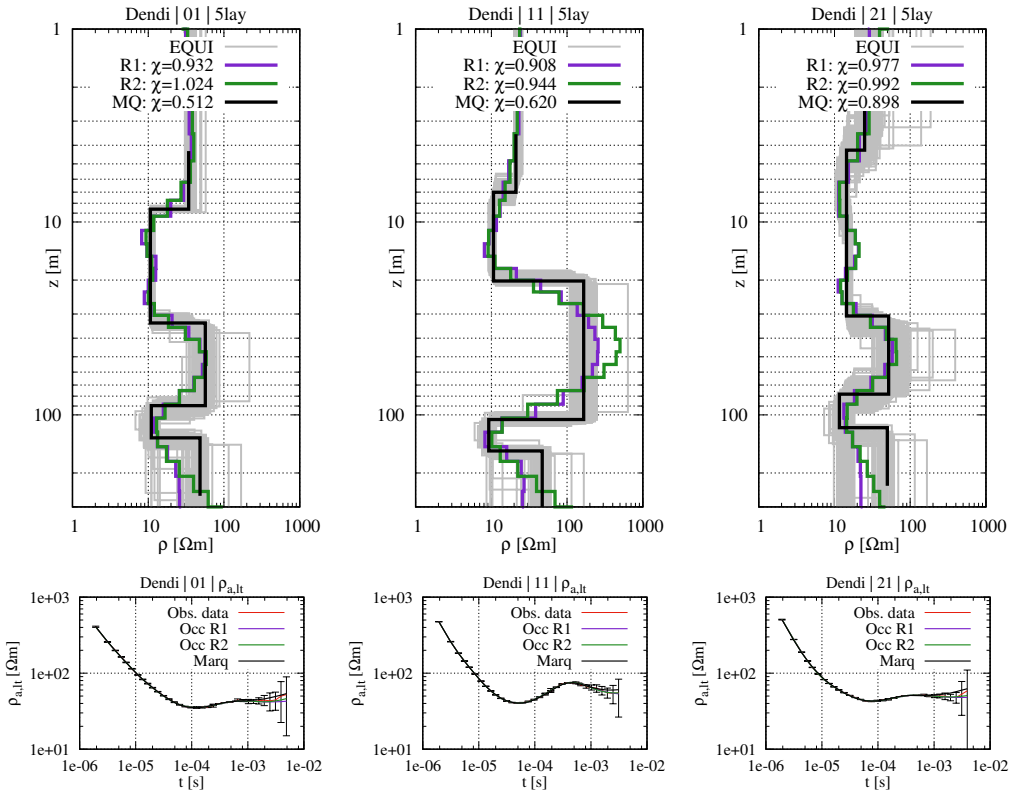

Figure 5.14.: *1D inversion results and $\rho_{a,lt}$ conversions (data and fittings) for selected soundings 01, 11 and 21 from Lake Dendi.*

1D inversion results and $\rho_{a,lt}$ conversions of selected stations 01, 11 and 21 of the Lake Dendi profile are shown in Figure 5.9. For station P1-01, the Occam R1 and R2 inversion results insinuate a 4 or a 5 layer subsurface, depending on how trustworthy the increase of resistivity at a depth below 100 m is assumed to be. This increase of resistivity at depths below 100 m can be observed at many stations throughout the profile. 1D inversion results of the remaining stations are shown in Appendix A.

From the images showing the $\rho_{a,lt}$ transformations in Figure 5.9, an increase of the apparent resistivity at very late times can be observed, but these values provide large error bounds. Regarding the conventional 1D inversion results, the existence of a resistive 5th layer is uncertain. The Monte Carlo inversions of stations 01 and 11 indicate that the measured data can be explained by a many 5-layer equivalent models that comprise a resistive 5th layer. However, a resistive 3rd layer with resistivities of up to 100 Ωm and from depths of minimum 20 m to a maximum of 100 m can clearly be seen in the results.

The starting model of the Marquardt and Monte Carlo inversions was a five layer model consisting of the following model parameters. The thicknesses have been set to 5, 25, 40 and 40 m and the resistivities to 30, 10, 50, 10 and 50 Ωm, respectively (from top to bottom).

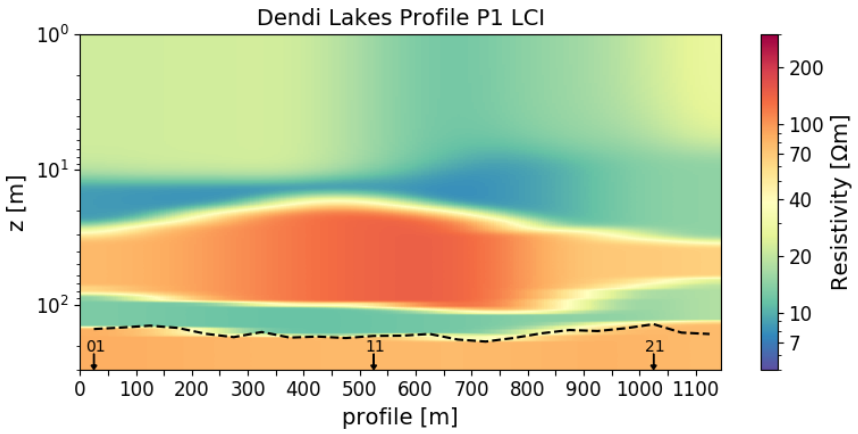

Figure 5.15.: *Interpolated and smoothed LCI result of profile P1 from the Dendi Lakes. The position of stations 01, 11 and 21 shown in Figure 5.14 are marked with black arrows for comparison. The black dashed line denotes the DOI provided by the AarhusInv software.*

On the data set from the Dendi Lakes, a laterally constrained inversion was performed as well. An interpolated and smoothed image of the LCI result is shown in Figure 5.15 together with the DOI value of the AarhusInv software between 140 and 190 m (black dashed line). The DOI after *Meju* (1995) yields values of 170 m with t_{max} = 5 ms, I = 10 A and a mean conductivity of 0.05 S/m (= 20 Ωm). As a first approximation, the exploration depth coincides with the depth of the boundary between the 4th and the 5th layer from the inversion result. Thus, the existence of this resistive bottom layer is questionable from the viewpoint of the TEM results.

The recorded data of station P1-22 turned out to be defective and could not be used for an inversion afterwards. Unfortunately, this was not noticed during field work. To include it nonetheless into the LCI inversion, data for station 22 was generated synthetically by building average thickness and resistivity values from adjacent stations 21 and 23.

Conclusively, conventional 1D Marquardt and Occam inversions as well as the laterally and spatially constrained inversion yielded the following results:

- At Chew Bahir, no bedrock or any other sharp resistivity contrast could be detected with exploration depths of about 150 to 200 m on all profiles. The very conductive, saline subsurface hindered greater investigation depths. From the ICDP drillings, it can be concluded that the thickness of the sedimentary deposits underneath station P1-16 is at least 280 m. On the western shore of Chew Bahir, the TEM results show minimum sediment thicknesses of 150 - 200 m.

- At Bisare River, a sedimentary layering and a resistive bottom layer with resistivities of approximately 100 Ωm could probably be detected. The composition of this resistive layer remains to be clarified. Sediment thicknesses are assumed to be about 100 m in the southern region of the survey area and up to 150 m in the northern part of the investigated area.

- The survey at Lake Dendi provided no reliable evidence about reaching a resistive bedrock. Instead, only indications of an increasing resistivity at very late times

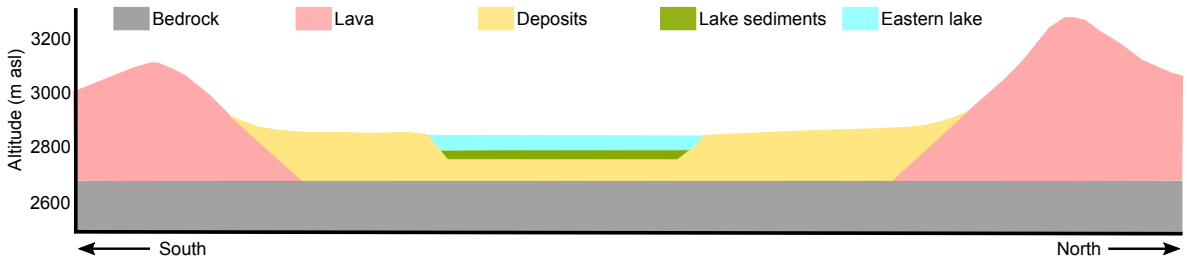

Figure 5.16.: *Simplified geological model of the Dendi Lakes after Zinaye (2014). The cross-section is north-south oriented and cuts through the eastern lake.*

could have been detected. Further research is necessary to clarify the existence of such a layer. At depths between 20 and 100 m, a comparably resistive layer with resistivities of 100 Ωm was detected in the conventional 1D inversion results as well as in the constrained inversion results. The sediments at Lake Dendi are assumed to be at least 150 m thick underneath the survey profile.

Comparing all results of the 1D Marquardt and LCI/SCI inversion results qualitatively leads to the conclusion that both techniques provide more or less comparable results, at least for the field data examined in this chapter. A quantitative comparison between both approaches was not performed.

In the appendices of this thesis, all 1D inversion results and the remaining SCI cross-sections from Bisare River are shown as well as impressions and pictures of the three field trips to Ethiopia.

5.2. 1D Modeling of Data from Lake Dendi

In the preceding chapter, the 1D and LCI inversion results of the $\dot{B}_z$ component from the TEM profile at Lake Dendi produced no reliable evidence of a resistive bedrock layer in the depth. Only indications of an increasing resistivity at late times could be derived from the data. The calculated exploration depths were approximately the same than the depth of the boundary between the 4th and a possible 5th (resistive) layer. Thus, an interpretation of a possibly detected bedrock at depths around 150 - 200 m is uncertain.

Zinaye (2014) presented a simplified geological model of the Dendi caldera. Figure 5.16 shows a revised version of this model as a north-south oriented cross-section cutting through the eastern lake. The model consists of the surrounding crater made up from lava flows and igneous rocks sitting on top of the trachyte and rhyolite bedrock. Inside the caldera, a layer of sedimentary deposits (yellow area in Figure 5.16) is found. According to *Zinaye* (2014), these deposits are made of a 10 m thick overburden of alluvial sediments followed by pyroclastic deposits (volcanic ashes, lapilli tuff and ignimbrite).

The eastern lake has nowadays a water depth of 56 m and it is located 2836 meters above sea level (*Wagner et al.*, 2018). In 2012, two corings were carried out from floating platforms on the eastern lake penetrating the lake sediments 10 and 8.5 meters, respectively. Stiff sediments prevented the drillings from further penetration into the lake sediments

Layer No	Resistivity [Ωm]	Thickness [m]
1	20	10
2	10	10
3	100	80
4	10	variable (20 - 200)
5	variable (10 - 10000)	

Table 5.1.: *5-layer model of the sedimentary deposits at Lake Dendi. The thickness of layer 4 was varied from 20 to 200 m and the resistivity of layer 5 was varied from 10 to 10,000 Ωm to assess the detectibility of a resistive bedrock layer.*

(*Wagner et al.*, 2018). During the field work, banks of tephra outcropping in the vicinity of the western end of the TEM profile could be found. However, only sparse information about the bedrock geology and the soils surrounding the lakes is available (*Wagner et al.*, 2018).

The deposits layer in the geological cross-section (Figure 5.16) is supposed to have a thickness of approximately 200 m. From the TEM measurements, the depth of the bedrock was estimated to be ∼ 150 m. To investigate until what depth a possible resistive 5th layer could have been detected reliably with the utilized TEM configuration, several 1D forward calculations with the 1D code EMUPLUS have been performed. EMUPLUS was chosen instead of TDcustEM as a forward routine because 1D modelings using a semi-analytic solution are much faster and more accurate than calculating a 5-layer model using 3D finite elements.

The underlying synthetic model for this study is presented in Table 5.1, it has been derived as an estimation from the TEM LCI results shown in Figure 5.15. For the forward calculations, the transmitter was a 50 × 50 m^2 inductively coupled loop and the $\dot{B}_z$ receiver was placed in the center of the transmitter. All data were normalized to 1 A and to 1 m^2.

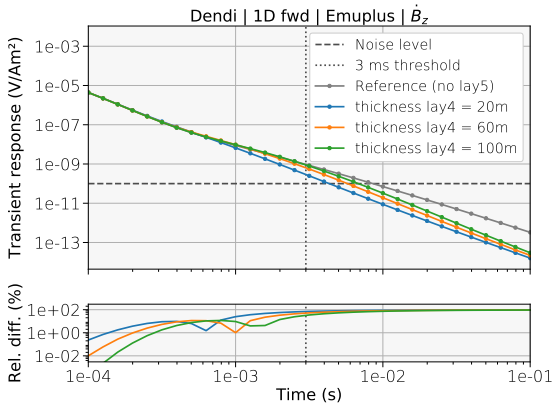

Figure 5.17.: *Selected 1D forward calculated transients of varying the 4th layer thickness of the Lake Dendi sediments model (Table 5.1). In grey, the transient for the reference model without a 5th layer is plotted.*

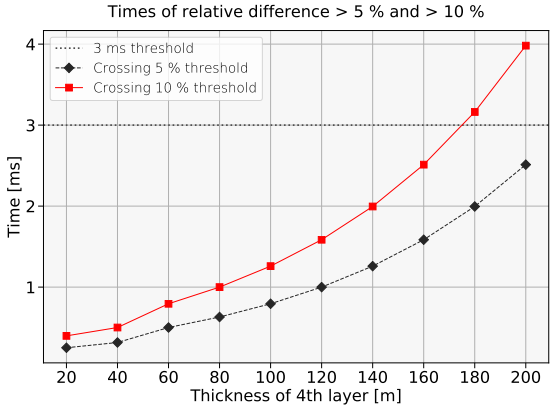

Figure 5.18.: *Times when the relative difference between the reference model and a 5-layer model depending on the thickness of the 4th layer reaches a specific threshold of 5 and 10 %.*

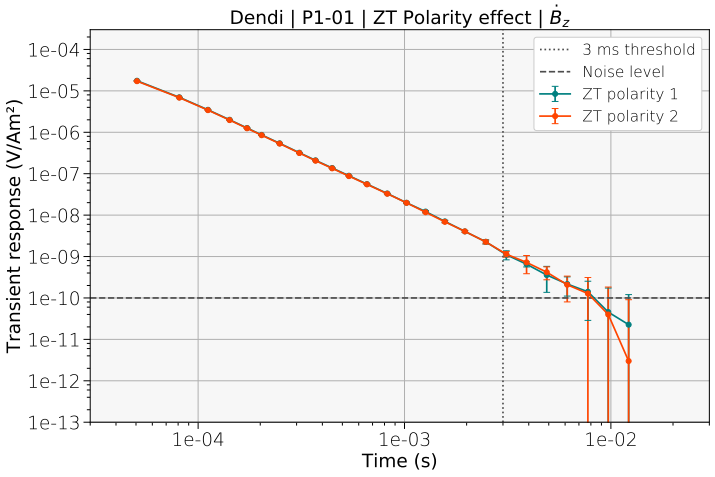

Figure 5.19: *Polarity effect of ZT data from Lake Dendi. After 3 ms, the transients of both measured receiver polarities are diverging.*

First, the thickness of the fourth layer, and therefore the starting depth of a possible 5th layer, has been varied from 20 to 200 meters (implying that the depth of the 5th layer was varied from 120 to 300 m, because the cumulated thickness of the first three layers is 100 m). The reference model is a 4-layer model without a resistive bedrock, i.e. the thickness of layer 4 is infinite.

Figure 5.17 shows the modeled transients of selected layer 4 thicknesses of 20 (blue), 60 (orange) and 100 (green) m together with the transient of the reference model (grey line). The noise level was set to 0.1 nV/Am^2 and the treshold for the last "trusted" time point, i.e. the time until that the raw ZT transient seems to have a clean progression, was set to 3 ms. Both values have been derived from Figure 5.13. A 4th layer thickness of 20 and 60 m can be visually distinguished in Figure 5.17, for a 4th layer thickness of 100 m it is difficult.

To assess a possible detectability of a 5th layer depending on the thickness of the 4th layer quantitatively, Figure 5.18 shows the times when the relative difference between the forward calculated data of one specific 4th layer thickness and the reference transient reaches 5 % (black line) and 10 % (red line). Assuming a 10 % difference between the reference transient and a 4th-layer thickness varied transient is sufficient to detect the bedrock layer, a 270 m deep 5th layer would still be detectable (equal to a 4th layer thickness of 170 m). Assuming a 5 % difference to be sufficient, even a 300 m deep 5th layer would be detectable (equal to a 4th layer thickness of 200 m).

The last "trusted" time point was confirmed by an additional assessment of raw ZT data. The GDP-32II receiver device is affected by a so called *polarity effect* which leads to different receiver signals at very late times when interchanging the polarity of the physical receiver loop or coil (*Yogeshwar*, 2014). The ZT data is treated as being trustworthy only for the time channels when the recorded signals of both polarities are the same (within a reasonable error margin). The data from time channels where both polarities are diverging are not used for inversion. Figure 5.19 shows the polarity effect for ZT data from station P1-01 from the Dendi Lake data set. Not only do the transients start to diverge after 3 ms, but also the error bars start to become significant.

Second, the resistivity of a possible 5th layer is varied to examine a potential detectability. Forward modelings with 5th layer resistivities of 10 to 10,000 Ωm have been calculated for 5th layer depths of 150 and 200 m (see Figure 5.20). The black lines for $\rho_5 = 10$ Ωm is

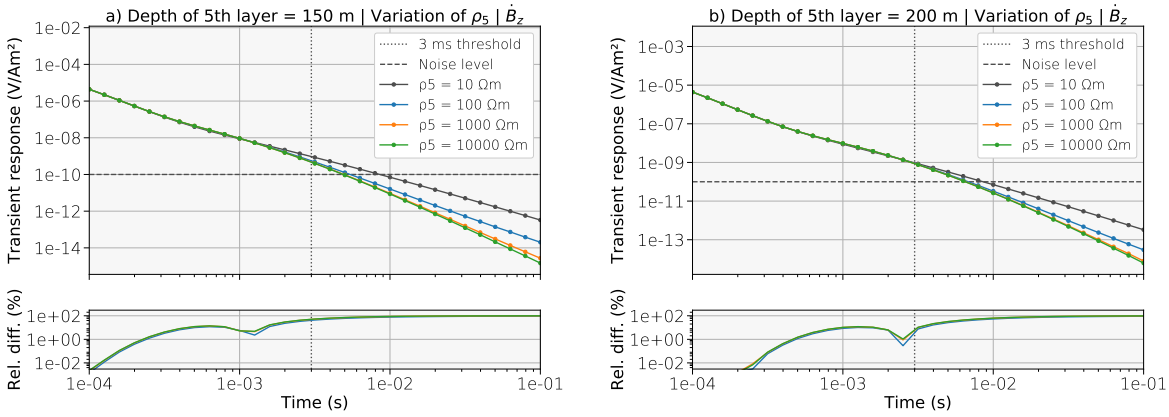

Figure 5.20.: *Variation of the 5th layer resistivity of the Lake Dendi sediments 1D model (Table 5.1) for a 5th layer depth of a) 150 m and b) 200 m.*

equal to a 4-layer model without a resistive 5th layer. Assuming the 4th layer to be only 50 m thick (Figure 5.20a), a detection of the 5th layer seems realistic. For a 4th layer thickness of 100 m (Figure 5.20b), a discrimination of the transients before 3 ms is hardly possible.

Conclusively, the 1D forward modelings showed that bedrock depths of 150 m underneath the deposits, as indicated by the inversion results, should be detectable in the data - although only marginally. However, detecting a bedrock at depths of 200 m, as proposed by the simplified geological model in Figure 5.16, is difficult and unlikely when applying the utilized TEM configuration. The question, if signatures of a resistive 5th layer can be found in the $\dot{B}_z$ field data from Dendi and if a resistive bedrock layer was detected during the survey, can not be finally clarified.

5.3. 3D Modeling of Data from Lake Dendi

Two components of the electromagnetic field have been measured during the field campaign at the Dendi Lakes. The vertical $\dot{B}_z$ component and the horizontal $\dot{B}_x$ component, facing south-east into the profile direction. While in the previous section, a 1D modeling of the vertical component has been conducted, this section concentrates on the investigation of $\dot{B}_x$ and $\dot{B}_z$ using 3D forward modelings of the Dendi crater including topography with TDcustEM.

The applied digital elevation model (DEM) was generated from topographic data of NASA's Shuttle Radar Topography Mission (SRTM)[15] with a resolution of 1 arc-second (approximately 30 meters). The 3D model consists of an igneous bedrock, the volcanic crater, sedimentary deposits and the eastern lake. The dimension of the primary model is $3.5 \times 3.5 \times 3.5$ km^3, a tetrahedron boundary extents the entire domain by a factor of 10. The x-direction of the domain is pointing eastwards, the y-direction towards north. The depth is defined by the negative z-direction.

[15]https://www.jpl.nasa.gov/srtm/

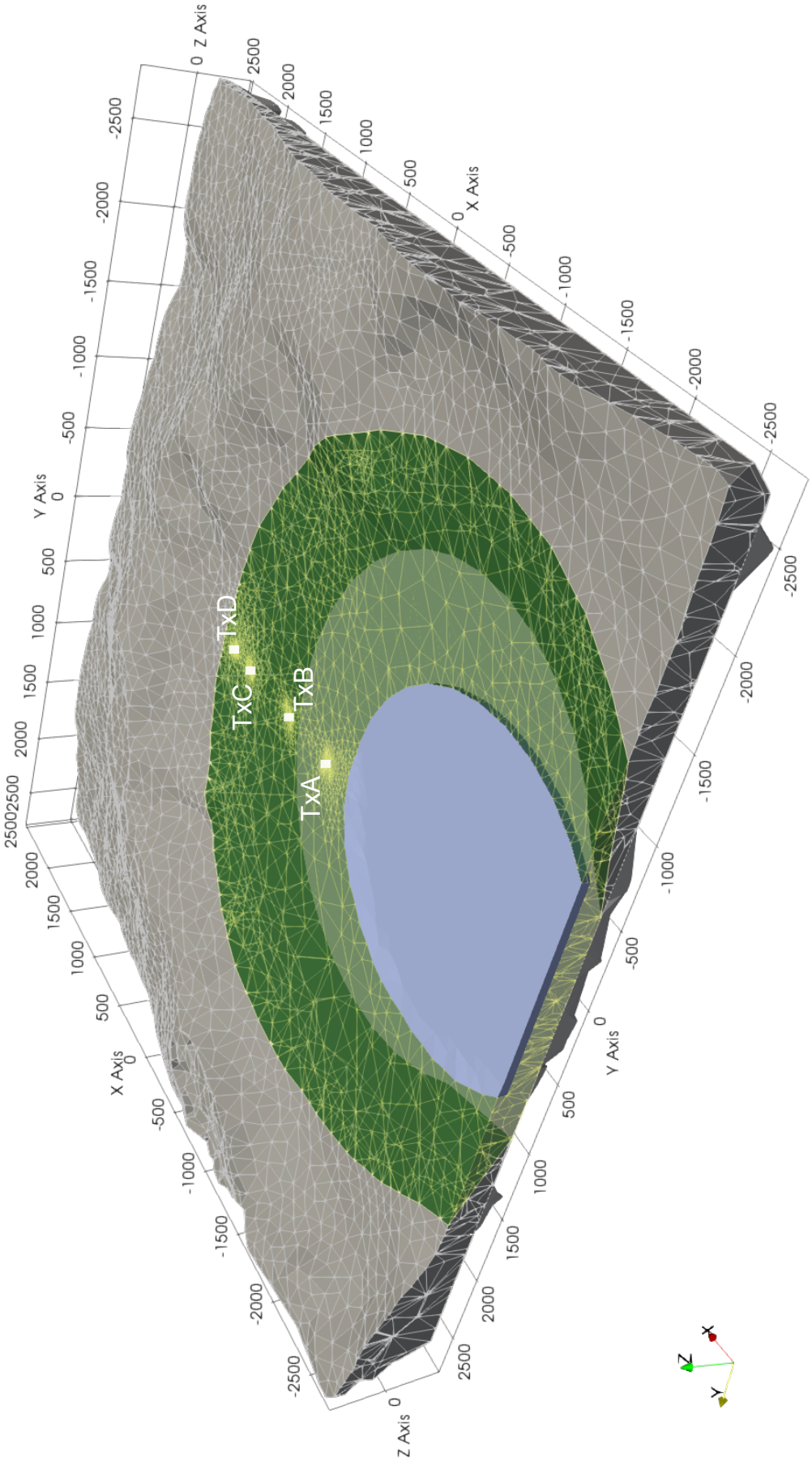

Figure 5.21.: *3D model of the eastern Dendi Lake and the survey area for the 3D forward calculations with TDcustEM. The four investigated transmitter/receiver locations are marked as TxA, TxB, TxC and TxD. To make the subsurface slope visible, the sedimentary deposit is displayed transparent. The y-direction points towards north (Clipped view of the entire simulation domain).*

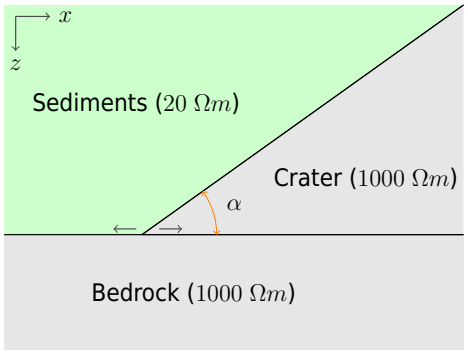

Figure 5.22: *2D Sketch of the dipping subsurface crater rim at the eastern Lake Dendi. The angle α is varied from 20 to 70 degrees simulating differently inclined slopes. When changing the angle, the foot of the slope is moved towards or away from the basin center.*

The artificial geometry of the sedimentary basin and the eastern Dendi lake is designed to resemble the setting of the survey area. The basin and the lake are approximated by 32 segments to form an oval and therefore not shaped perfectly round. Figure 5.21 shows a clipped view of the 3D mesh where the air layer is masked out and the depth is only shown until z = -350 m. The z = 0 m level is set to the surface of the lake (blue area in Figure 5.21), which in reality is 2833 m asl. The water depth of the lake is 50 m. In grey, the surrounding volcanic crater is displayed and in green the sedimentary basin. For a clearer visibility of the 3D domain, the tetrahedral mesh of the lake is not shown and the sedimentary basin is displayed transparent.

The sediment layer thickness was set to 200 m based on the results and information of the preceding sections. In the present study, the subsurface slope of the basin (the dark green area in Figure 5.21) is varied. Simulations have been conducted for subsurface slope angles of 20, 30, 45, and 70 degrees, where 70 degrees denote a steep inclination and 20 degrees a flat and gentle dipping, see Figure 5.22. When changing the slope angle, the boundary of the sediment basin at the surface remains fixed and the subsurface boundary at a depth of 200 m is moved towards the center of the basin.

The specific resistivity of the trachyte and rhyolite bedrock and the igneous crater are assumed to be the same and set to 1000 Ωm. The resistivity of the sedimentary deposits and the lake are set to 20 Ωm. The lake is assumed to have no impact on the results because of the lateral distance to the closest modeled central-loop position. Moreover, possible effects of the lake on the transients in 3D is not in the scope of this study.

Four transmitter/receiver positions in the central-loop configuration have been computed, labeled TxA, TxB, TxC and TxD. The transmitter size was 50 × 50 m^2 each as it was during the survey. The induced current was 1 A. All four transmitter/receiver positions are arranged along one profile facing into the positive x-direction towards east and therefore perpendicular to the crater rim. TxA is located in a distance of approximately 200 m to the lake at coordinates (-650,0). In a distance of 500 m each, TxB and TxC are located at coordinates (-150,0) and (350,0). TxD, which is located another 200 m in eastern direction, is closest to the caldera at coordinates (550,0). Due to the applied topography, the z-coordinates of the transmitter/receiver locations are increased. TxA and TxB are ∼ 10 m above the zero-level, TxB is elevated by ∼ 40 m and TxD by ∼ 50 m. If not reduced by the inclined crater slope, the sediment thicknesses underneath each location is increased by these elevations. The modeled time range throughout this study is 10^{-6} to 10^{-2} s.

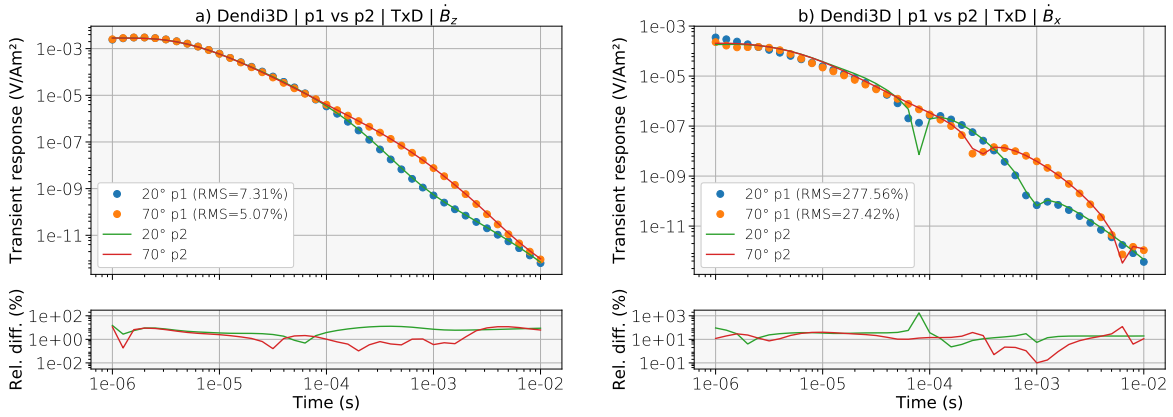

Figure 5.23.: *Comparison of polynomial degrees $p = 1$ and $p = 2$ for transmitter location TxD and slope angles of 20 and 70 degrees. The left-hand side images (a) show the modeled component $\dot{B}_z$ and on the right side, the results of $\dot{B}_x$ are dislayed (b). The relative differences and RMS errors correspond to calculations of the same slope angle using $p = 1$ and $p = 2$.*

Transmitter TxA serves as a reference station far away from any possible effects of the modeled subsurface slope. TxB is located approximately above the foot of the flattest slope. TxC and TxD are in the vicinity of the crater rim. TxD is 130 m away from to the border of the sedimentary basin. For the flattest slope angle of 20 degrees, the thickness of the sediment layer underneath TxC is $\sim$ 100 m and underneath TxD $\sim$ 40 m. Therefore, the dipping volcanic layer is assumed to have a significant effect on the transients of locations TxC and TxD.

Differently from the displayed mesh in Figure 5.21 where all four transmitter locations are meshed, visible and marked, the meshes designed for the actual 3D computations contained only the specific transmitter location of interest. The meshes consisted of 100 k cells on average. Whether a fast computation using a polynomial degree of p = 1 is sufficient or a more time consuming computation with a polynomial degree of p = 2 is necessary is to be answered first.

Figure 5.23 shows the comparison of the p = 1 (p1) and p = 2 (p2) transients for the vertical $\dot{B}_z$ (5.23a) and the profile-directed $\dot{B}_x$ component (5.23b). The chosen transmitter location is TxD and the investigated slope angles are 20 and 70 degrees (i.e. the steepest and the flattest modeled inclination). The 2D effects of the underlying dipping crater are obvious in both components. The transients of the vertical component progress steeper at late times, as expected, this effect appears earlier for the 20° inclination. The horizontal in-profile component sees two sign reversals at intermediate to late times. Again, these sign reversals appear earlier for the 20° inclination.

For the vertical component, the difference between p1 and p2 looks marginal but the RMS errors are still 5.07 % for the 70° slope and 7.31 % for the 20° slope case. For a general modeling study of field data, these differences might be acceptible. However, taking a look at the horizontal component reveals that a computation with a more accurate polynomial degree is necessary.

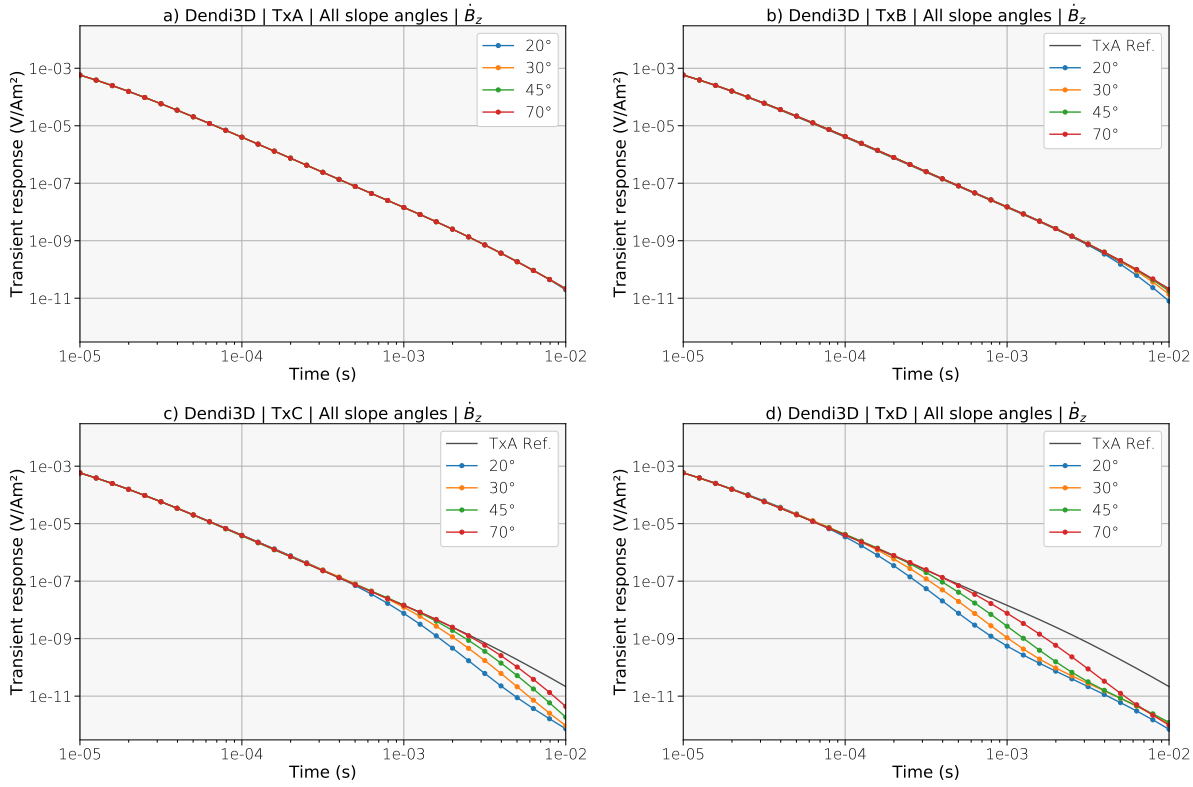

Figure 5.24.: *Vertical component $\dot{B}_z$ for transmitter/receiver locations a) TxA, b) TxB, c) TxC and d) TxD for simulated inclinations of the subsurface slope from 20 to 70 degrees.*

The RMS error between the p1 and p2 simulations are 27.4 % for the steep 70° slope and an even higher 277.6 % for the flatter 20° slope for the $\dot{B}_x$ component. These high RMS errors can only in parts be explained by the two sign reversals. For the majority of the calculated time channels, the relative difference between p1 and p2 is more than 10 %.

The results in Figure 5.23 suggest the following: The closer the dipping subsurface to the receiver location is (i.e. the more shallow the resistive bedrock is), the greater the impact on the differences between the p1 and p2 calculations is. Finally, all forward calculations for the 3D Dendi model have been performed using the polynomial degree of p = 2.

5.3.1. The Vertical Component $\dot{B}_z$

The results for the vertical $\dot{B}_z$ component of all four transmitter/receiver locations TxA, TxB, TxC and TxD are displayed in Figure 5.24 a-d. For each location, the transients for the simulated subsurface slope angles of 20° to 70° are shown. TxA serves as a quasi-reference station without being affected by any subsurface inclination. Except the topography, the subsurface underneath TxA can be considered as 1D. The $\dot{B}_z$ transient of the 70° slope calculation of TxA is plotted in the subfigures of TxB, TxC and TxD to emphasize 2D/3D effects. For a finer view on the results, only the time range from 10^{-5} to 10^{-2} s is shown, the data of the first decade before 10^{-5} s exhibits no signatures of a dipping subsurface.

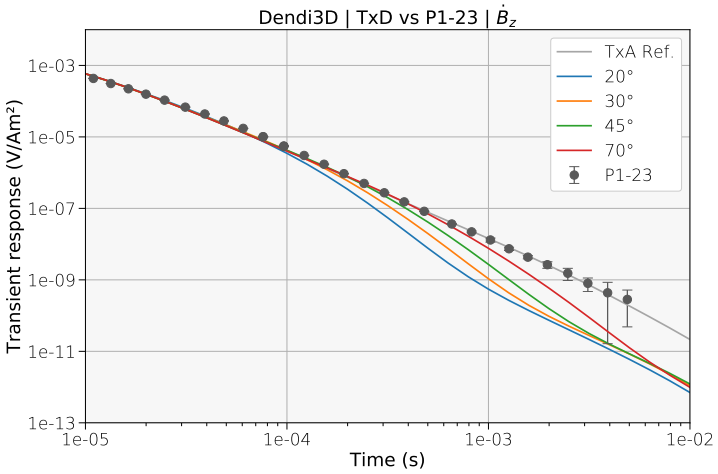

Figure 5.25: *Synthetic $\dot{B}_z$ data from location TxD for different slope angles (colored transients) and the reference station TxA (grey transient) compared to $\dot{B}_z$ field data from Lake Dendi station P1-23 (dark grey dots).*

The suitability of TxA being a quasi-reference station can be substantiated by Figure 5.24a. For all modeled slope angles, the transients look almost the same. At very late times, the transients progress slightly steeper which is related to the resistive volcanic bedrock layer at 200 m depth. For the 20° inclination model, the foot of the dipping slope is located more than 600 m away. The diffusion depth (Equation 5.3) for the latest time channel 10^{-2} s is only $\sim$ 560 m.

Regarding the location TxB, a prominent effect of the dipping crater is only visible for the 20° case and only the last 5 time channels. The transients for the steeper slope angles are hardly distinguishable visually. On the other hand, locations TxC and TxD exhibit considerable signatures that can be attributed to the inclined subsurface. The less the inclination is and the more shallow it is located under the surface, the greater is the resulting impact on the $\dot{B}_z$ transient. If the transients of TxC and TxD would be interpreted in a 1D inversion, the results for the flat angles would probably be a false 3-layer model.

Figure 5.25 shows the synthetic $\dot{B}_z$ transients from location TxD for all modeled slope angles together with the reference station TxA and together with real $\dot{B}_z$ field data from station P1-23 of the Dendi Lakes survey. The location of TxD within the 3D tetrahedral model resembles the location of station P1-23, which is the eastern-most station of the survey profile P1 (see Figure 5.12) closest to the caldera. If a possible slope effect can be seen anywhere in the field data, station P1-23 is the most promising candidate. But the modeled slope angles for location TxD (colored transients in Figure 5.25) differ considerably from the field data of station 23. Even the transient of the relatively steep 70° model deviates significantly from the field data. Instead, the measured P1-23 $\dot{B}_z$ transient fits the reference station TxA to a very good degree.

Hence, no traces of a 2D/3D effect based on a possible dipping crater rim underneath station P1-23 can be seen in the vertical component. The deviations of the field data to the synthetic data around 10^{-5} and 10^{-4} s is related to the simplification of the sedimentary basin in terms of resistivity. In the 3D model, the resistivity was set to a homogeneous 20 Ωm. As the 1D inversion results showed, this is not the case for the field data.

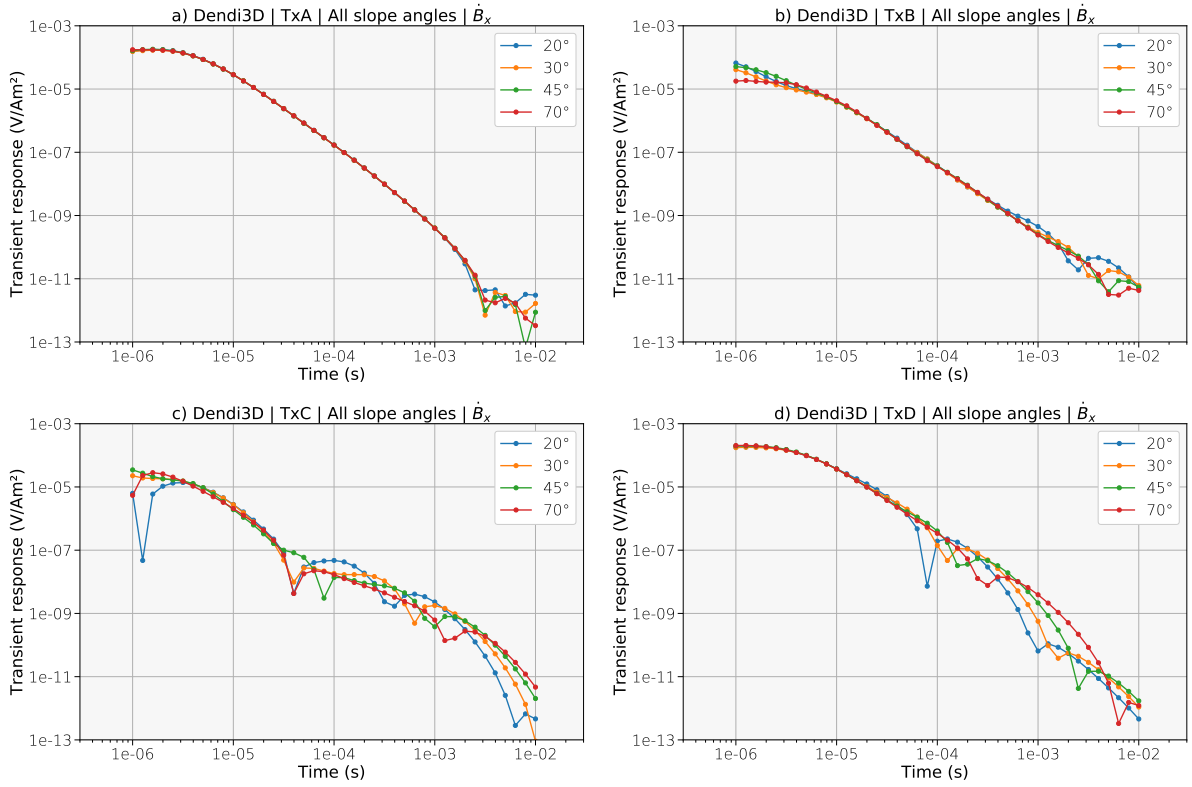

Figure 5.26.: *Horizontal component $\dot{B}_x$ for transmitter/receiver locations a) TxA, b) TxB, c) TxC and d) TxD for simulated inclinations of the subsurface slope from 20 to 70 degrees.*

5.3.2. The Horizontal Component $\dot{B}_x$

The results of the horizontal $\dot{B}_x$ component facing into the positive x-direction are shown in Figure 5.26 a-d, again for all four locations and all four slope angles. The first thing that stands out is that the transients of TxA and TxB look similar for all inclinations whereas the results of locations TxC and TxD show diverse transient shapes. Hence, 2D effects depending on the slope angles are evident in the data of TxC and TxD and non-existing at locations TxA and TxB.

The next interesting observation from the data concerns the magnitudes of the horizontal component. At a rough estimate, the magnitude of the horizontal component is between one and two orders less than the magnitude of the vertical component. However, due to the quasi-1D subsurface at transmitter location TxA (and for the steep inclination models for TxB), the horizontal components in the center of the loop are supposed to be zero. Moreover, the magnitude levels of locations TxA and TxD are similarly strong (around 10^{-4} V/Am^2) and the magnitude levels of locations TxB and TxC are similarly strong (less than 10^{-4} V/Am^2).

So what causes these relatively strong magnitudes, and what is the explanation for the two groups of magnitude levels? One possible explanation is the topography. Table 5.2 shows the elevation (z-level) of the corner coordinates of the four transmitter loop locations with topography being applied.

Location	SE [m]	SW [m]	NW [m]	NE [m]	Δ_{max} [m]
TxA	12.1	9.3	15.1	16.9	**7.6**
TxB	16.2	18.3	16.8	17.5	2.1
TxC	40.1	40.6	41.0	41.7	1.6
TxD	44.9	49.0	50.1	47.7	**5.2**

Table 5.2.: *Z-Coordinates of the four square loop transmitter vertices for locations TxA, TxB, TxC and TxD of the 3D Dendi model with applied topography. Δ_{max} is the maximum elevation difference between the four vertices per location.*

Here, SE, SW, etc. are the cardinal directions as seen from the loop center and Δ_{max} denotes the maximum elevation difference between all four corner vertices of one particular square loop. The highest Δ_{max} values with 5.2 m and 7.6 m can indeed be found for transmitters TxA and TxD, explaining the large horizontal magnitudes of these two locations. For TxA, the maximum difference of 7.6 m is between two opposite loop corners (SW and NE) therefore it corresponds to an inclination of approximately 10 %. The horizontal component $\dot{B}_y$ perpendicular to the profile direction has magnitudes of the same order than the $\dot{B}_x$ component for all locations. The lateral resolution of the applied DEM was 30 m which might be too coarse for a 50 × 50 m^2 transmitter loop.

In order to demonstrate the effect of the applied DEM model on the $\dot{B}_x$ transients, forward modelings of the Dendi 3D model with an inclination of 70° without topography have been conducted. Figure 5.27 shows a comparison of $\dot{B}_x$ data for stations TxA and TxD which are the most affected stations according to Table 5.2. Approximately, the magnitudes of the data without topography is of one order less for TxA. For TxD, this accounts only for the first two time decades. When the effect of the nearby slope takes over, both transients progress on a similar level.

Nevertheless, the horizontal component does not vanish - as expected at least for the location TxA where no 2D or 3D subsurface geometry is to be found nearby. The remaining $\dot{B}_x$ components may therefore be related to numerical reasons or are due to an insufficiently fine mesh. The magnitude of the vertical component is on average 10 times

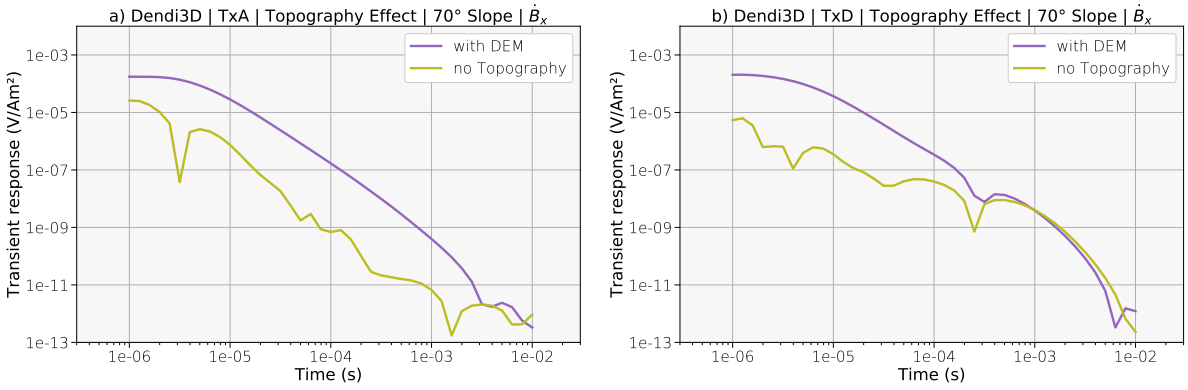

Figure 5.27.: *Horizontal component $\dot{B}_x$ for transmitter/receiver locations TxA and TxD with and without topography applied to the 3D Dendi model.*

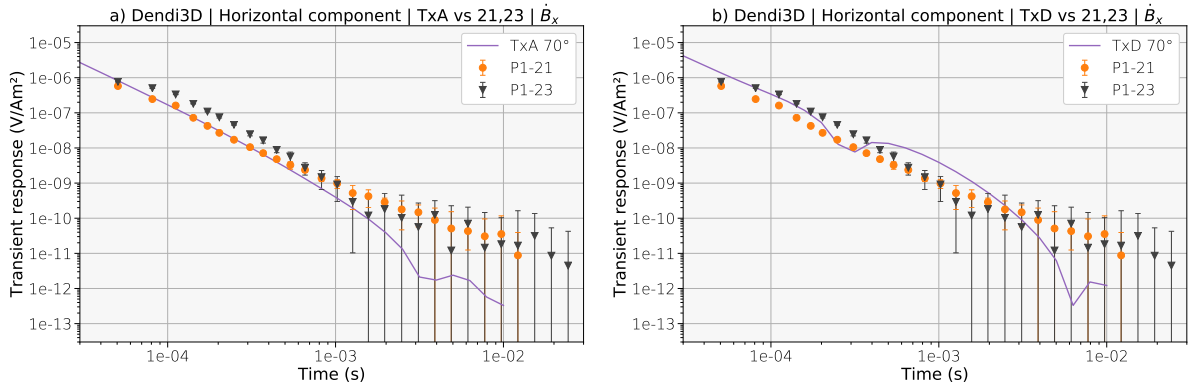

Figure 5.28.: *Synthetic $\dot{B}_x$ data from the 3D model location a) TxA and b) TxD for the 70 degree slope angle with applied topography compared to $\dot{B}_x$ field data from Lake Dendi stations P1-21 and P1-23.*

higher than the magnitude of the horizontal component when using the DEM. Without topography, it is 100 times higher than the magnitude of the horizontal component.

Taking a closer look on the $\dot{B}_x$ transients of stations TxC and TxD in Figures 5.26c and 5.26d with regards to 2D effects reveals that all transients provide two sign reversals. One at intermediate times and one at later times (excluding the very early times, i.e. the first two or three time channels).

At location TxC, the first sign reversal occurs around 50 μs for all slopes, the exact times are barely distinguishable in the chosen presentation and with a resolution of 10 samples per decade. The second sign reversal occurs around 300 μs for the 20° inclination and around 1.5 ms for the 70° inclination. Here, a clear dependency between the slope angle and the time of the second sign reversal can be derived. At location TxD, the two sign reversals are distinguishable for all slope angles and a dependency between subsurface inclination and the times of both sign reversals is evident.

The horizontal $\dot{B}_x$ field data from the Lake Dendi survey did not contain any sign reversals at all recording stations. Moreover, the $\dot{B}_x$ transients showed a similar shape and level throughout the whole profile. As an example, Figure 5.28 shows $\dot{B}_x$ field data from stations P1-21 and P1-23 (the eastern-most stations close to the caldera) together with synthetic $\dot{B}_x$ data from locations TxA and TxD from the Dendi 3D model with applied topography. As mentioned before, the field data of station P1-22 was defective and could not be used. The transient of station P1-23 contains three more time channels than P1-21 which is related to a longer acquisition time that was chosen for this station during the field work. The field data was gained in the ZeroTEM mode using a Zonge TEM/3 coil therefore no data was acquired before 5.05E-05 s.

For location TxA, the data of station P1-21 matches the synthetic data well for times between 50 μs and 500 μs. After that, the modeled data decreases faster than the field data. For location TxD, the field data can not be fitted at all due to the sign reversal. To conclude, no signature of a 2D effect based on a possible inclined subsurface crater can be found the horizontal data of Lake Dendi.

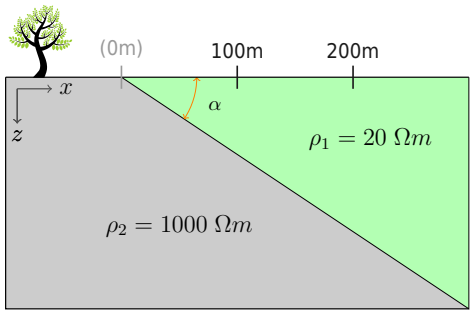

Figure 5.29: *2D Sketch of the dipping layer model consisting of a resistive lower layer with 1000 Ωm and a more conductive overburden with 20 Ωm. The angle α is varied from 10 to 75 degrees.*

5.4. Modeling a Dipping Layer

In order to investigate effects of a dipping layer on the vertical and one horizontal magnetic field component, an additional simple setting was modeled with TDcustEM. Figure 5.29 shows a 2D sketch of the model consisting of a resistive dipping layer with a 1000 Ωm resistivity and a more conductive overburden with 20 Ωm.

The angle α denotes the inclination of the dipping layer. Calculations have been made for angles of α = 10, 20, 30, 45 and 75 degrees. The transmitter was a 100 × 100 m^2 inductively coupled loop source with an injected current of 1 A.

Two central-loop locations are investigated: One with an x-direction offset of 100 m and one with an x-direction offset of 200 m. At x = 0 m, the dipping layer appears on the surface. The modeled time range was again 10^{-6} to 10^{-2} s. Although the modeling domain is 3D, the resistivity is only depending on the x- and z-direction.

The results of this study are shown in Figure 5.30. The left-hand side images contain the results of the vertical component $\dot{B}_z$ and the results of the $\dot{B}_x$ component are displayed in the images on the right-hand side.

The transients of the vertical $\dot{B}_z$ component show a clear dependency on the modeled values for α as well as an expected shift of these patterns in time when comparing the 100 m offset data to the 200 m offset data. The transients of the horizontal $\dot{B}_x$ component provide one sign reversal each, except for the 100 m offset and 10° inclination. The calculations of the $\dot{B}_x$ component suggest two things: First, the greater the inclination angle α is, the later the sign reversal occurs. Second, the smaller the inclination angle is, the greater is the magnitude of the horizontal component.

A comparison between the results of this simplified model and the results of the 3D model of Lake Dendi discussed in the last chapter shows that the sign reversal occurs significantly earlier in the present simple model and that only one sign reversal can be observed. In contrast, the 3D model of Lake Dendi produced two sign reversals for the stations TxC and TxD which are closest to the dipping subsurface layer (see Figure 5.26). The distance of TxD to the crater rim was approximately 135 m. Therefore, the dipping layer alone can not be responsible for the appearance of two sign reversals in the synthetic $\dot{B}_x$ components of the 3D Lake Dendi model. The three-dimensionality and the topography of the Lake Dendi model must account for shape and patterns of the horizontal $\dot{B}_x$ transients as well.

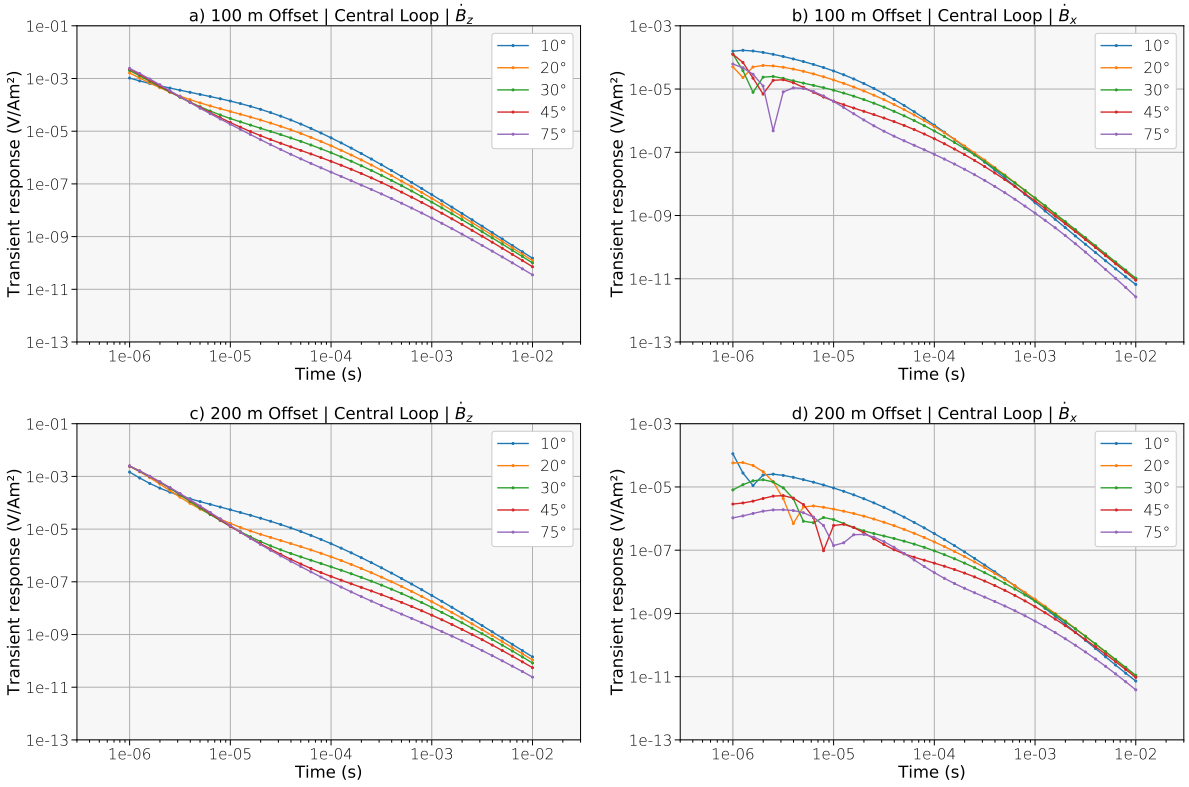

Figure 5.30.: *Vertical $\dot{B}_z$ and horizontal $\dot{B}_x$ component of the simplified dipping layer model using a central-loop TEM setup for inclinations of 10 to 75 degrees. Two locations with distances of 100 and 200 m from the outcropping resistive layer are modeled.*

CHAPTER 6

Summary and Conclusion

In the framework of the present thesis, a 3D CSEM time domain code *TDcustEM* based on the recently published open-source software custEM and the finite element toolbox FEniCS was developed. The transformation of the frequency domain data provided by custEM into the time domain is done by a Fast Hankel Transform using 80 digital filter coefficients and 10 samples per decade. With TDcustEM, it is possible to generate synthetic data using unstructured tetrahedral meshes with topography, arbitrary source and subsurface geometries as well as anisotropy. The usage of higher-order polynomials and parallel computing facilitates fast and accurate 3D time domain results. The 3D tetrahedral meshes using edge-based Nédélec finite elements are generated by the well-established mesh generator TetGen. While the present thesis concentrates on the common total E-field approach, further electromagnetic field approaches are implemented in custEM and could therefore be used with TDcustEM as well.

To ensure precision and reliability of the new algorithm, the results of several successful cross-validations for the different electric and magnetic field components and CSEM configurations were shown. These cross-validations were done for inductively coupled loop transmitters and grounded dipole sources. For homogeneous half-spaces, the results were compared to analytic solutions. For a various number of 1D layered subsurfaces, the results were validated by comparing them to the semi-analytic 1D software EMUPLUS. Subsequently, the 3D competence of TDcustEM was proven by successfully comparing its results to the finite difference algorithm SLDMEM. The applicability of the utilized SLDMEM grids and the numerical solution accuracy were proven by grid checks with EMUPLUS. The runtime of the algorithm was investigated in dependency of several parameters like the input frequency, polynomial degree, number of parallel used cores and different mesh refinements.

Long computational runtimes due to the large number of necessary frequency domain solutions are still a considerable drawback of convolutional time domain techniques. Different modeling studies regarding possible interpolation and extrapolation techniques applied on the frequency domain data were conducted. It was shown that there is a huge potential of saving runtime by reducing the number of frequencies as long as the shape of the

frequency data response is sufficiently smooth. But due to possible sign reversals in the frequency domain, depending on the subsurface model and the chosen CSEM setup, it is impossible to suggest that the computation of a certain number of samples per decade in the frequency domain is generally sufficient. A more sophisticated investigation on the behavior of the frequency data series, depending on the subsurface model and the CSEM setup, is necessary to make use of these runtime saving potentials. Especially with regard to a possible implementation of TDcustEM in a 3D inversion scheme in the future, faster runtimes are inevitable.

Regarding the Fast Hankel Transform in TDcustEM, a default set of 80 filter coefficients was implemented. The performance of this set was successfully assessed in comparison with two recently published sets of 101 and 201 filter coefficients for a loop and a dipole source transmitter. The subsurface model of this assessment was a uniform half-space and only the $\dot{H}_z$ component was investigated. A comparison of more complex geological models could provide better insights if a greater set of coefficients yields more precise results. On the other hand, a greater number of coefficients yields a longer computation time. A reduction of the utilized filter coefficients to less than 80 and therefore a smaller number of total necessary frequency solutions is not advised.

The importance of a precise receiver positioning for magnetic components was investigated. While the vertical magnetic component is quite stable regarding small deviations of the receiver position, small deviations of the horizontal components generate significant signals in the receivers. To corroborate this hypothesis, an exemplary transient of a probably shifted horizontal $\dot{B}_x$ measurement showed the same structure than synthetic $\dot{B}_x$ data with a small offset of 1 or 2 m. When horizontal magnetic components or their time derivative are going to be measured during a field survey, handheld GPS receivers with an assumed accuracy of a few meters are probably too imprecise. Horizontal B-field components are not only sensitive to a precise receiver positioning, small deviations from the transmitter loop planarity can trigger unwanted horizontal signals as well.

Synthetic studies showed that boundary conditions are not mandatory for the CSEM simulations with TDcustEM. Chosing a sufficiently large domain size with a possible extension of the mesh by a much coarser secondary tetrahedron mesh (a so-called tetrahedron boundary) yields as good results as forward modelings with Zero-Dirichlet boundary conditions. The coarse extension mesh usually increases the total number of tetrahedra by a justifiable quantity. Modeling different resistivity contrasts for simple subsurface models with two layers revealed that TDcustEM is capable of managing resistivity contrasts ratios of up to 1:50. However, further research is necessary on mesh properties when the forward calculated models are subject to sharp resistivity contrasts of 1:100 or greater.

During the process of developing and verifying the code and running a huge number of simulations, the following findings were made regarding TDcustEM. First, the usage of the polynomial degree of 2 is advised for all regular simulations. For testing purposes and for very simple models, running simulations with a polynomial degree of 1 is sufficient. Second, meshing 1D layered half-spaces is easy and straightforward with custEM and TetGen. Generating meshes with more complex 3D structures that resemble real world settings, i.e. meshes beyond simple geometries like a cube or a sphere, is nontrivial. A basic knowledge of the programming language Python and of the available meshing routines provided by custEM is essential.

As being a part of the CRC 806 - *Our Way to Europe*, the 1D and constrained inversion results regarding the TEM loop source surveys in the East African Rift Valley suggest the following: At Lake Chew Bahir, the data showed no signatures of an underlying bedrock. With estimated exploration depths of approximately 150 - 200 m, the sediment thicknesses of the basin seem to be at least 200 m, even at the western-most parts of the survey area near the lake shore. The subsurface at Chew Bahir consists of very conductive, hypersaline sediments with resistivities around 1 Ωm and less, preventing deeper exploration depths. With a significant likelihood, a sedimentary layering and a resistive bottom layer could be detected during the survey at Bisare River. Sediment thicknesses are assumed to be 100 - 150 m. The recorded data from the Dendi Lakes provided no evidence regarding a resistive bedrock layer. Only indications of a bottom layer with an increasing resistivity were detected. Sediment thicknesses in the area of the conducted survey at Lake Dendi are assumed to be at least 150 m.

An extensive 3D modeling study of the eastern parts of Lake Dendi area was performed including topography in form of a digital elevation model. A subsurface dipping crater flank with four different simulated inclinations between 20° and 70° was investigated for different loop source locations inside the sedimentary basin. The results indicate that significant 3D patterns in the vertical and horizontal transients are generated even for steep inclinations of 70° and locations adjacent to the crater rim. However, none of these patterns can be found in the two-dimensional field data set from the Dendi Lakes. Therefore, no sign of a dipping crater in the field data is evident.

Conclusively, the TEM surveys in Ethiopia provided new insights into the structure and depths of the investigated sedimentary basins. Detailed images of the resistivity distribution at Bisare River and at the Dendi Lakes were presented. At Lake Chew Bahir and at the Dendi Lakes, further geophysical research is necessary to reliably estimate sediment thicknesses. A LOTEM campaign deploying an extensive dipole transmitter with adequate transmitter/receiver distances could possibly detect a crystalline bedrock. Nevertheless, the presented geophysical results in this thesis provide valuable information for possible future drillings.

Bibliography

Andersen, W. L. (1989), A hybrid fast hankel transform algorithm for electromagnetic modeling, *Geophysics*, *54 (2)*, 263–266, doi:10.1190/1.1442650.

Ansari, S. and C. G. Farquharson (2014), 3d finite-element forward modeling of electromagnetic data using vector and scalar potentials and unstructured grids, *Geophysics*, *79 (4)*, E149–E165, doi:10.1190/geo2013-0172.1.

Auken, E. and A. V. Christiansen (2004), Layered and laterally constrained 2D inversion of resistivity data, *Geophysics*, *69*, 752–761, doi:10.1190/1.1759461.

Avdeev, D. B. (2005), Three-dimensional electromagnetic modelling and inversion from theory to application, *Surveys in Geophysics*, *26*, 767–799.

Badea, E. A., M. E. Everett, G. A. Newman and O. Biro (2001), Finite-element analysis of controlled-source electromagnetic induction using coulomb-gauged potentials, *Geophysics*, *66*, 786–799.

Börner, R.-U. (2010), Numerical Modelling in Geo-Electromagnetics: Advances and Challenges, *Surveys in Geophysics*, *31(2)*, 225–245, doi:10.1007/s10712-009-9087-x.

Börner, R.-U., O. G. Ernst and K. Spitzer (2008), Fast 3-d simulation of transient electromagnetic fields by model reduction in the frequency domain using krylov subspace projection, *Geophysical Journal International*, *173*, 766–780, doi:10.1111/j.1365-246X.2008.03750.x.

Börner, R.-U., O. G. Ernst and S. Güttel (2015), Three-dimensional transient electromagnetic modeling using rational krylov methods, *Geophysical Journal International*, *202*, 2025–2043, doi:10.1093/gji/ggv224.

Cai, H., X. Hu, B. Xiong, E. Auken, M. Han and J. Li (2017), Finite element time domain modeling of controlled-source electromagnetic data with a hybrid boundary condition, *Journal of Applied Geophysics*, *145*, 133–143, doi:10.1016/j.jappgeo.2017.08.005.

Castillo-Reyes, O., J. de la Puente and J. M. Cela (2018), Petgem: A parallel code for 3d csem forward modeling using edge finite elements, *Computers and Geosciences*, *119*, 123–136, doi:10.1016/j.cageo.2018.07.005.

Christensen, N. B. (1990), Optimized fast hankel transform filters, *Geophysical Prospecting*, *38*, 545–568, doi:10.1111/j.1365-2478.1990.tb01861.x.

Christiansen, A. V. and E. Auken (2012), A global measure for depth of investigation, *Geophysics*, *77*, WB171–WB177, doi:10.1190/GEO2011-0393.1.

Coggon, J. H. (1971), Electromagnetic and electrical modeling by the finite element method, *Geophysics*, *36*, 132–155, doi:10.1190/1.1440151.

Commer, M. and G. Newman (2004), A parallel finite-difference approach for 3d transient electromagnetic modeling with galvanic sources, *Geophysics*, *69*, 1192–1202, doi:10.1190/1.1801936.

Druskin, V. L. and L. A. Knizhnerman (1988), A spectral semi-discrete method for the numerical solution of 3D nonstationary problems in electrical prospecting, *Physics of the Solid Earth*, *24*, 641–648.

Druskin, V. L. and L. A. Knizhnerman (1994), Spectral approach to solving threedimensional Maxwell's diffusion equations in the time and frequency domains, *Radio Science*, *29 (4)*, 641–648, doi:10.1029/94RS00747.

Druskin, V. L. and L. A. Knizhnerman (1999), New spectral Lanczos decomposition method for induction modeling in arbitrary 3-D geometry, *Geophysics*, *64 (3)*, 701–706, doi:10.1190/1.1444579.

Foerster, V. et al. (2012), Climatic change recorded in the sediments of the Chew Bahir basin, southern Ethiopia, during the last 45,000 years, *Quaternary International*, *274*, 25–37, doi:10.1016/j.quaint.2012.06.028.

Ghosh, D. P. (1971), The application of linear filter theory to the direct interpretation of geoelectrical resistivity sounding measurements, *Geophysical Prospecting*, *19*, 192–217, doi:10.1111/j.1365-2478.1971 .tb00593.x.

Gockenbach, M. S. (2006), *Understanding and Implementing the Finite Element Method*, Society of Industrial and Applied Mathematics, Philadelphia.

Grayver, A. and T. V. Kolev (2015), Large-scale 3D geoelectromagnetic modeling using parallel adaptive high-order finite element method, *Geophysics*, *80 (6)*, E277–E291, doi:10.1190/GEO2015-0013.16.

Grayver, A., K. Tietze and O. Ritter (2013), RMS – Rather Meaningless Simplification?, presented at the 25th Schmucker-Weidelt-Kolloquium, Kirchhundem-Rahrbach, Germany, 23rd – 27th September 2013.

Gupta, P., A. Raiche and F. Sugeng (1989), Three-dimensional time-domain electromagnetic modeling using a compact finite-element frequency-stepping method, *Geophysical Journal International*, *96*, 457–468, doi:10.1111/j.1365-246X.1989.tb06007.x.

Haber, E., D. W. Oldenburg and R. Shekhtman (2007), Inversion of time domain three-dimensional electromagnetic data, *Geophysical Journal International*, *171*, 550–564, doi:10.1111/j.1365-246X.2007.03365.x.

Hohmann, G. W. (1975), Three-dimensional induced polarization and electromagnetic modeling, *Geophysics*, *40 (2)*, 309–324, doi:10.1190/1.1440527.

Hönig, M. (2002), Entwicklung und Anwendung von Auswertealgorithmen für die Induzierte Polarisation im Zeitbereich in bis zu drei Dimensionen, Ph.D. thesis, University of Cologne, Germany.

Hördt, A., V. L. Druskin, L. A. Knizhnerman and K.-M. Strack (1992), Interpretation of 3-D effects in long-offset transient electromagnetic (LOTEM) soundings in the Münsterland, *Geophysics*, *57 (9)*, 1127–1137, doi:10.1190/1.1443327.

Hördt, A., S. Dautel, B. Tezkan and H. Thern (2000), Interpretation of long-offset transient electromagnetic data from the Odenwald area, Germany, using two-dimensional modelling, *Geophysical Journal International*, *140 (3)*, 577–586, doi:10.1046/j.1365-246X.2000.00047.x.

Jahandari, H., S. Ansari and C. G. Farquharson (2017), Comparison between staggered grid finite-volume and edge-based finite-element modeling of geophysical electromagnetic data on unstructured grids, *Journal of Applied Geophysics*, *138*, 185–197, doi:10.1016/j.jappgeo.2017.01.016.

Janser, S. (2017), Development of an one-dimensional forward and inverse algorithm for SQUID and coil TDEM data, M.Sc. thesis, University of Cologne, Germany.

Jin, J.-M. (2010), *Theory and Computation of Electromagnetic Fields*, IEEE Press, Piscataway, New Jersey.

Jin, J.-M. (2014), *The Finite Element Method in Electrodynamics*, Wiley, 3rd edition, Hoboken, New Jersey.

Johansen, H. K. and K. Sørensen (1979), Fast Hankel transforms, *27*, 876–901, doi:10.1111/j.1365-2478.1979.tb01005.x.

Jupp, D. L. B. and K. Vozoff (1975), Stable Iterative Methods for the Inversion of Geophysical Data, *Geophysical Journal of the Royal Astronomical Society*, *42*, 957–976.

Kearey, P., M. Brooks and I. Hill (2002), *An introduction to geophysical exploration*, 3. ed., Blackwell Scientific Publications, Oxford.

Key, K. (2012), Is the fast Hankel transform faster than quadrature?, *Geophysics*, *77 (3)*, F21–F30, doi:10.1190/GEO2011-0237.1.

Li, J., C. G. Farquharson and X. Hu (2017), 3D vector finite-element electromagnetic forward modeling for large loop sources using a total-field algorithm and unstructured tetrahedral grids, *Geophysics*, *82 (1)*, E1–E16, doi:10.1190/geo2016-0004.1.

Li, J., X. L. C. G. Farquharson and X. Hu (2018), A finite-element time-domain forward solver for electromagnetic methods with complex-shaped loop sources, *Geophysics*, *83 (3)*, E117–E132, doi:10.1190/GEO2017-0216.1.

Lippert, K. (2015), Detektion eines submarinen Aquifers vor der Kuste Israels mittels mariner Long Offset Transient-elektromagnetischer Messung, Ph.D. thesis, University of Cologne, Germany.

Livelybrooks, D. (1993), A multidimensional electromagnetic finite element model, *Geophysical Journal International*, *114*, 443–458, doi:10.1111/j.1365-246X.1993.tb06978.x.

Logg, A., K.-A. Mardal and G. Wells (2012), *Automated solution of different equations by the finite element method: The FEniCS book*, Springer, Berlin.

Mackie, R. L., T. R. Madden and P. E. Wannamaker (1993), Three-dimensional magnetotelluric modeling using difference equations—theory and comparisons to integral equation solutions, *Geophysics*, *58 (2)*, 215–226, doi:10.1190/1.1443407.

Maxwell, J. C. (1873), *A Treatise on electricity and Magnetism*, Oxford University Press, Oxford.

Meju, M. A. (1995), Simple effective resistivity-depth transformations for infield or real-time data processing, *Computers and Geosciences*, *21*, 985–992, doi:10.1016/0098-3004(95)00035-7.

Mohsen, A. A. and E. A. Hashish (1994), The fast Hankel transform, *Geophysical Prospecting*, *42*, 131–139, doi:10.1111/j.1365-2478.1994.tb00202.x.

Monk, P. (2003), *Finite Element Methods for Maxwell's Equations*, Oxford University Press Inc., New York.

Mulder, W. A., M. Wirianto and E. C. Slob (2008), Time-domain modeling of electromagnetic diffusion with a frequency-domain code, *Geophysics*, *73 (1)*, F1–F8, doi:10.1190/1.2799093.

Nédélec, J. C. (1980), Mixed finite elements in R3, *Numerische Mathematik*, *35 (3)*, 315–341, doi:10.1007/BF01396415.

Nédélec, J. C. (1986), A new family of mixed finite elements in R3, *Numerische Mathematik*, *50 (1)*, 57–81, doi:10.1007/BF01389668.

Newman, G. A. and D. L. Alumbaugh (1995), Frequency-domain modeling of airborne electromagnetic responses using staggered finite differences, *Geophysical Prospecting*, *43*, 1021–1042, doi:10.1111/j.1365-2478.1995.tb00294.x.

Newman, G. A., G. W. Hohmann and W. L. Anderson (1986), Transient electromagnetic response of a three-dimensional body in a layered earth, *Geophysics*, *51 (8)*, 1608–1627, doi:10.1190/1.1442212.

Pridmore, D. F., G. W. Hohmann, S. H. Ward and W. R. Still (1981), An investigation of finite-element modeling for electrical and electromagnetic data in three dimensions, *Geophysics*, *46*, 1009–1024, doi:10.1190/1.1441239.

Puzyrev, V., J. Koldan, J. de la Puente, G. Houzeaux, M. Vázquez and J. M. Cela (2013), A parallel finite-element method for three-dimensional controlled-source electromagnetic forward modeling, *Geophysical Journal International*, *193*, 678–693, doi:10.1093/gji/ggt027.

Raiche, A. P. (1974), An Integral Equation Approach to Three-Dimensional Modelling, *Geophysical Journal International*, *36 (2)*, 363–376, doi:10.1111/j.1365-246X.1974.tb03645.x.

Rochlitz, R., M. Queitsch, P. Yogeshwar, T. Günther, A. Chwala, S. Janser, N. Kukowski and R. Stolz (2018), Capability of low-temperature squid for transient electromagnetics under anthropogenic noise conditions, *Geophysics*, *83 (6)*, E371–E383, doi:10.1190/GEO2017-0582.1.

Rochlitz, R., N. Skibbe and T. Günther (2019), custEM: Customizable finite-element simulation of complex controlled-source electromagnetic data, *Geophysics*, *84 (2)*, 1–17, doi:10.1190/GEO2018-0208.1.

Rylander, T., A. Bondeson and P. Ingelström (2013), *Computational Electromagnetics*, Springer, New York, doi:10.1007/978-1-4614-5351-2.

Rätz, S. (2000), Ein dreidimensionales Finite Elemente Programm zur Simulation elektromagetischer Oberflächen und Bohrlochverfahren, Ph.D. thesis, Institut für Geophysik und Meteorologie, Universität zu Köln, Cologne, Germany.

Rücker, C., T. Günther and F. Wagner (2017), pyGIMLi: An open-source library for modeling and inversion in geophysics, *Computers and Geosciences*, *109*, 106–123, doi:10.1016/j.cageo.2017.07.011.

Schaumann, G. (2001), Transientenelektromagnetische Messungen auf Mülldeponien - Untersuchung des Einflusses von 3D-Leitfähigkeitsvariationen und 1D-frequenzabhängiger Polarisierbarkeit, Ph.D. thesis, University of Braunschweig, Germany.

Scholl, C. (2005), The influence of multidimensional structures on the interpretation of LOTEM data with one-dimensional models and the application to data from Israel, Ph.D. thesis, University of Cologne, Germany.

Schwarzbach, C., R.-U. Börner and K. Spitzer (2011), Three-dimensional adaptive higher order finite element simulation for geo-electromagnetics: A marine CSEM example, *Geophysical Journal International*, *187*, doi:10.1111/j.1365-246X.2011.05127.x.

Seidel, M. and B. Tezkan (2017), 1D Cole-Cole inversion of TEM transients influenced by induced polarization, *Journal of Applied Geophysics*, *138*, 220–232, doi:10.1016/j.jappgeo.2017.01.011.

Si, H. (2015), TetGen, a Delaunay-based quality tetrahedral mesh generator, *ACM Transactions on Mathematical Software (TOMS)*, *41 (2)*, doi:10.1145/2629697.

Spies, B. R. (1989), Depth of Investigation in Electromagnetic Sounding Methods, *Geophysics*, *54*, 872–888.

Spies, B. R. and F. C. Frischknecht (1991), Electromagnetic Sounding, in *Electromagnetic Methods in Applied Geophysics*, 2, chap. 5, Society of Exploration Geophysicists.

Sugeng, F. (1998), Modelling the 3D TDEM response using the 3D full-domain finite-element method based on the hexahedral edge-element technique, *Exploration Geophysics*, *29*, 615–619, doi:10.1071/EG998615.

Um, E. S., J. M. Harris and D. L. Alumbaugh (2010), 3D time-domain simulation of electromagnetic diffusion phenomena: A finite-element electric-field approach, *Geophysics*, *75 (4)*, 115–126, doi:10.1190/1.3473694.

Um, E. S., J. M. Harris and D. L. Alumbaugh (2012), An iterative finite element time-domain method for simulating three-dimensional electromagnetic diffusion in earth, *Geophysical Journal International*, *190*, 871–886, doi:10.1111/j.1365-246X.2012.05540.x.

Viezzoli, A., A. V. Christiansen, E. Auken and K. Sørensen (2008), Quasi-3D modeling of airborne TEM data by spatially constrained inversion, *Geophysics*, *73*, F105–F113, doi:10.1190/1.2895521.

Wagner, B., V. Wennrich, F. Viehberg, A. Junginger, A. Kolvenbach, J. Rethemeyer, F. Schaebitz and G. Schmiedle (2018), Holocene rainfall runoff in the central Ethiopian highlands and evolution of the River Nile drainage system as revealed from a sediment record from Lake Dendi, *Global and Planetary Change*, *163*, 29–43, doi:10.1016/j.gloplacha.2018.02.003.

Wang, T. and G. W. Hohmann (1993), A finite-difference, time-domain solution for three-dimensional electromagnetic modeling, *Geophysics*, *58*, 797–809, doi:10.1190/1.1443465.

Ward, S. H. and G. W. Hohmann (1991), Time Domain Electromagnetic Prospecting Methods, in *Electromagnetic Theory for Geophysical Exploration*, vol. 1, M. N. Nabighian ed., chap. 4, pp. 131–311, Society of Exploration Geophysicists.

Weidelt, P. (1975), Electromagnetic Induction in Three-Dimensional Structures, *J. Geophys.*, *41*, 85–109.

Weidelt, P. (1986), Einführung in die elektromagnetische Tiefenforschung, lecture notes.

Werthmüller, D. (2017), An open-source full 3D electromagnetic modeler for 1D VTI media in Python: empymod, *Geophysics*, *82*, WB9–WB19, doi:10.1190/GEO2016-0626.1.

Yee, K. S. (1966), Numerical Solutions of Initial Boundary Problems Involving Maxwell's Equations in Isotropic Media, *IEEE Transactions on Antennas and Propagation*, *14*, 302–309, doi:10.1109/TAP.1966.1138693.

Yogeshwar, P. (2014), A resistivity-depth model of the central Azraq basin area, Jordan: 2D forward and inverse modeling of time domain electromagnetic data, Ph.D. thesis, University of Cologne, Germany.

Yogeshwar, P. and B. Tezkan (2017), Two-dimensional basement modeling of central loop transient electromagnetic data from the central Azraq basin area, Jordan, *Journal of Applied Geophysics*, *136*, 198–210, doi:10.1016/j.jappgeo.2016.11.001.

Zhao, Y., Z.-Q. Zhu, G.-Y. Lu and B. Han (2018), The optimal digital filters of sine and cosine transforms for geophysical transient electromagnetic method, *Journal of Applied Geophysics*, *150*, 267–277, doi:10.1016/j.jappgeo.2018.01.008.

Zinaye, B. (2014), Geological and Geomorphological Characterization of The Dendi Caldera, West Central Ethiopia: Implications for Paleo-Environmental Reconstruction Using Lake Sediment Cores, M.Sc. thesis, University of Addis Ababa, Ethiopia.

Zohdi, T. I. (2015), *A Finite Element Primer for Beginners*, Springer, Cham (u.a.).

Zonge (2002), *GDP-32 II Multifunction Receiver Operation Manual*, Zonge Engineering and Research Organization.

A. 1D Inversion Results from Ethiopia

1D inversion results of the TEM surveys in Ethiopia.

A.1. Chew Bahir

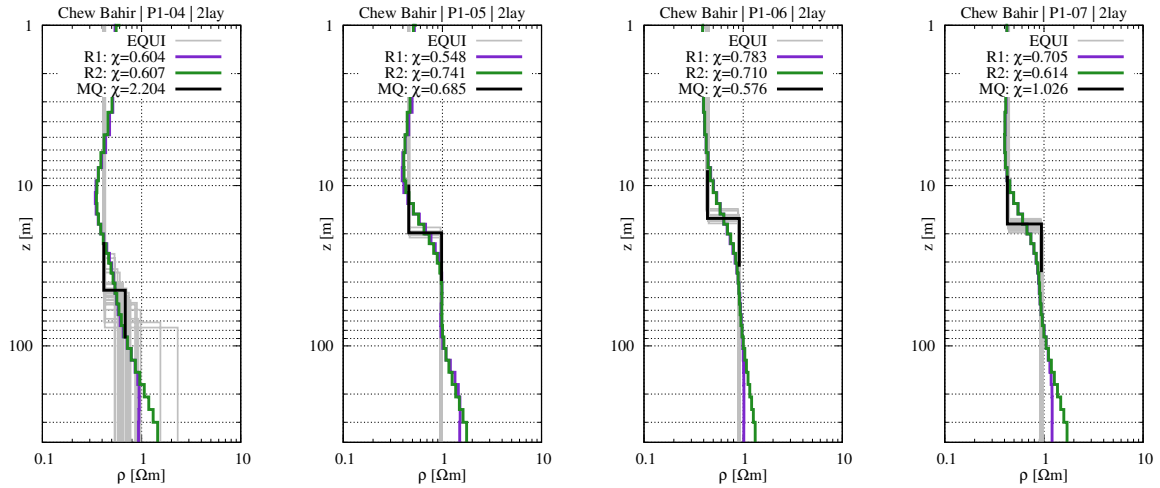

Figure A.1.: *1D inversion results of Chew Bahir profile P1 stations 4 - 7.*

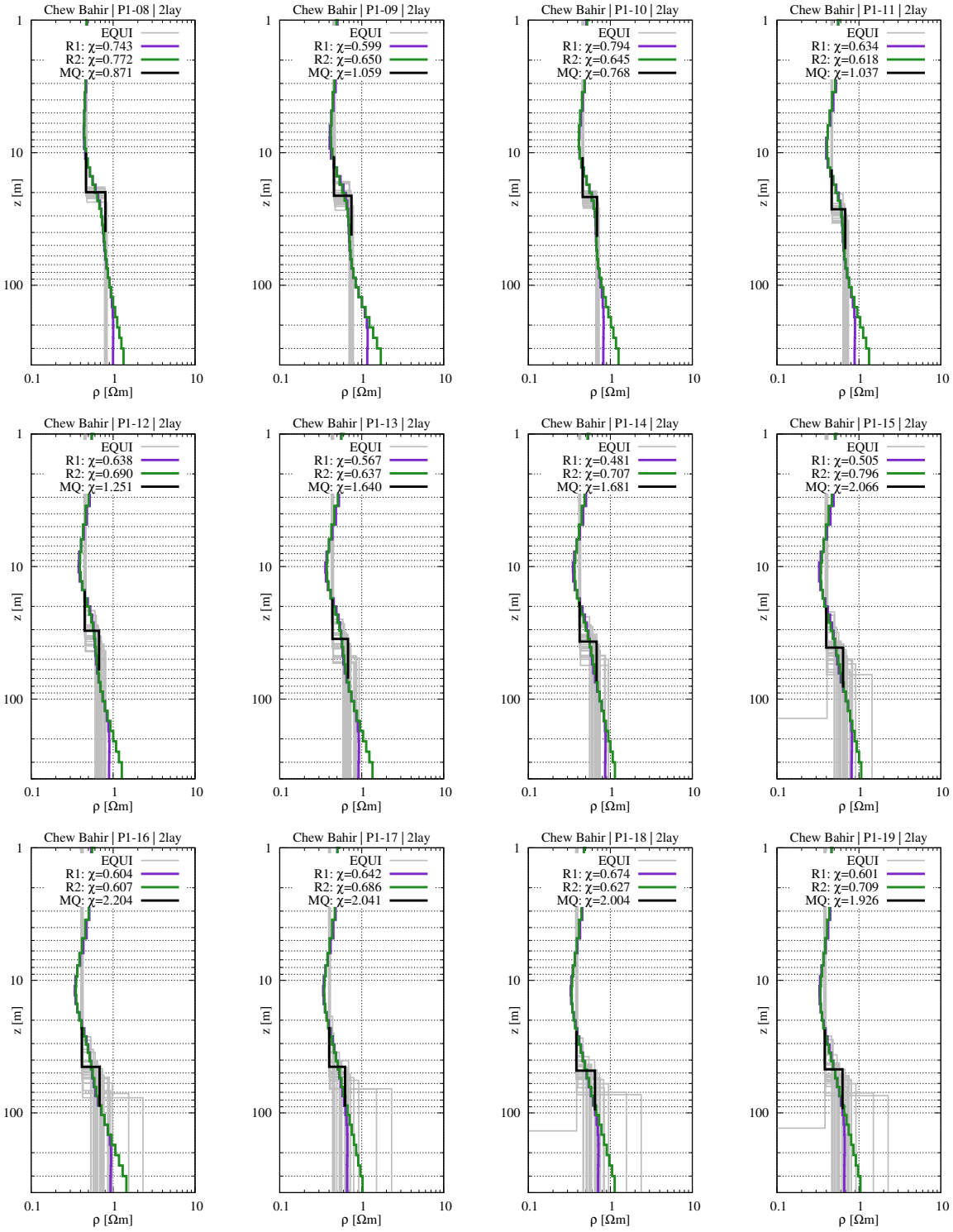

Figure A.2.: *1D inversion results of Chew Bahir profile P1 stations 8 - 19.*

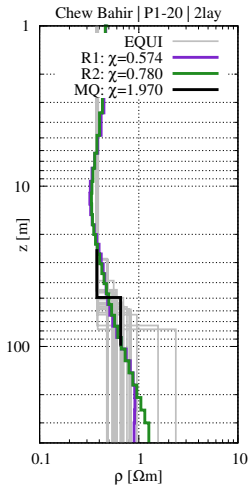

Figure A.3.: *1D inversion results of Chew Bahir profile P1 station 20.*

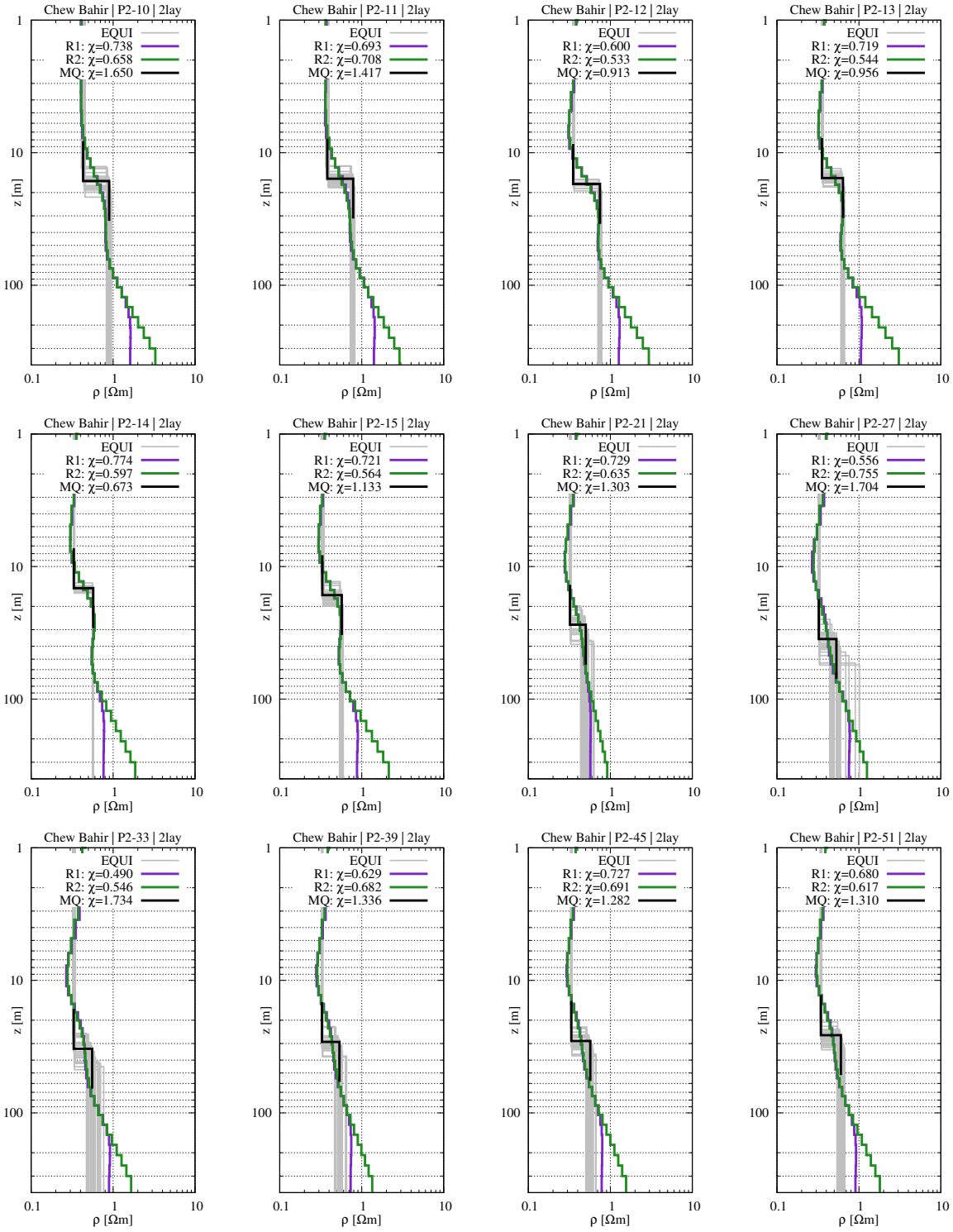

Figure A.4.: *1D inversion results of Chew Bahir profile P2 stations 10 - 51.*

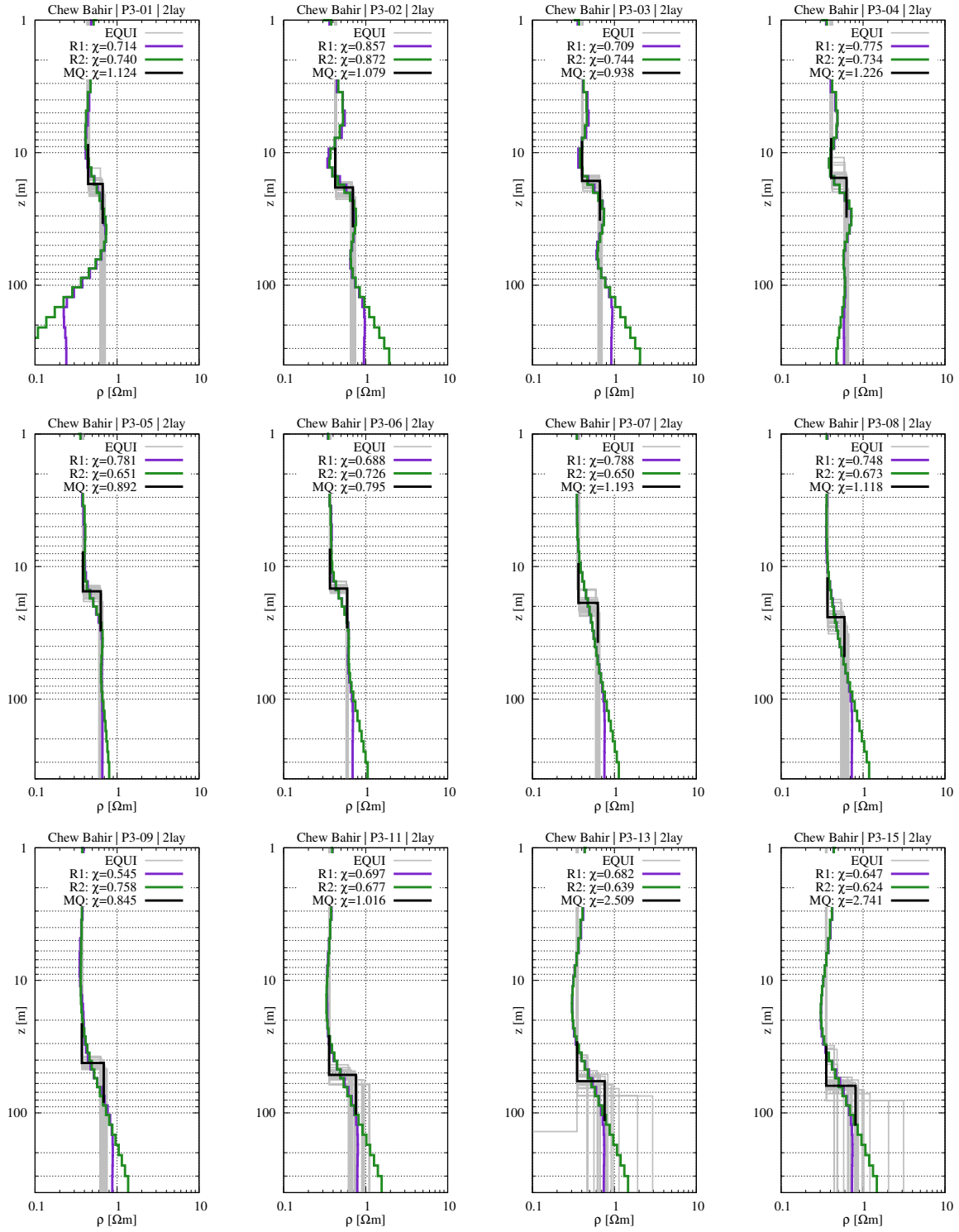

Figure A.5.: *1D inversion results of Chew Bahir profile P3 stations 1 - 15.*

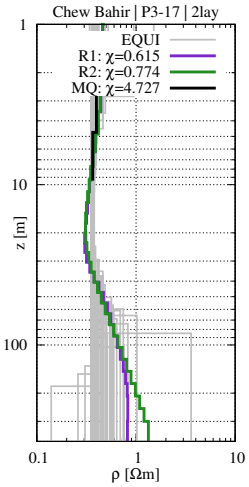

Figure A.6.: *1D inversion results of Chew Bahir profile P3 station 17.*

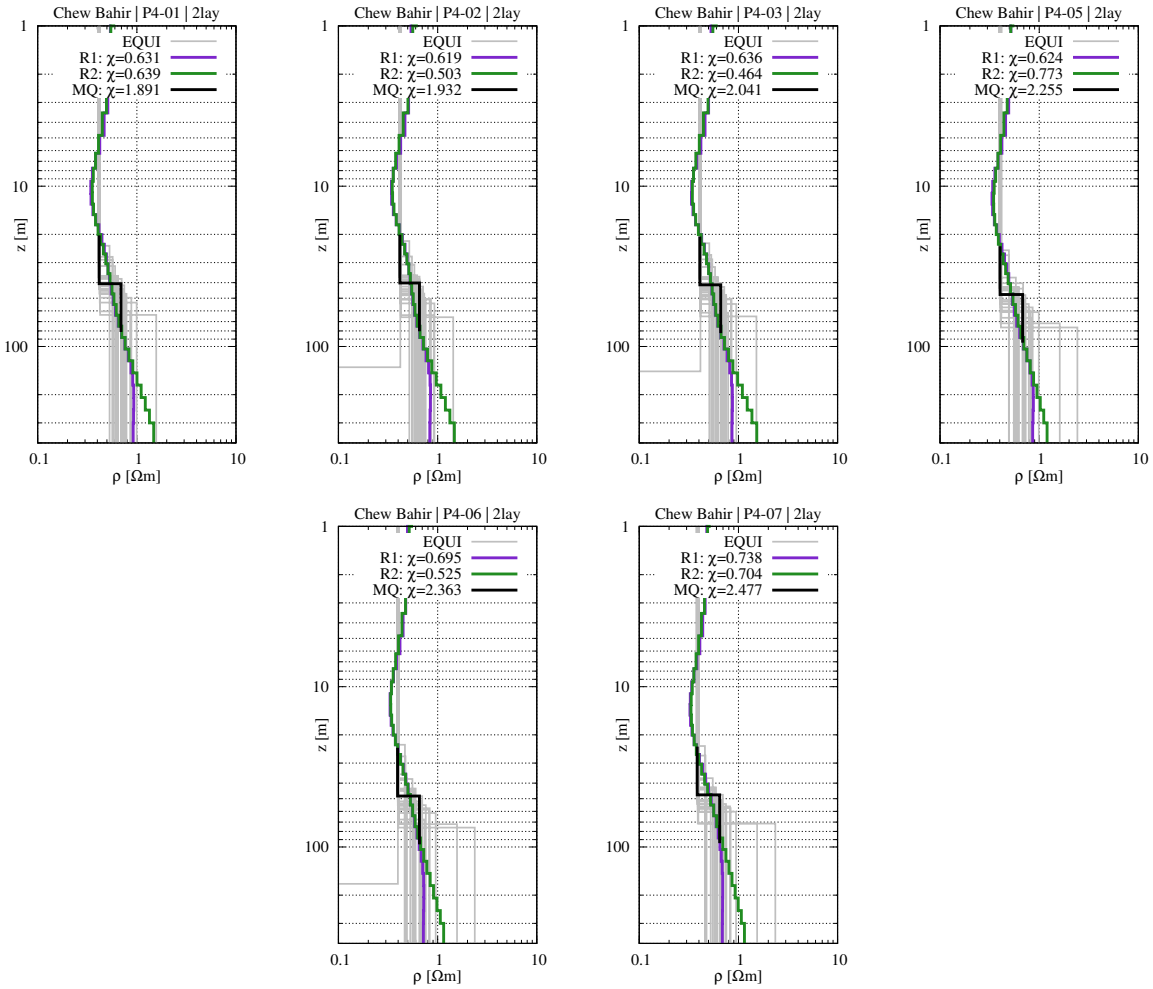

Figure A.7.: *1D inversion results of Chew Bahir profile P4 stations 1 - 7.*

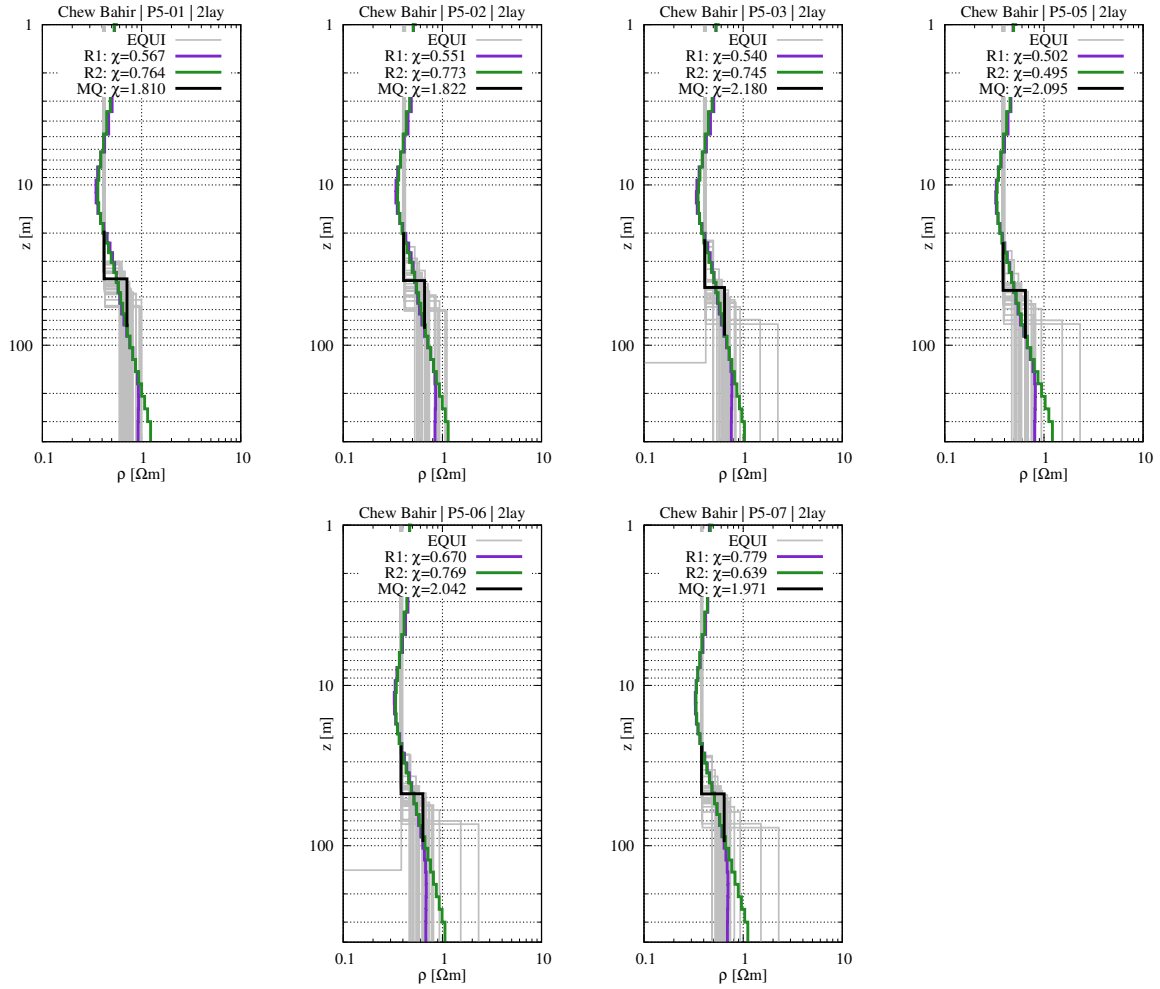

Figure A.8.: *1D inversion results of Chew Bahir profile P5 stations 1 - 7.*

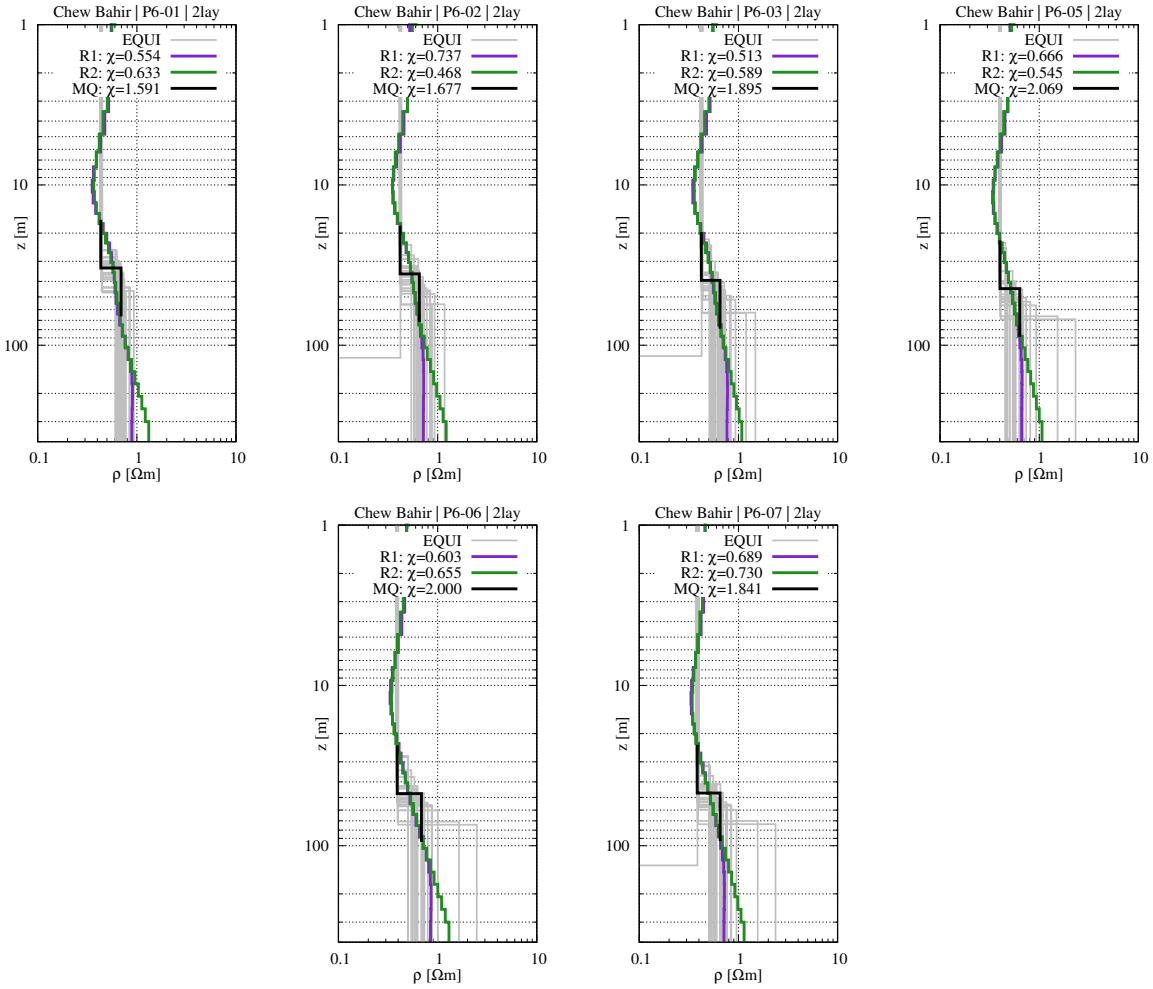

Figure A.9.: *1D inversion results of Chew Bahir profile P6 stations 1 - 7.*

A.2. Bisare River

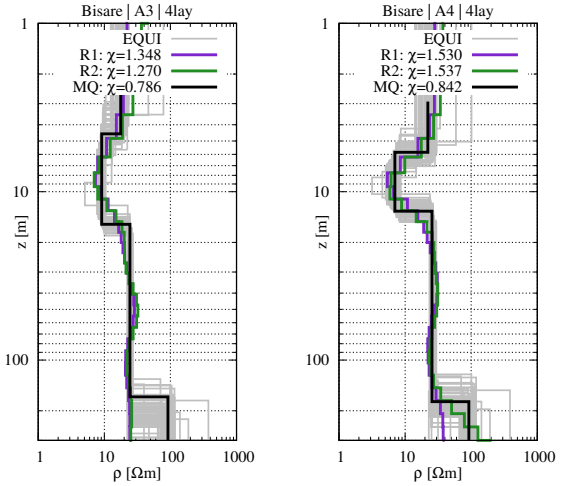

Figure A.10.: *1D inversion results of Bisare River profile A stations 3 - 4.*

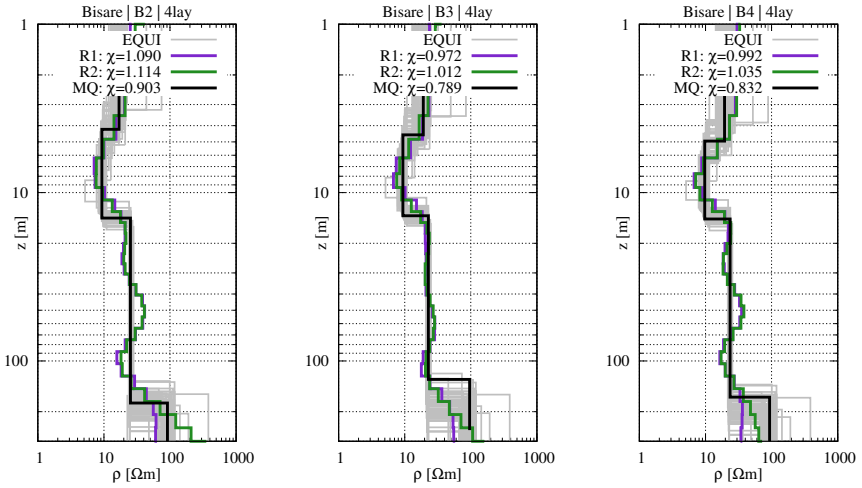

Figure A.11.: *1D inversion results of Bisare River profile B stations 2 - 4.*

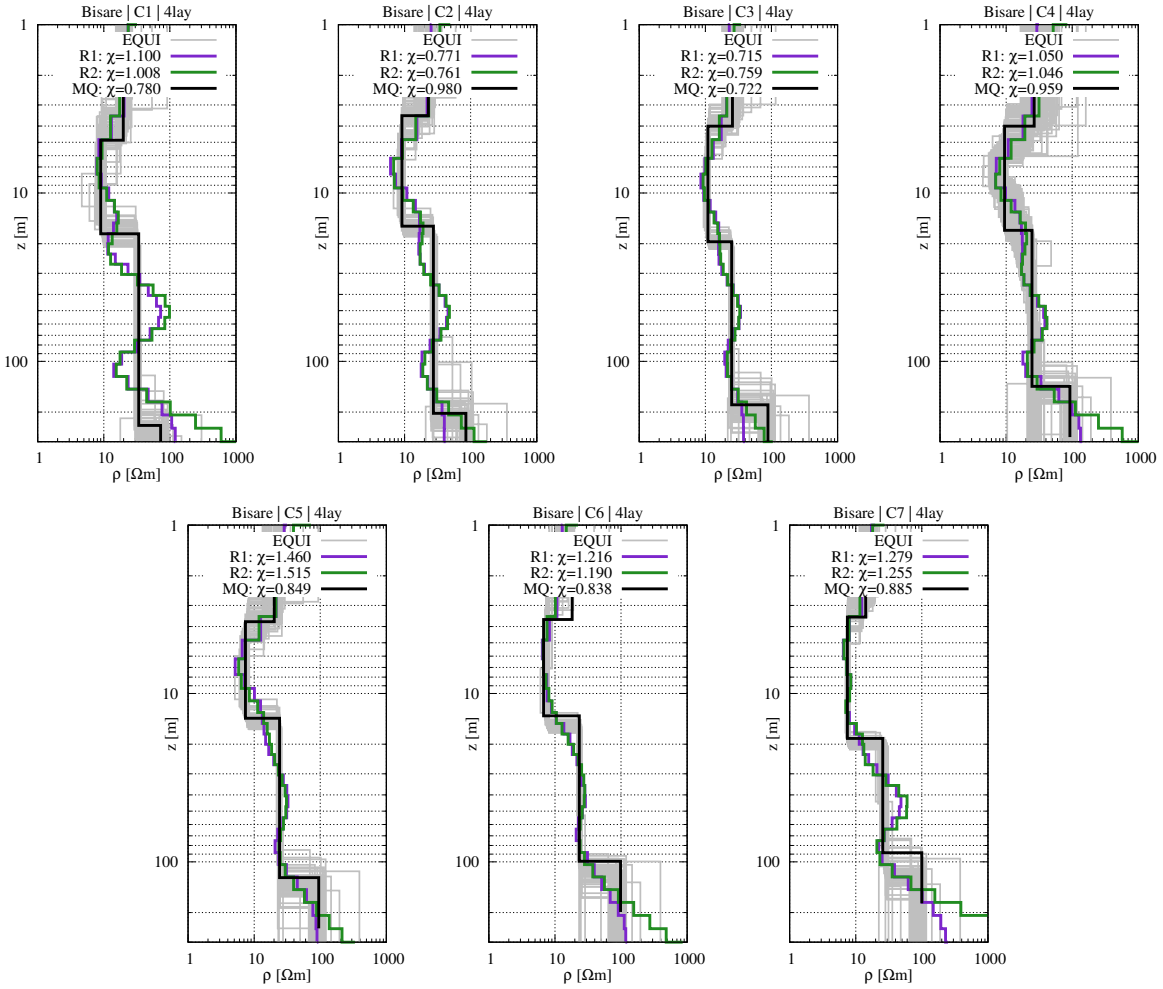

Figure A.12.: *1D inversion results of Bisare River profile C stations 1 - 7.*

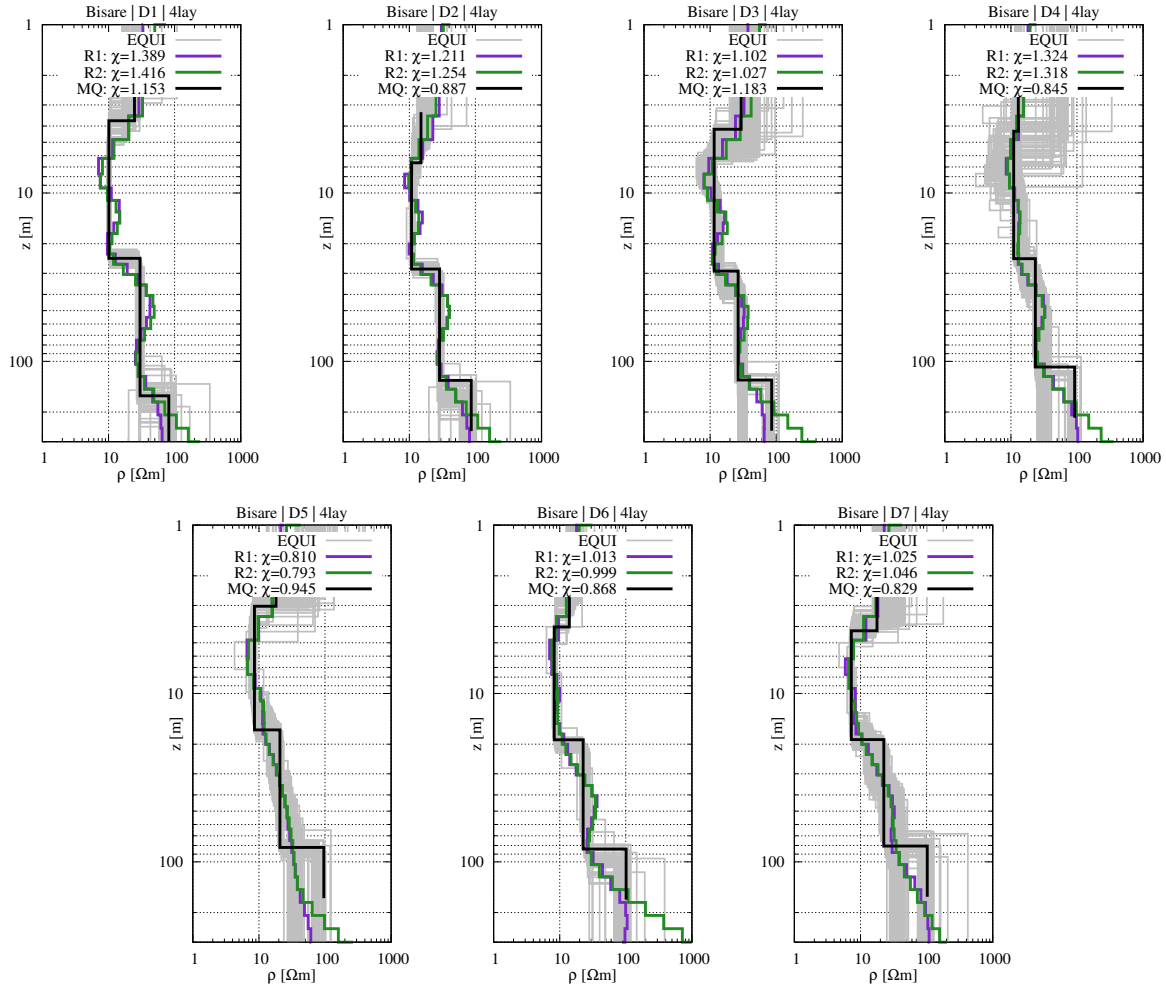

Figure A.13.: *1D inversion results of Bisare River profile D stations 1 - 7.*

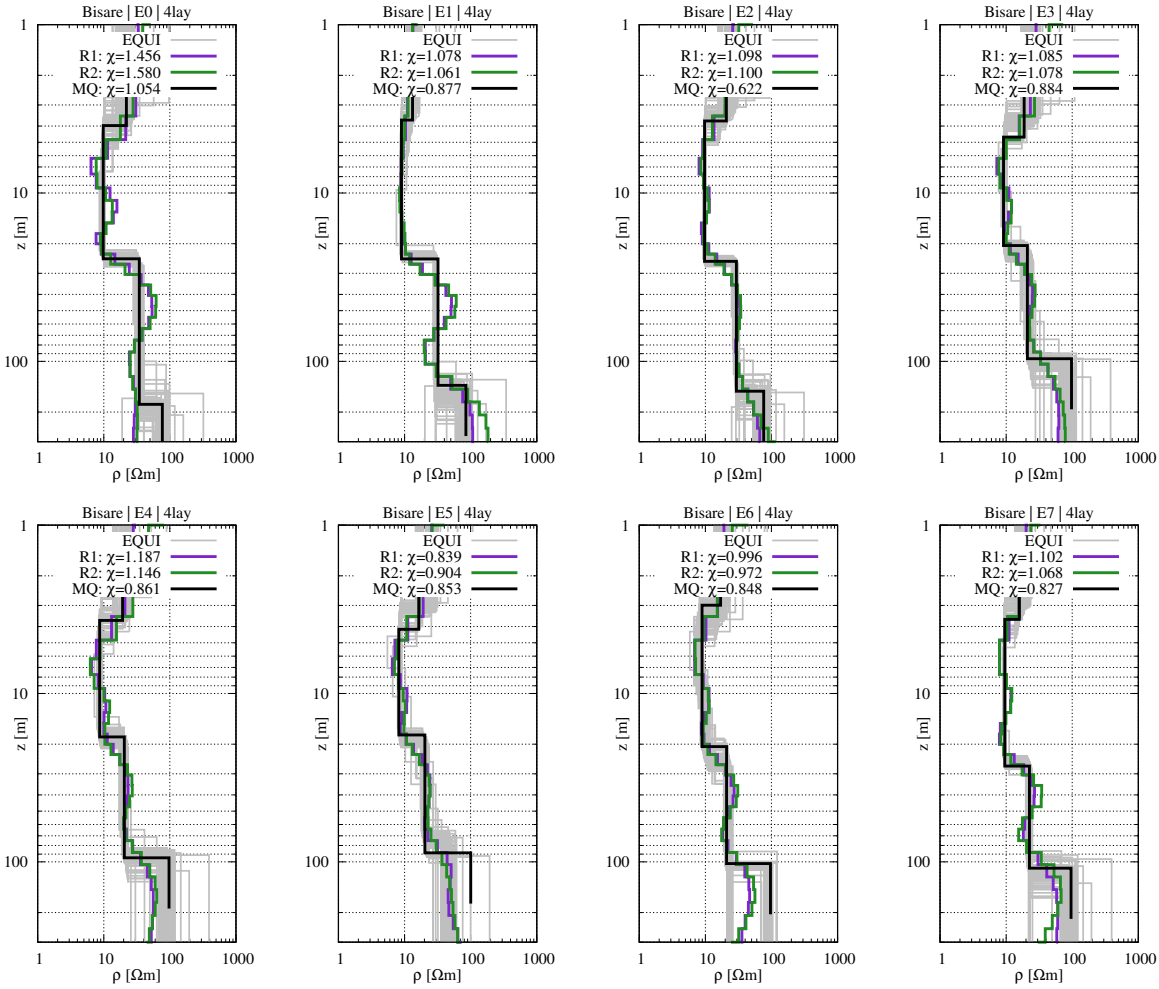

Figure A.14.: *1D inversion results of Bisare River profile E stations 0 - 7.*

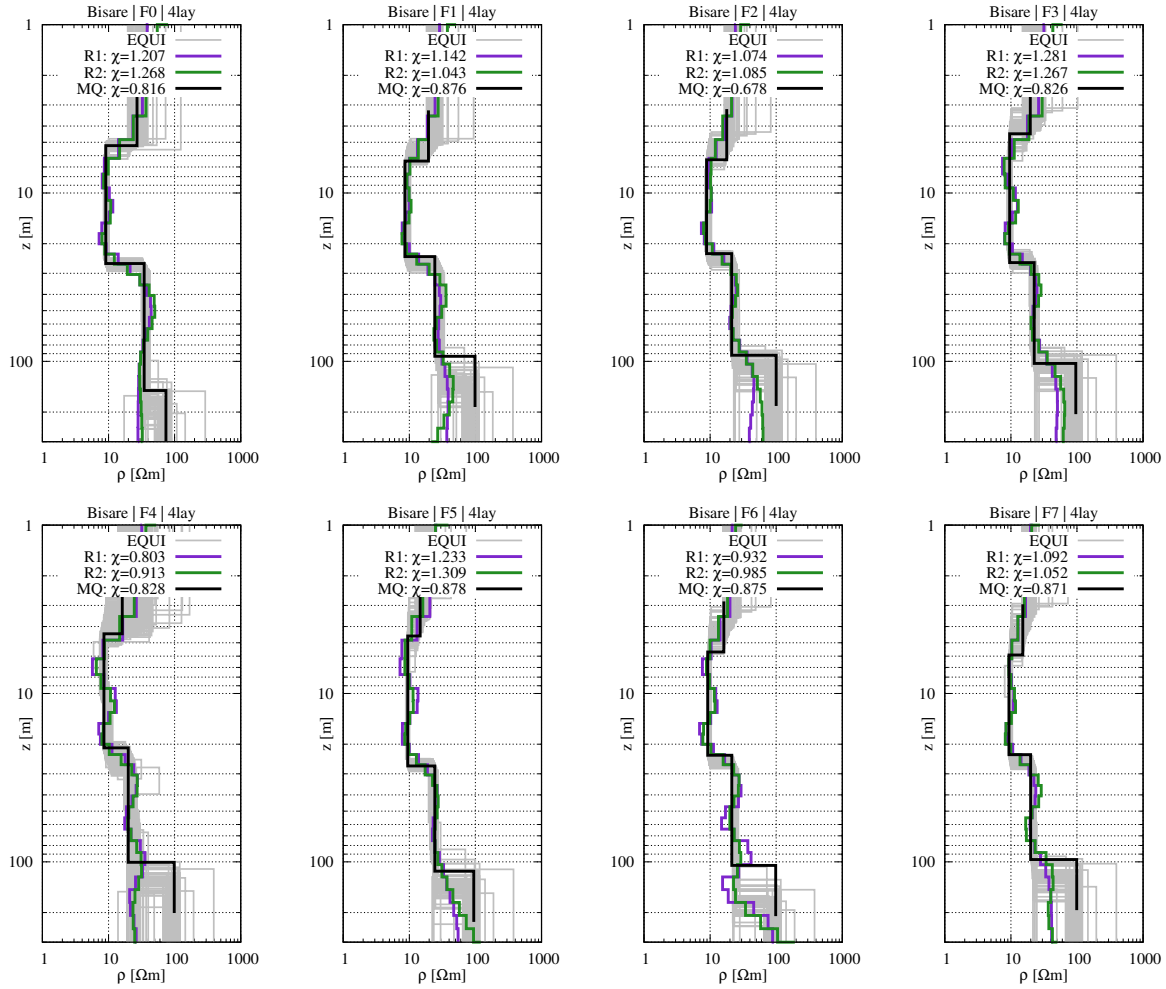

Figure A.15.: *1D inversion results of Bisare River profile F stations 0 - 7.*

A.3. Dendi Lakes

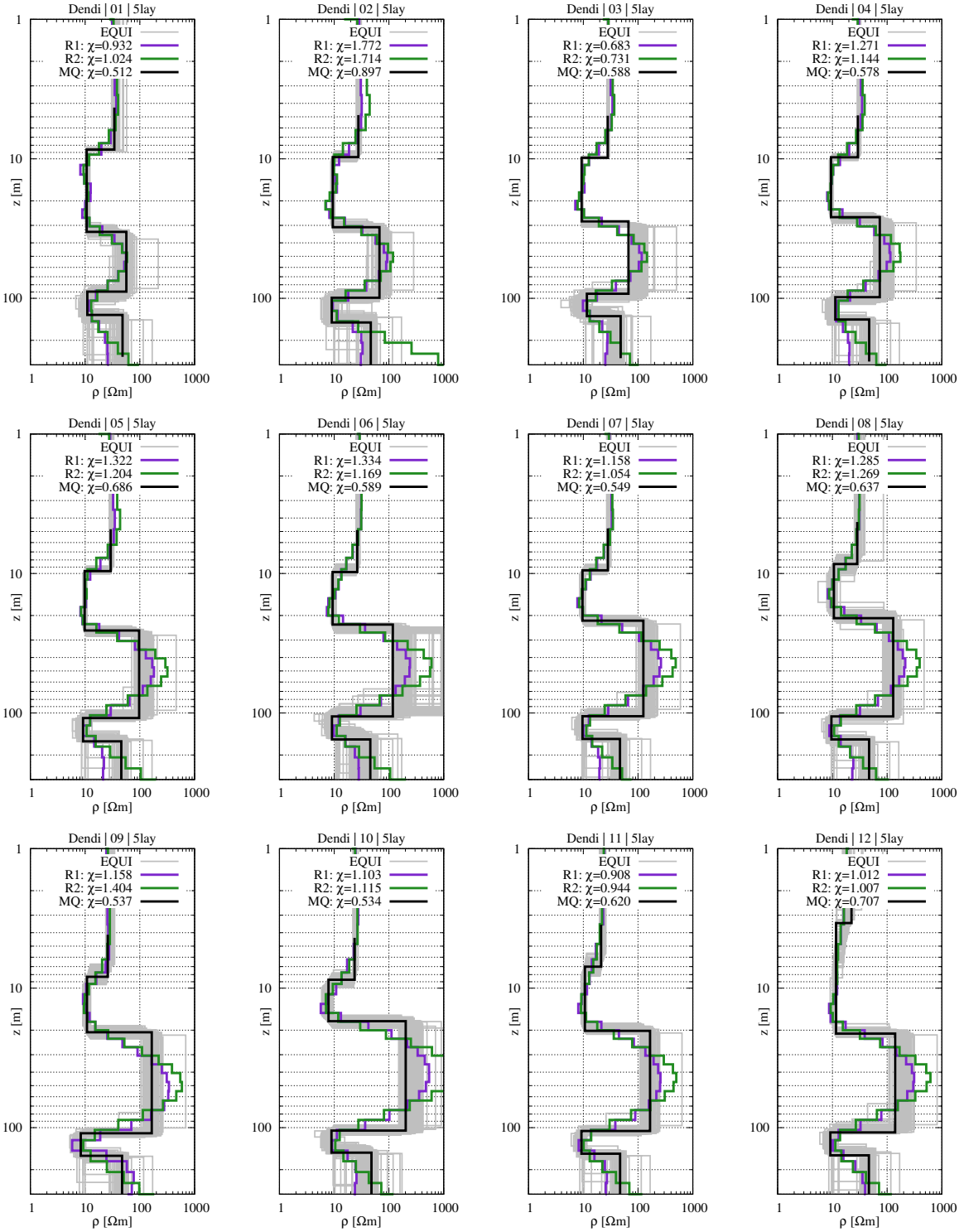

Figure A.16.: *1D inversion results of Lake Dendi profile P1 stations 1 - 12.*

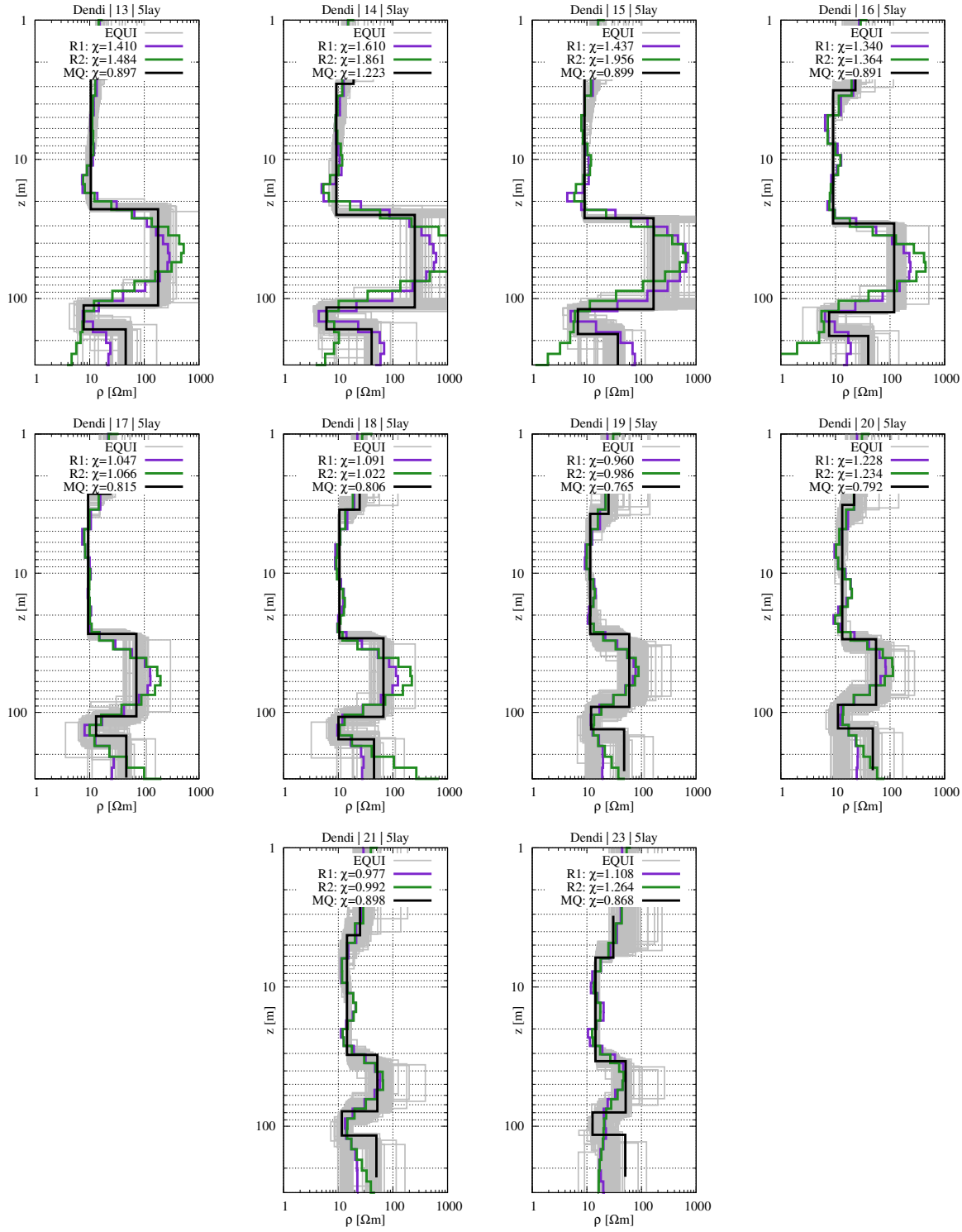

Figure A.17.: *1D inversion results of Lake Dendi profile P1 stations 13 - 23.*

B. SCI Inversion Results from Ethiopia

SCI inversion results from Bisare River.

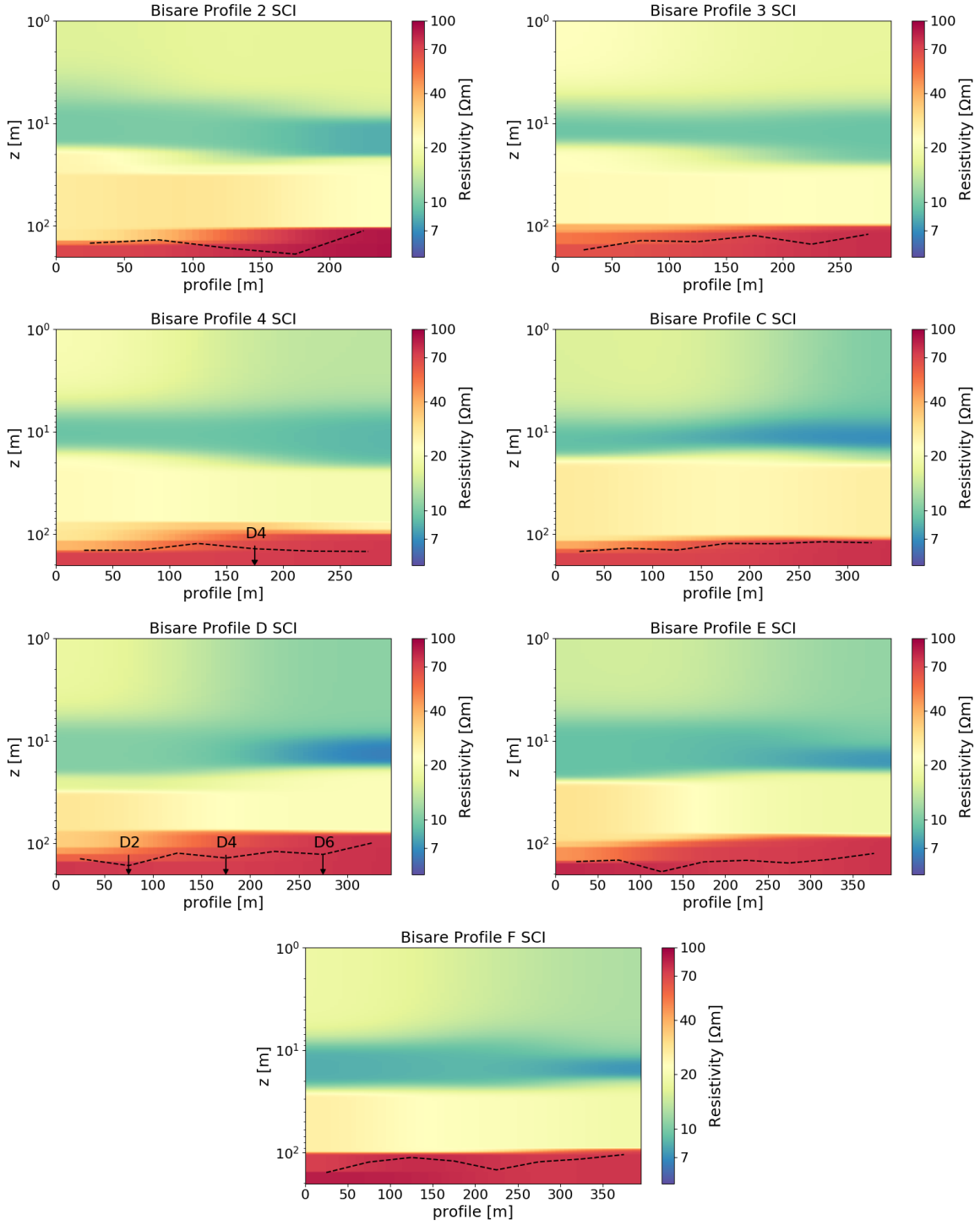

Figure B.1.: *SCI inversion results of all profiles at Bisare River.*

C. Survey Images from Ethiopia

C.1. Chew Bahir

Figure C.1.: *Images from the survey at Chew Bahir.*

Figure C.2.: *Images from the survey at Chew Bahir.*

C.2. Bisare River

Figure C.3.: *Images from the survey at Bisare River.*

C.3. Dendi Lakes

Figure C.4.: *Images from the survey at Lake Dendi.*

Acknowledgements

Finally, I would like to thank

- Prof. Dr. Bülent Tezkan for the supervision of this thesis and for all the support over the last years. I am deeply grateful for the opportunity to work on this project and for all the experiences I made during the time at the IGM Cologne.
- Prof. Dr. Andreas Hördt for being the second supervisor.
- Dr. Pritam Yogeshwar for providing advice and support regarding this thesis, his assistance throughout the entire project and the teamwork during many exciting surveys.
- Raphael Rochlitz for the collaboration, the support and all the advices regarding custEM and FEniCS.
- Tilman Hanstein and Sascha Janser for their assistance in the implementation of the Fast Hankel Transform.
- Dr. Atalay Ayele and Dr. Shimeles Fisseha from the IGSSA, Addis Ababa, for the cooperation between our institutes and the support during the field work in Ethiopia.
- Diego, David and all our drivers and local helpers for their assistance during the field work in Ethiopia and especially Diego for the fantastic time we had sharing an office and all the fun during many journeys.
- all members of the "AGEOs" and "Eties" working groups and our fantastic secretary Christiane Kuhl.
- the German Research Foundation (DFG) who has funded this project in the framework of the Collaborative Research Center SFB 806.
- and of course Laura for all her encouraging love and for taking so selflessly care of our little Tsarevich – especially during the last weeks of writing this thesis.

Erklärung

Ich versichere, dass ich die von mir vorgelegte Dissertation selbständig angefertigt, die benutzten Quellen und Hilfsmittel vollständig angegeben und die Stellen der Arbeit – einschließlich Tabellen, Karten und Abbildungen –, die anderen Werken im Wortlaut oder dem Sinn nach entnommen sind, in jedem Einzelfall als Entlehnung kenntlich gemacht habe; dass diese Dissertation noch keiner anderen Fakultät oder Universität zur Prüfung vorgelegen hat; dass sie – abgesehen von unten angegebenen Teilpublikationen – noch nicht veröffentlicht worden ist sowie, dass ich eine solche Veröffentlichung vor Abschluss des Promotionsverfahrens nicht vornehmen werde. Die Bestimmungen der Promotionsordnung sind mir bekannt. Die von mir vorgelegte Dissertation ist von Prof. Dr. Bülent Tezkan betreut worden.

Köln, 08. Januar 2020